Non-Hydrolytic Synthesis of Visible Light Active Stable Metal Oxides and Metal Oxide Coatings for Fuel Forming Reactions

by

Kori D. McDonald

A dissertation submitted in partial fulfillment
of the requirements for the degree of
Doctor of Philosophy
(Chemistry)
in the University of Michigan
2021

Doctoral Committee:

Professor Bart M. Bartlett, Chair
Professor Stephen Maldonado
Professor Max Shtein
Professor Corey R. J. Stephenson

Kori D. McDonald

korimc@umich.edu

ORCID iD: 0000-0002-3420-3653

Dedication

To the giants who helped me see further.

Acknowledgements

Mom and Dad, it goes without saying but I would not be who I am today without you two. I am eternally grateful to have such loving and caring parents who are constantly supportive of everything I do and always encourage me to challenge myself. Susie, I thank you for accepting me into your life and family with unchanging love. Most importantly, I thank you all for giving me such amazing siblings. Carlo, Kendra, Nichole, and Dominic, thank you for just being there and helping me as I grow. You all have continued to be my place of comfort and peace in times of need and I love you.

Vani, you were the best roommate anyone could have hoped for in grad school. I will miss our late night chats well past your bedtime and TV sessions where I explain to you all of the crazy shows I watch. Donald, Uchenna, and Yves thank you for being a home away from home and keeping the Meyerhoff family alive in Michigan. Josi, how could I forget my roots? Thank you for taking me in my first week here. You didn't know me that well yet, but you showed me a kindness I have continued to see grow with our friendship.

Bart, thank you for accepting me into your group even though I had no experience in any of your research areas. I have learned a lot from you in presenting and communicating my science and because of this have developed more confidence in myself and my place in this community. Above all I am thankful for the engaging, collaborative, and fun environment that you foster in the lab. As well, I would like to thank the rest of my committee members – Professors Corey Stephenson, Stephen Maldonado, and Max Shtein. Thank you for your help and advice at each milestone in my degree progress.

To the lab, you all were and are an amazing group of people to work with and learn from. Charles I only got to interact with you for a short time in my rotation, but you have maintained a wonderful and lasting impression in my career. Jimmy thank you for continuing to invite me to your board game nights and being a wonderful presence to be around. John, Sam, Adam, Aaron, and Andy thank you for being great scientists I could look up to. When I was struggling on my project or just needed someone to talk to you all were always there with great advice and suggestions. Aaron especially thank you for being a great friend and making the time spent on our side of the lab very memorable. To Brad, Christian, and Li thank you for showing me how to keep my spark in science alive. I am in awe of who you are as scientists and am excited to see where life takes you. Lastly, thank you to Geoffrey, Matt, and Izzy for working with me in my research and sticking with me through many failing projects. It was a pleasure to both teach and learn from you all.

Table of Contents

List of Figures

List of Tables

List of Illustrations

List of Appendices

Abstract

This thesis addresses current challenges in the synthesis and photochemistry of metal oxide and metal chalcogenide materials, while providing potentially useful avenues for expanding their application. While water splitting is a means to achieve solar fuel production in the formation of hydrogen gas (H_2), the slow kinetics of water oxidation limit large scale utility. As a replacement, the transformation of organic substrates into value-added chemicals has emerged as a scalable alternative. Materials commonly employed for this strategy are metal oxide and metal chalcogenide semiconductors that through excitation from solar light can generate charge carriers capable of facilitating redox chemistry. However, they are limited by energy barriers due to their large band gap, poor charge carrier mobility and photocorrosion during the catalytic transformation. While conventional synthesis eventually leads to pure materials, the attractive aspect of tuning the particle's size and composition comes with great difficulty. This work has focused on investigating synthetic routes for preparing phase pure, metal oxide semiconductor nanomaterials using solvent-assisted low temperature methods through controlled microwave heating.

With the aid of direct heating through microwave irradiation in non-aqueous media, nanocrystalline tungsten (VI) oxide is achievable in 30 minutes at 200°C, faster and at lower temperatures than conventional methods. Forming in a platelet morphology, these particles are 20 nm with a surface area of 37 m^2g^{-1} WO_3. These nanoplatelets are active for the photocatalytic oxidation of the benzylamine (rate constant, k of 0.021 h^{-1} WO_3), benzyl alcohol (k of $2.6x10^{-3}$ h^{-1}), and 5-(hydroxymethyl)-2- furfural (k of 0.01 h^{-1}) using 10 mg of WO_3 with 2 mL of 0.250 M

substrate in acetonitrile and a 150 mW•cm^{-2} 460 nm blue LED source. These rate constants are larger than those observed for commercially prepared, micron-sized WO_3. XPS analysis shows that during catalysis, the concentration of W^{5+} on the surface increases, but the nanoplatelets are stable under these reaction conditions. The morphology and size of the particles are retained through the reactions. Moreover, the nanoplatelets are recyclable—showing no loss in activity for four reaction cycles.

Expanding the synthetic scope, through microwave heating in ethanol and with subsequent annealing, crystalline $MgFe_2O_4$ nanoparticles are produced rapidly and in high yields >99%. Under varied annealing temperatures, the degree of Mg and Fe site inversion changes the optical, electronic, and composition of the nanoparticles. A small particle size of ∼10 nm is achievable with the aid of an ammonium salt mineralizer that caps the particles during nucleation and growth. Particles with the lowest inversion parameter and limited sintering upon annealing (at 600 °C) exhibit the greatest production of hydroxyl radicals under visible light illumination. As such, these particles also facilitate the degradation of methylene blue dye (rate constant k of 0.061 h^{-1}) faster than those particles annealed at higher temperature with 20 mg of catalyst. This synthetic protocol is successively expanded to other ternary metal ferrites with similar crystalline structures.

Finally, from the knowledge gained in this work, the synthesis and photostability of metal chalcogenide materials can be explored for routes to support large scale use. Known approaches to surface modification of nanoparticles are adapted to design complex core@shell structures of well-studied photocatalytic semiconductors. Insights into how the synthetic design can be improved are provided based on the observations of incomplete shell coverage of cadmium selenide (CdSe).

Chapter 1

Introduction

1.1 Addressing the Future Energy Demands with Renewable Energy

Millions of years ago, fossil fuels in the form of coal, oil, and natural gas were formed through natural geological and biological phenomena on earth.[1] In the eleventh century in China, fossil fuel use through coal saw its first spark for implementation into human history. However, it was not until the eighteenth century with the industrial revolution that fossil fuels cemented its place in the energy consumption landscape.[2] Since then, the consumption of fossil fuels has been on an historic rise, rapidly fulfilling the demand for its use (**Figure 1.1**). When burned, their stored energy supplies the continued daily human necessities of providing power to machinery, transportation, and food production to name a few. Nearing the twentieth and twenty-first centuries

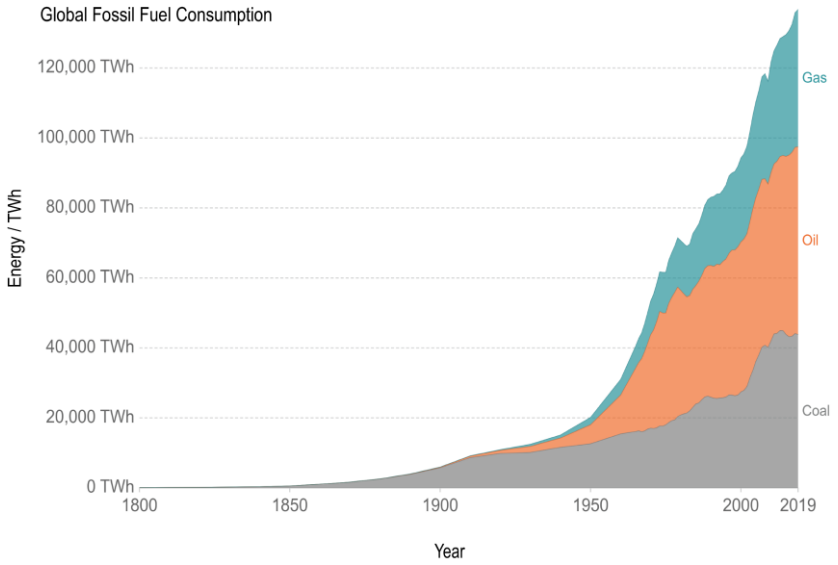

Figure 1.1: Global energy consumption breakdown in terawatt-hours (TWh) of fossil fuels from 1800 to 2019. Each of the three main fuel types (coal, oil, and natural gas) are accounted for.

an information technology boom was predicted to aid in decreasing the consumption of fossil fuels. However, with the rapid large-scale use of these technologies came a new problem to tackle in the increased electricity demand. Thus, fossil fuels will continue to play a pivotal role in the function of our society.

Given the unrelenting use of fossil fuels to support everyday life, one can imagine the build-up of overwhelming consequences that have been ignored. In this dilemma, two main factors are at the forefront for efforts to reshape the energy production and consumption system: (1) the depletion of the fossil fuel reserves and (2) the threat of a global climate crisis. The world's fossil fuel use relies on a nonrenewable source that went untouched for millennia before humans began to exploit it.[3] As the rate of fuel consumption continues to outpace the rate of production the lifetime of this resource is an unknown value. Without a suitable replacement plan in place to restructure our reliance, the state of our infrastructure will suffer. The second issue to address is climate change. Through many necessary global functions, such as the burning of fossil fuels, the release of greenhouse gases (CO_2, CH_4, N_2O, etc.) negatively impacts our environment. When released, these toxic gas emissions fill the Earth's atmosphere and trap the surrounding heat. In a recent survey, it was found that carbon dioxide (CO_2) accounted for 80% of the greenhouse gas emissions in the United States alone.[4] The burning of fossil fuels accounts for the majority of these CO_2 gas emissions, which in turn has led to an increase the average temperature of the Earth by a little over 1°C since 1880.[5] To address this dilemma, there needs to be a shift towards alternative routes for energy production and storage that do not rely on this fleeting, nonrenewable, toxic source.

Capturing renewable sources of energy has long been a facet of energy production, with less of a widespread usage. Various sources encompass the class of renewables including biomass,

geothermal, hydropower, solar, and wind. At its current state, the total energy consumption across all regimes is 19 TW of energy globally.[6] Of this energy, only 1.1% came from solar energy. This aspect is important to note given that of the breadth of renewables sources, the sun affords nearly 5,000 times more energy a year. Across this class, solar energy remains as the most abundant and universally accessible source. While the implementation of solar energy technologies has diversified, the sector has yet to reach it full potential due to some limiting factors. Straining costs of large infrastructures and the need for sustainable storage systems are hindering the growth of this field.

1.2 The Storage of Solar Energy in Chemical Bonds

Harnessing solar energy is accomplished through the use of photovoltaic systems that convert the photons from the sun into electricity.[7,8] The generation of this energy then requires immediate use or storage, otherwise it is wasted. As such, this work seeks to explore other means of solar energy conversion and storage. With that, the potential energy held in chemical bonds presents as a viable option. Energetic bonds of interest are held in chemical energy storage materials, or pure and mixed gas fuels.[9] These include hydrogen (H_2), methane (CH_4), and ammonia (NH_3). Within this group, H_2 presents as the most important alternative to fossil fuel consumption. In any case, the generation of these energy storage materials requires a few pieces of consideration for their production and implementation. For the systems studied in this thesis, storage and transportation of the materials, environmental impact, and compatibility with the current infrastructure come to mind.

While water splitting is a nontoxic means to achieve solar fuel production with the formation of H_2, the kinetic limitations from the required water oxidation component and poor chemical value in O_2 limit large scale utility. In addition, the generation of two gaseous species raises cause

for concern regarding the transportation and isolation of the valuable H_2 product. As a replacement, the selective transformation of organic substrates into value-added chemicals has emerged as a scalable alternative with fewer thermodynamic and kinetic limitations.[10,11] The pressing four electron requirement for the oxidation of water pales in comparison to the two electrons one would need for the oxidation of simple organic functionalities such as alcohols and aldehydes.

Bio-derived substrates from biomass already hold a place in the renewable energy conversation and as such have room for development in other expanding areas. In comparison to OER from water splitting as described above, the transformation of biomass affords a multitude of routes towards value-added chemicals (biochemicals, biomaterials, and biofuels)[12]. In the collection of biomass derived feedstocks, lignocellulosic materials are the most abundant renewable material poised to replace fossil fuels in fuel production. Obtained from plant materials, this agricultural waste product places no hinderance on food or valuable crops and needs no additional resources for cultivation and protecting. The compositional make-up of lignocellulose in a plant has three main components: cellulose (40-70%), hemicellulose (10-40%), and lignin (10-30%)[13]. Cellulose, being the most abundant component, is well utilized for the development of functional platform chemicals through successive oxidative and reductive reactions (**Scheme 1.1**). Refining cellulose, however, comes with its own host of challenges that require further investigation and reforming.

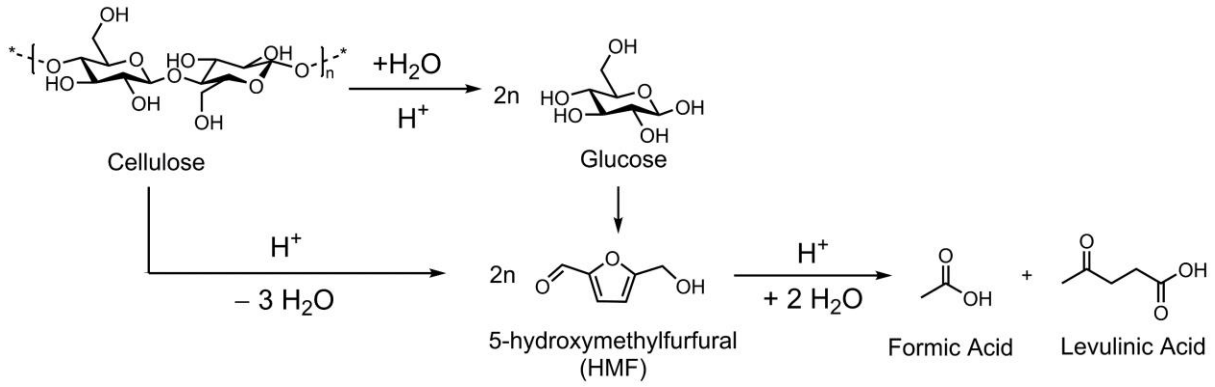

Scheme 1.1 : Example of cellulose refining process to form value added products and commodity chemicals in the form of 5-hydroxymethylfurfural (HMF), formic acid, and levulinic acid.

Namely, the high degree of functionality in the structure raises issues with solubilizing the material for solution processing and requiring corrosive, acid catalyzed depolymerization steps that often hinder product selectivity.

1.3 Semiconductor Photocatalysis and Design Considerations

Photochemically active, heterogeneous catalysts present themselves as strong candidates for advancing this field of H_2 fuel production by way of targeted biomass upgrading. Materials common in studying this are metal oxide (M_xO_y) and metal chalcogenide (M_xE_y, E = S, Se, Te) semiconductors.[14] Figure 1.2a illustrates the process by which these materials become activated by photo-initiation. Through excitation from solar light these materials are activated from absorbed photons that supply enough energy to promote an electron (e^-) from the occupied valence band (VB) ground state to the unoccupied conduction band (CB) excited state. The promotion of this electron creates an excess of negative charge in the conduction band and leaves behind a hole (h^+) in the valence band. With this set of charge carriers targeted redox chemistry can be performed on the surface of suspended semiconducting materials. The minimum energy requirement that a semiconductor must absorb for this process to occur is dictated by the potential difference between the edges of each respective band and is known as the band gap, E_g.

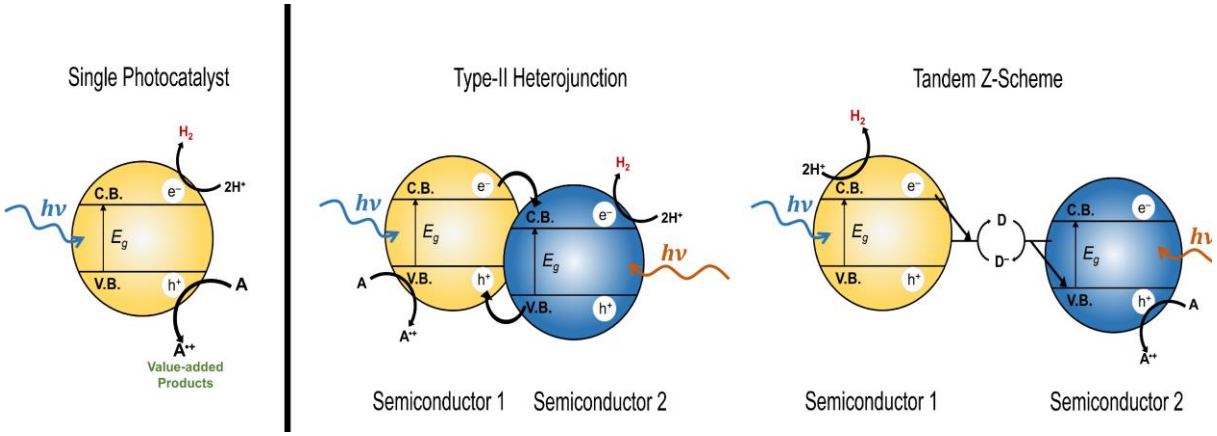

Figure 1.2: (a) Diagram detailing the photocatalytic process for semiconductor particles and **(b)** types of composite configurations. The heterojunction contacts either between two semiconductors or interfaced with the solution aid in charge separation.

To properly design a photochemical reaction system and employ the most applicable catalyst to drive the reactions there are a few key features that the system must exhibit. *(1) The catalyst in question must have strong absorption in the visible light region; that is to say that the band gap must be equivalent to the energy of light in this region.* With the aim to couple organic oxidation reactions with HER, one would need to minimize the use of UV light for catalyst activation as many organic substrates are prone to direct degradation by high energy UV light. *(2) A minimization of particle size to combat changes to charge carrier mobility and lifetimes.* When conducting the described redox chemistry photochemically, rates of chemical reaction are dependent on the ability for the produced charge carriers to migrate from the bulk of the material to the surface where the substrates are adsorbed. By minimizing the overall size of the particles to the nanoscale, one can decrease that distance that charges must diffuse to engage in photocatalysis. As an aside, there remains limitations intrinsically in some semiconducting materials that nano-scaling cannot fully avoid. While charge transport distances are reduced, this does not necessarily ensure that the charges will migrate to the surface and remain separated long enough for the chemistry to proceed. Recombination of the charges at the surface in addition to the bulk remains a pressing challenge for purely photochemically driven reactions. To overcome this challenge, one can design catalyst composites with at least one photo-active material to generate the necessary charge carriers and another to drive the separation of charges away from the photocatalyst. Figure 1.2b highlights the two main configurations for achieving this improved charge separation. Common composite materials researched for metal oxides and chalcogenides are other solid semiconductor materials[15-17], polymeric-carbon based materials [18-20], or metals [21-23]. In any case the latter two catalyst design features are universally required regardless of catalyst type. *(3) Thermodynamic feasibility and selective kinetics for both the organic oxidation reaction and HER.*

In concert with having an appropriate band gap to absorb visible light, the band edges need to be at appropriate potentials to drive the oxidation and reduction reactions in question. For the oxidation reaction to occur the valence band maximum (VBM) edge must be at a positive enough potential with respect to the reduction potential of the organic substrate. Similarly, the conduction band minimum (CBM) edge must be at a negative enough potential to reduce the protons liberated in solution. Figure 1.3 details the band diagram for the primary materials studied in this thesis with the corresponding reduction potentials for the attractive redox processes.[24] *(4) Chemical stability in a range of reactive environments.* Lastly, when the catalyst is designed for the targeted reactions, it must be ensured that the material is stable for repeated cycles. For these materials to retain their marketable sustainability, they must preserve their bulk composition and activity along with recoverability for further recycling in continuous reactions. Metal chalcogenides, such as CdS or CdSe, are direct band gaps semiconductors that have already been investigated as photocatalysts for biomass upgrading in primary and secondary alcohol oxidations.[25-27] This direct band gap nature that they possess allows for improved light absorption and generation of charge carriers, leading to faster catalytic rates.[28] However, major drawbacks to their utilization arise from their

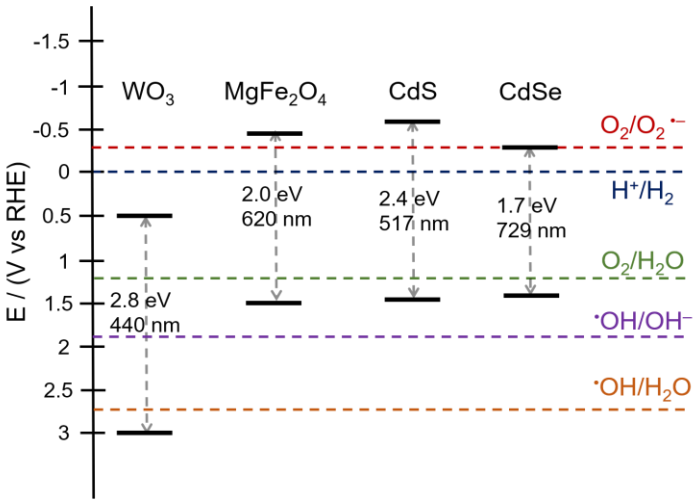

Figure 1.3: Band structures for the semiconductor metal oxide and metal chalcogenide materials discussed in this thesis. Corresponding thermodynamic redox potentials for some targeted processes are shown.

photo-corrosion in aerobic aqueous[29,30] and non-aqueous media[31]. This process results in the loss of the catalyst material and leaching of toxic elements into the reaction solution. When challenges such as these arise for the two previously described characteristics, complex composite materials again present as an alternative route to furthering the chemistry. In properly addressing the needs of the catalytic system, the next steps require confronting the challenge of directed synthesis of the material.

1.4 Metal Oxide and Metal Chalcogenide Synthetic Scope – The Path Towards Microwave Chemistry

The complexity of solid catalytic systems is accompanied by a multitude of routes for their synthesis. This section will cover the general categories of solid materials synthesis, ways in which they are achieved and where they stand in the overall synthetic class.[32]

1.4.1 The Ceramic Method

The most utilized and simple technique in the synthesis of metal oxide particles is the ceramic method. In this route precursor powders are finely ground and mixed as needed or pressed into pellets and heated in a high temperature furnace (300 – 1500°C) for an extended period of hours to days; and sometimes weeks. This prolonged heating time is necessary for this synthetic scope due to the atomic inhomogeneity of the precursor. Critical aspects of this synthesis are diffusion of the precursors through the grain interface to begin the nucleation of crystalline units with the appropriate stoichiometry and structure. This type of solid-state chemistry is often employed for complex, ternary metal oxide materials containing two metals and the corresponding stoichiometric equivalent of oxygen. Taking an example from our own lab, the synthesis of $CuWO_4$ is undertaken by grinding copper (II) oxide (CuO) and tungsten (VI) oxide WO_3 in a crucible at 800°C for 6 hours (**Figure 1.4**).[33] While very robust, this method often results in little

to no control over the tuning of particle size and shape forming low surface area particles with large grain boundaries.

1.4.2 Hydrothermal Synthesis

To impart control on the synthesis, solution-based methods arose as the next course of action. Aqueous sol-gel chemistry through hydrothermal synthesis emerged as a promising route having

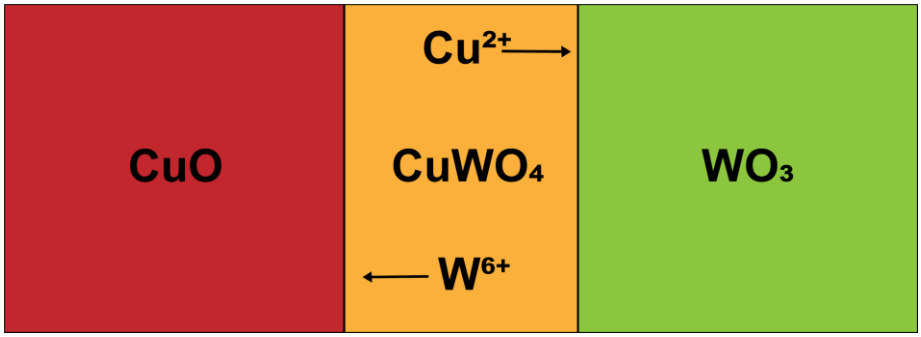

Figure 1.4: Sample phase formation of $CuWO_4$ formed through the ceramic synthesis route.

shown initial success in the preparation of bulk metal oxides with great potential for applications in nanoparticle synthesis. This method involves heating precursors in the form of metal salts in high pressure environments at elevated temperatures (100 – 500°C).[34] However, the attempts to modify this route for the nanoscale proved less fruitful with the reaction systems revealing an unwanted complexity. For starters, in hydrothermal preparations the water acts both as the solvent creating the pressurized medium and as the ligand responsible for transforming the precursors. Rates of hydrolysis and condensation, rates of oxidation, and system pH are just a few reaction parameters one must consider when attempting to utilize the hydrothermal route for the synthesis of metal oxides. In addition, while the synthesis conditions are operating at lower temperatures than the convention solid-state method; there is no guarantee that the as-synthesized powder will be crystalline. More often than not, an amorphous powder is produced, requiring a post-synthesis

treatment of high temperature annealing to force crystallization; a fundamental problem when looking to control size and morphology in nanoparticle synthesis.

1.4.3 Surfactant-Assisted Synthesis

To work around the currently presented drawbacks, the synthetic scheme shifted to be performed under solution assisted conditions in the absence of water. The use of organic solvents bridges in the reaction versatility afforded through both routes and gives more room for control over crystallite size. Particularly, great control in the growth of nanoparticles comes when using surfactants as the organic solvent to transform the precursor compounds. With the synthesis being performed in a typical temperature range of 250 – 350°C, the surfactants act as capping ligands during the growth of these particles.[34,35] This capping serves to facilitate the formation of monodisperse particles that are well dispersed thereafter through controlled growth. As well, the shape of the particles can be fine-tuned with variability in the ligand chain and functional capping group. Though this process offers control over crystal properties like tailored shape and size control; the surface bound surfactants limit the utility of the produced particles. The strong binding nature of the surfactants results in organic surface impurities that restrict accessibility to the surface and present toxicity issues. The steps of nucleation and growth are illustrated in Figure 1.5, showing the remnants of the surface bound ligands after the nanoparticle growth steps. Applications such as gas sensing or even catalysis are only applicable with the removal of the

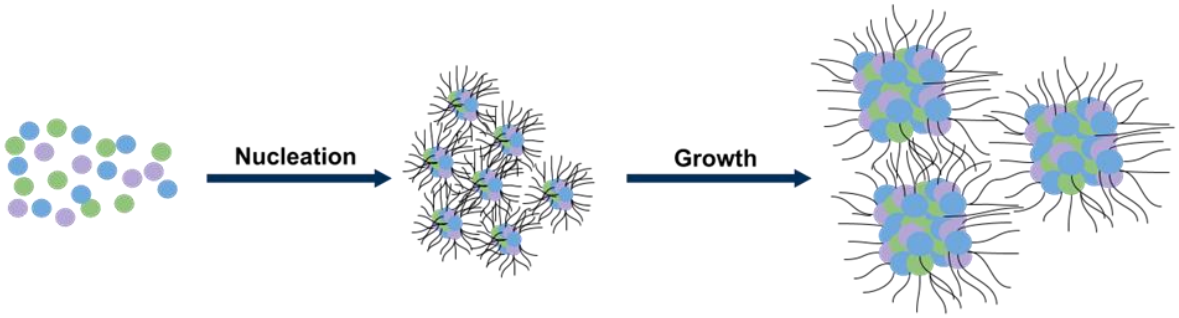

Figure 1.5: Illustration of the nucleation and growth process of nanocrystals following surfactant-assisted protocols. The black tendrils illustrate the capping surfactant ligands that remain on the surface of the particles as they crystallize.

surface species. To remove these ligands and access the surface, heat treatment is thus necessary, often yielding agglomerated particles.

1.4.4 Solvothermal Synthesis

Utilizing organic solvents with lower boiling points than surfactants, systems operated in the range of 50 – 200°C, offer a simpler route to making nanocrystalline solid materials. Here the organic solvents are simpler, non-toxic, and are applicable to more synthetic heating conventions.[34] Without the surface binding surfactants highly crystalline materials can be easily synthesized with unobstructed access to the particles surface. The versatility in this synthetic class arises because of the variety of precursor materials that can be used and potential to understand the underlying mechanism of particle formation. Similar to aqueous synthetic methods, the chosen organic substrate used in these solvent-controlled reactions act both as the solvent for the precursors and their reagent. Thus, observing transformations that occur to the organic solution can reveal the general pathway that the precursors undergo in forming the metal-oxygen and metal-chalcogen bonds. The pathways present as halide elimination (Equation 1.4.1), ether elimination (Equation 1.4.2), ester elimination (Equation 1.4.3), or aldol condensation (Equation 1.4.4).

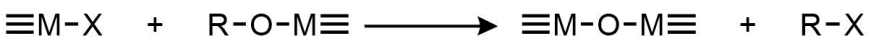

(1.4.1)

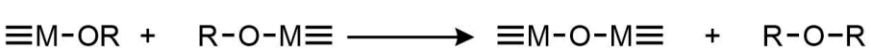

(1.4.2)

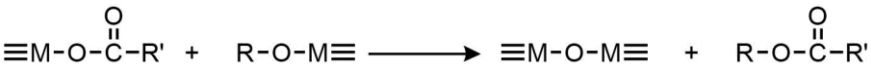

(1.4.3)

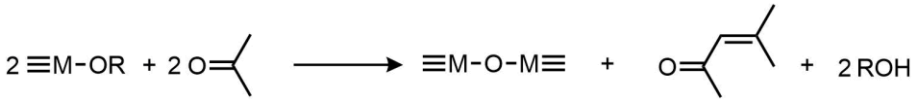

(1.4.4)

Drawbacks are still present for this route compared the surfactant assisted protocols in less control over crystallite size and shape as well as aggregate formation from an unprotected surface. Despite

the drawbacks, the solvothermal route pushes forward as the leading synthetic direction for the robust growth of semiconductor nanoparticles.

1.4.5 Microwave Synthesis

The solvent-assisted approach to nanoparticle synthesis dominates the field due to its adaptability but is still limiting in its efficiency. Under the general solvothermal conditions as they have been studied, the crystallization process involves reaction times on the order of hours to days. Long reaction times prohibit scaled-up production thanks to the heat diffusion dependence in the hydro/solvothermal reaction vessels and poor control over the heating environment altogether. One can begin to speculate that this is why the particle compositions under conventional solvothermal heating yields polydisperse particle grain sizes. Historically applied in the realm of organic synthesis, microwave heating is increasingly finding its place in the synthesis of solid inorganic materials. In Figure 1.6, the heating isotherms presented for both conventional and microwave heating approaches highlights the rapid heating afforded through microwave irradiation and how it can drastically reduce reaction times. Operating through the alignment and activation of dipoles in organic solvents, microwave reactors can efficiently generate and disperse heat in any given solution. The success of a solvents utility under microwave heating can be measured through correlation of its dielectric loss (ε'') and permittivity (ε') in the parameter tan δ, shown in equation

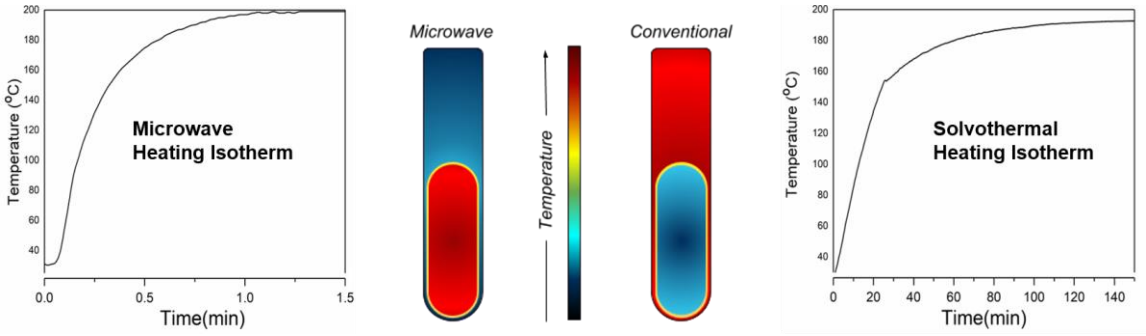

Figure 1.6: Comparative heating isotherms between microwave heating and conventional solvothermal heating. The middle picture illustrated the distribution of heat within the two systems.

1.4.5.[34,36] Solvents with a high microwave absorbing properties (tan δ > 0.5) such as alcohols (ethylene glycol, ethanol) or dimethyl sulfoxide (DMSO) will offer a rapid and controlled heating environment in a reactor. Solvents with a medium (0.1 < tan δ < 0.5) to low (tan δ < 0.1) tan δ lack a permanent dipole moment preventing sufficient microwave absorption, though can still be utilized with the aid of polar molecule additives such as ionic liquids.

$$tan\ \delta = \ \varepsilon" \ / \ \varepsilon' \qquad (1.4.5)$$

In addition to the rapid heating, common reactors allow for magnetic stirring during the synthetic process to even further aid in the dispersion of heat and increase the chance of forming a monodisperse collection of nanoparticles. Large scale syntheses are made possible thanks to the fast and uniform heating from microwave irradiation making it the obvious choice for exploring the synthesis and application of semiconductor photocatalysts.

1.5 Scope of This Thesis

This thesis work seeks to serve as a foundation for the design of new synthetic routes for phase pure, metal oxide semiconductor nanomaterials using solvent-assisted low temperature methods through controlled microwave heating. Upon synthesizing the appropriate materials, further objectives entail understanding the photochemical activity of these metal oxides for photochemically driving redox reactions.

Chapter 2 details the initial exploration of solvothermal, microwave chemistry for the synthesis of metal oxide photocatalysts. Starting with a well explored material both in our lab and in others, tungsten (VI) oxide (WO_3) will serve as our guide for the validity of this route. Starting from simple salt precursors and in simple organic solvents, the synthesis of WO_3 is shown. Extensive characterization analysis is provided and discussed to reveal phase and properties pertinent to catalysis. Evaluation of photochemical reactivity in the space of biomass derived organic

oxidations is supplemented to support justification of synthetic route. The work in this chapter lays the foundation for understanding key synthetic adjustments that must be made for the development of photocatalysts.

Expanding upon this work Chapter 3 highlights investigations into interesting classes of metal oxide semiconductors in ternary metal ferrites with spinel structure (MFe_2O_4). Adapting similar microwave principles, the amorphous form of magnesium ferrite ($MgFe_2O_4$) is shown. An interesting facet to the chemistry associated with this class of materials lies in the ability to alter the physical and electronic properties, thus affecting its photocatalytic capabilities. To study these structure-properties relationships, high temperature annealing was applied to the as-made nanoparticles. Catalysis and kinetic analysis serve to determine the controlling factors over the rates of photocatalytic redox reactions.

Understanding the ways in which synthetic modification through solvent-assisted and microwave routes can be altered, Chapter 4 briefly explores how these principles can facilitate stability improvements in metal chalcogenide photocatalysts. To prevent photo-corrosion of highly reactive cadmium sulfide (CdS) and cadmium selenide (CdSe) nanoparticles, protective oxide layers are studied for their ability to stabilize the surface during catalysis. Finally, Chapter 5 of this thesis summarizes the main conclusions revealed through the previous chapters and takes a brief look at the next directions that will further the development of the field.

1.6 References

1. Pirani, Si. *Burning Up A Global History of Fossil Fuel Consumption*; Pluto Press, 2018.

2. Morris, I. *Foragers, Farmers, and Fossil Fuels: How Human Values Evolve*; Princeton University Press, 2015.

3. How long before we run out of fossil fuels? https://ourworldindata.org/how-long-before-we-run-out-of-fossil-fuels (accessed June 1, 2021).

4. Inventory of U.S. Greenhouse Gas Emissions and Sinks https://www.epa.gov/ghgemissions/inventory-us-greenhouse-gas-emissions-and-sinks (accessed June 1, 2021).

5. Al-Ghussain, L. Global Warming: Review on Driving Forces and Mitigation. *Environ. Prog. Sustain. Energy* **2019**, *38* (1), 13–21.

6. Renewable energy consumption, World https://ourworldindata.org/grapher/renewable-energy-consumption?country=~OWID_WRL (accessed June 1, 2021).

7. Mahmoud, M.; Ramadan, M.; Olabi, A.-G.; Pullen, K.; Naher, S. A Review of Mechanical Energy Storage Systems Combined with Wind and Solar Applications. *Energy Convers. Manag.* **2020**, *210*, 112670.

8. Koçak, B.; Fernandez, A. I.; Paksoy, H. Review on Sensible Thermal Energy Storage for Industrial Solar Applications and Sustainability Aspects. *Sol. Energy* **2020**, *209*, 135–169.

9. Allison, T.; Smith, N. R.; Ma, Z. Introduction to Energy Storage. In *Thermal, Mechanical, and Hybrid Chemical Energy Storage Systems*; Elsevier, 2021; pp 1–25.

10. Nicewicz, D. A.; MacMillan, D. W. C. Merging Photoredox Catalysis with Organocatalysis: The Direct Asymmetric Alkylation of Aldehydes. *Science* **2008**, *322* (5898), 77–80.

11. Fagnoni, M.; Dondi, D.; Ravelli, D.; Albini, A. Photocatalysis for the Formation of the C−C Bond. *Chem. Rev.* **2007**, *107* (6), 2725–2756.

12. Gilkey, M. J.; Xu, B. Heterogeneous Catalytic Transfer Hydrogenation as an Effective Pathway in Biomass Upgrading. *ACS Catal.* **2016**, *6* (3), 1420–1436.

13. Luque, R.; Balu, A. M. *Producing Fuels and Fine Chemicals from Biomass Using Nanomaterials*; 2014.

14. Colmenares, J. C.; Luque, R. Heterogeneous Photocatalytic Nanomaterials: Prospects and Challenges in Selective Transformations of Biomass-Derived Compounds. *Chem. Soc. Rev.* **2014**, *43* (3), 765–778.

15. Low, J.; Yu, J.; Jaroniec, M.; Wageh, S.; Al-Ghamdi, A. A. Heterojunction Photocatalysts. *Adv. Mater.* **2017**, *29* (20), 1601694.

16. Wang, F.; Gu, Y.; Yang, Z.; Xie, Y.; Zhang, J.; Shang, X.; Zhao, H.; Zhang, Z.; Wang, X. The Effect of Halogen on BiOX (X = Cl, Br, I)/Bi2WO6 Heterojunction for Visible-Light-Driven Photocatalytic Benzyl Alcohol Selective Oxidation. *Appl. Catal. A Gen.* **2018**, *567*, 65–72.

17. Sadik, W. A.; El-Demerdash, A.-G. M.; Nashed, A. W.; Mostafa, A. A.; Hamad, H. A. Highly Efficient Photocatalytic Performance of Cu2O@TiO2 Nanocomposite: Influence of Various Inorganic Oxidants and Inorganic Anions. *J. Mater. Res. Technol.* **2019**, *8* (6), 5405–5414.

18. Fu, Y.; Chen, H.; Sun, X.; Wang, X. Combination of Cobalt Ferrite and Graphene: High-Performance and Recyclable Visible-Light Photocatalysis. *Appl. Catal. B Environ.* **2012**, *111–112*, 280–287.

19. Li, P.; Zhou, Y.; Li, H.; Xu, Q.; Meng, X.; Wang, X.; Xiao, M.; Zou, Z. All-Solid-State Z-Scheme System Arrays of Fe 2 V 4 O 13 /RGO/CdS for Visible Light-Driving Photocatalytic CO 2 Reduction into Renewable Hydrocarbon Fuel. *Chem. Commun.* **2015**, *51* (4), 800–803.

20. Huang, Z.; Zeng, X.; Li, K.; Gao, S.; Wang, Q.; Lu, J. Z-Scheme NiTiO 3 /g-C 3 N 4 Heterojunctions with Enhanced Photoelectrochemical and Photocatalytic Performances under Visible LED Light Irradiation. *ACS Appl. Mater. Interfaces* **2017**, *9* (47), 41120–41125.

21. Zhou, B.; Song, J.; Zhang, Z.; Jiang, Z.; Zhang, P.; Han, B. Highly Selective Photocatalytic Oxidation of Biomass-Derived Chemicals to Carboxyl Compounds over Au/TiO 2. *Green Chem.* **2017**, *19* (4), 1075–1081.

22. Bellardita, M.; García-López, E. I.; Marcì, G.; Palmisano, L. Photocatalytic Formation of H2 and Value-Added Chemicals in Aqueous Glucose (Pt)-TiO2 Suspension. *Int. J. Hydrogen Energy* **2016**, *41* (14), 5934–5947.

23. Han, G.; Jin, Y.-H.; Burgess, R. A.; Dickenson, N. E.; Cao, X.-M.; Sun, Y. Visible-Light-Driven Valorization of Biomass Intermediates Integrated with H 2 Production Catalyzed by Ultrathin Ni/CdS Nanosheets. *J. Am. Chem. Soc.* **2017**, *139* (44), 15584–15587.

24. Armstrong, D. A.; Huie, R. E.; Koppenol, W. H.; Lymar, S. V.; Merényi, G.; Neta, P.; Ruscic, B.; Stanbury, D. M.; Steenken, S.; Wardman, P. Standard Electrode Potentials Involving Radicals in Aqueous Solution: Inorganic Radicals (IUPAC Technical Report). *Pure Appl. Chem.* **2015**, *87* (11–12), 1139–1150.

25. Li, C.; Wang, H.; Ming, J.; Liu, M.; Fang, P. Hydrogen Generation by Photocatalytic Reforming of Glucose with Heterostructured CdS/MoS2 Composites under Visible Light Irradiation. *Int. J. Hydrogen Energy* **2017**, *42* (27), 16968–16978.

26. Wakerley, D. W.; Kuehnel, M. F.; Orchard, K. L.; Ly, K. H.; Rosser, T. E.; Reisner, E. Solar-Driven Reforming of Lignocellulose to H2 with a CdS/CdOx Photocatalyst. *Nat. Energy* **2017**, *2* (4), 17021.

27. DiMeglio, J. L.; Breuhaus-Alvarez, A. G.; Li, S.; Bartlett, B. M. Nitrate-Mediated Alcohol Oxidation on Cadmium Sulfide Photocatalysts. *ACS Catal.* **2019**, *9* (6), 5732–5741.

28. Hernández-Ramírez, A.; Medina-Ramírez, I. *Photocatalytic Semiconductors*; Springer International Publishing, 2015.

29. Meissner, D.; Memming, R.; Kastening, B.; Bahnemann, D. Fundamental Problems of Water Splitting at Cadmium Sulfide. *Chem. Phys. Lett.* **1986**, *127* (5), 419–423.

30. Xi, L.; Lek, J. Y.; Liang, Y. N.; Boothroyd, C.; Zhou, W.; Yan, Q.; Hu, X.; Chiang, F. B. Y.; Lam, Y. M. Stability Studies of CdSe Nanocrystals in an Aqueous Environment. *Nanotechnology* **2011**, *22* (27), 275706.

31. DiMeglio, J. L.; Bartlett, B. M. Interplay of Corrosion and Photocatalysis During Nonaqueous Benzylamine Oxidation on Cadmium Sulfide. *Chem. Mater.* **2017**, *29* (17), 7579–7586.

32. West, A. *Solid State Chemistry and Its Applications*; Wiley-VCH, 2014.

33. Proctor, A. D.; Panuganti, S.; Bartlett, B. M. CuWO 4 as a Photocatalyst for Room Temperature Aerobic Benzylamine Oxidation. *Chem. Commun.* **2018**, *54* (9), 1101–1104.

34. Niederberger, M.; Pinna, N. *Metal Oxide Nanoparticles in Organic Solvents*; Engineering Materials and Processes; Springer London: London, 2009.

35. van Embden, J.; Chesman, A. S. R.; Jasieniak, J. J. The Heat-Up Synthesis of Colloidal Nanocrystals. *Chem. Mater.* **2015**, *27* (7), 2246–2285.

36. Bilecka, I.; Niederberger, M. Microwave Chemistry for Inorganic Nanomaterials Synthesis. *Nanoscale* **2010**, *2* (8), 1358.

Chapter 2

Photocatalytic Primary Amine and Alcohol Oxidation on WO_3 Nanoplatelets

Portions of this chapter were published:
McDonald, K. D.; Bartlett, B. M. *RSC Adv.* **2019**, *9* (49), 28688.

2.1 Introduction

Transforming organic substrates into value-added chemicals has long been researched through forming carbon–carbon and carbon–nitrogen bonds. Using sources of visible light, these reactions have improved with the help of many homogeneous transition metal photocatalysts.[1–3] While these routes prove feasible for achieving high reactivity, limitations arise as many known catalysts contain toxic and expensive metals such as ruthenium or iridium. In addition, their homogeneity, and thus complex removal, hinders any larger scale utility. As such, heterogeneous metal oxide catalysts present themselves as an alternative route to achieving the same reactivity.[4,5] Many offer long-term photostability and easy filtering to prevent the leaching and loss of expensive metals.

Many metal oxides are highly reactive towards photocatalyzed transformations of organic substrates. Among them, tungsten oxides have emerged as a prominent photocatalyst capable of performing various energy and environmentally relevant transformations. Many have explored the usefulness of tungsten (VI) oxide (WO_3), a well -studied visible light absorbing semiconductor with a band gap of 2.7–2.8 eV, for its ability to photochemically[6,7] and photoelectrochemically[8–10] oxidize water and degrade organic

dyes. Using the knowledge gained from these known reactions as a guide, the controlled oxidation of organic molecules are being explored to replace these challenging processes.

As presented in the introduction chapter, recent work has shown that for the same catalyst composition, using nanoscale particles can lead to improved rates of photocatalytic reactions.[11,12] The rate enhancement can be attributed to the increase in the specific surface area of the material and the decrease in electron–hole transport distance photogenerated charge carriers must diffuse before reaching the particle surface. Attempts have been made to synthesize many binary oxides on the nanoscale, though many routes are time consuming, energy demanding, and require a post-synthesis heat treatment to achieve a crystalline phase, which often results in sintering (and thus increased particle size and potential loss of important morphology).[13–16] To avoid these drawbacks, a known microwave-assisted synthesis of crystalline monoclinic WO_3 nanoparticles prepared in benzyl alcohol solvent was adapted.[17] The direct heating afforded by microwave irradiation results in faster heating rates and a more homogeneous heat distribution in the reaction solution to impart control over the nucleation and growth of the desired material.[18–24]

Moreover, the non-aqueous solvents act as surfactants and control particle size and shape during heating in microwave reactions.[22,25,26] Efforts have already been directed towards forming metal oxides through this combined route, though directly comparing how the synthesis conditions affect organic photocatalysis has seldom been explored.

Herein, the photocatalytic oxidation of benzylamine, benzyl alcohol and 5-(hydroxymethyl)-2-furfural (HMF) is explored and shown to proceed at faster rates on the surface of WO_3 nanoplatelets than on the bulk material. Benzylamine and benzyl alcohol oxidation serve as test reactions for the selective oxidation of organic substrates and

selective oxidation of biomass relevant substrates, respectively. The HMF substrate shows the promise of WO_3 for transforming biomass-derived feedstocks into value-added chemicals.

2.2 Experimental Section

2.2.1 Materials

Tungsten (VI) chloride (99.9%) was purchased from Strem Chemicals. Benzylamine (99%), N-benzylidenebenzylamine (99%), chlorobenzene (99+%, for spectroscopy), and tungsten (VI) oxide (99.9%) were purchased from Sigma-Aldrich. Acetonitrile (Certified ACS), dichloromethane (Certified ACS), ethanol (200 proof), benzyl alcohol (Certified ACS), and 5-(hydroxymethyl)-2-furfural (98%) were purchased from Fisher Scientific. Acetonitrile-d_3 was purchased from Cambridge Isotope Laboratories. Benzyl alcohol was vacuum distilled and stored on sieves under N_2. All other reagents were used as received. Nylon syringe filters (25 mm, 0.2 μm membrane) were purchased from VWR or Macherey-Nagel.

2.2.2 Microwave Synthesis

In a typical synthesis, 0.5 mmol of tungsten hexachloride was added to 10 mL of stirring benzyl alcohol in a glass microwave vial with an inner volume of 30 mL in an N_2-filled glovebox (Vacuum Atmospheres). The dissolved powder formed a red solution that proceeded to turn blue with further stirring. The glass microwave vessel was then sealed with a PTFE-lined cap and taken out of the glovebox. The microwave experiments were conducted using an Anton Paar Monowave 400 synthesis reactor. During microwave heating, stirring was maintained with a magnetic stir bar in the reaction mixture at 800 rpm. The organic reaction was induced by automatic adjustments to the microwave power to rapidly heat the solution to 200 °C (Figure A.1). This temperature is held constant for 30 minutes before being quenched with compressed air and cooled to room

temperature. The temperature and pressure are controlled and maintained by an internal IR thermometer and pressure sensor, respectively. After microwave irradiation, the resulting precipitate is collected by centrifugation and thoroughly washed with ethanol (2×) and chloroform (2×) under ambient conditions. Yield: 0.43 mmol WO_3, 87% based on starting WCl_6. The initial reaction mixture is saved for GC-MS analysis to observe the organic by-products. The powders were dried in a vacuum oven (Fisher Scientific) at 60°C overnight.

2.2.3 Material Characterization

Powder X-ray diffraction (XRD) data were collected on a Panalytical Empyrean diffractometer at a power of 1.8 kW (45 kV, 40 mA) with Cu Kα (λ = 1.5418 nm) radiation. The detector was a X'Celerator Scientific, a position sensitive 1D detector equipped with Bragg-BrentanoHD X-ray optic delivering only Kα radiation. Patterns were collected with a sampling step of 0.020° and a scan rate of 0.080°• s^{-1} while spinning the sample stage at a rate of 0.25 Hz. Transmission electron microscopy (TEM) was performed on a JEOL 3011 high-resolution electron microscope operated at 300 kV. The samples were ground with a mortar and pestle and then suspended in ethanol. One drop of this suspension was deposited on a carbon grid. The ethanol was allowed to evaporate before sample imaging. Gas chromatography coupled to mass spectrometry (GC-MS) was performed on a Shimadzu QP-2010 GCMS quadrupole. Brunauer−Emmett−Teller (BET) surface area measurements of the catalysts were obtained on a Quantachrome NOVA4200e. A Varian Cary 5000 spectrophotometer equipped with an external diffuse reflectance accessory was used for UV-vis measurements. These reflectance data were transformed into absorbance using the Kubelka-Monk function. Barium sulfate was used as a 100% reflectance standard. Photoluminescence (PL) spectra were collected using a Horiba Quanta Master fluorimeter with a Xe-arc lamp as the excitation source. Electron paramagnetic resonance (EPR) spectroscopy was

performed using a Bruker EMX electron spin resonance spectrometer with a Bruker 4102-ST cavity. X-ray photoelectron spectroscopy (XPS) was performed on a Kratos Axis Ultra using a monochromatic Al source. Collected spectra were corrected for charging by referencing the C(1s) peak to 284.8 eV. All peaks were fitted in Casa XPS with the Shirly-type background.

2.2.4 Photocatalytic Activity Tests

Photocatalytic oxidation of primary amines were carried out in front of a Newport-Oriel 150W Xe arc lamp equipped with an AM 1.5G solar simulator filter and water filters to cool the reaction. A fan was also used to keep the reaction at room temperature. Vials placed in front of the lamp received a front cell irradiance of 300 mW•cm^{-2} (3-sun). Reactions were run in 4 mL glass dram vials containing 10 mg of catalyst and 2 mL of 250 mM substrate solution in acetonitrile. Reactions were capped with a rubber septum; and kept under an O_2 atmosphere using balloons. Photocatalytic oxidation of primary alcohols were carried out using narrow linewidth blue LEDs (460 nm) with an irradiance of ~150 mW•cm^{-2} (1.5-sun). Reactions were run in 4 mL glass dram vials containing 10 mg of catalyst and 2 mL of 250 mM substrate solution in acetonitrile. Reactions were capped with a rubber septum; and kept under an O_2 atmosphere using balloons. A fan was used to keep the reaction at room temperature, measured with thermometer in a control acetonitrile solution (Figure A.2). Prior to irradiation, all solutions were stirred for an hour in the dark to establish an adsorption-desorption equilibrium before having an aliquot taken out to determine the initial concentration of substrate in each solution. To confirm the importance of an O_2 atmosphere, control experiments were performed in an N_2-filled glovebox (Vacuum Atmospheres), using the above-described LED set-up with the alcohol substrate. Recyclability experiments were conducted in observation of the photocatalytic oxidation of benzyl alcohol. In each successive cycle. The reaction solution was illuminated for 24 hours. After this period, the solution was separated by

centrifugation and the remaining powder was washed with acetonitrile (3x) to remove any residual benzyl alcohol. The powder was finally allowed to dry in a 60°C vacuum oven before being used further. Reaction progression was monitored by GC with a flame ionization detector on a Trace 1310 GC-FID system with a TG-5MS Amine column. Argon was used as the carrier gas. Data were collected with chlorobenzene as an internal standard and were then converted to first order rate plots. Selectivity data was collected using ^{1}H NMR spectroscopy with dichloromethane as an internal standard in acetonitrile-d_3. Before NMR analysis, each reaction was filtered through a nylon syringe filter to remove the catalyst. ^{1}H NMR data was collected on a Varian MR400 NMR spectrometer equipped with a Varian 5 mm PFG AutoX Dual Broadband probe.

2.3 Results and Discussion

2.3.1 Synthesis, Phase, and Morphology

Similar to a previously reported example,[17] crystalline WO_3 is formed through rapid heating of soluble tungsten hexachloride in benzyl alcohol solvent at 200°C for 30 minutes with stirring under microwave irradiation *with no further annealing*. This material is denoted as MW–30. The

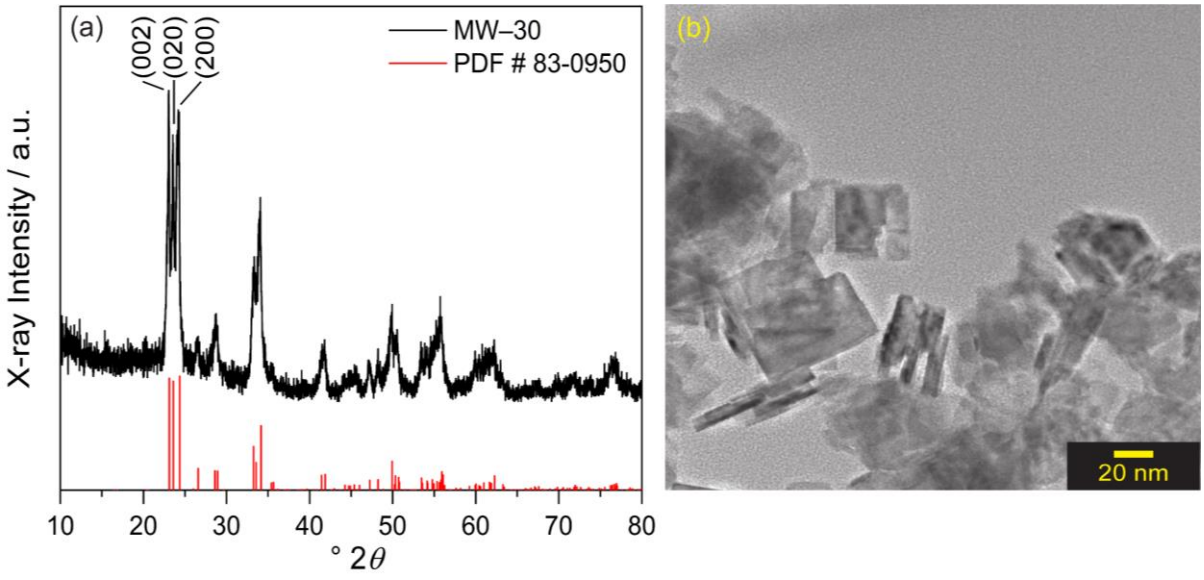

Figure 2.1 : (a) Powder XRD pattern of MW–30 nanoplatelets (black) and reference pattern (red) corresponding to monoclinic WO_3. **(b)** TEM image of MW–30 nanoparticles.

powder X-ray diffraction pattern for the as-synthesized powder is shown in Figure 2.1a. All diffraction peaks can be assigned to the monoclinic phase of WO_3 (PDF #83-0950). The average domain size was calculated to be 20 nm with the Scherrer equation using the (002) reflection. Transmission electron microscopy (TEM) shows that the particle size is consistent with this domain size, with a platelet morphology of the particles, along with a 5 – 10 nm thickness (Figure 2.1b). Slight agglomeration from the lack of stabilizing surfactants is observed, though the individual grains are clear. Nitrogen sorption isotherms reveal a BET surface area of 37 $m^2 \bullet g^{-1}$ for the particles, which is notably larger than that of commercially available nanocrystalline WO_3 (only 2.6 $m^2 \bullet g^{-1}$).

Oxide formation is achieved from benzyl alcohol, which acts as solvent and reactant, analogous to results found in previous solvent assisted syntheses.[17,22,25] GC-MS analysis (Figure A.3) performed on the reaction solution after removal of the suspended particles supports the common mechanisms of halide elimination and either elimination with benzyl chloride, residual benzyl alcohol, and dibenzyl ether observed at retention times 5.72 min, 5.95 min, and 10.43 min respectively. The identity of each by-product was confirmed and referenced by the corresponding mass spectra for each (Figure A.4). The reaction proceeds through the mechanisms illustrated in Scheme 1. Integrating the GC data shows that these two by-products form in a ratio of 12.6:1 dibenzyl ether to benzyl chloride.

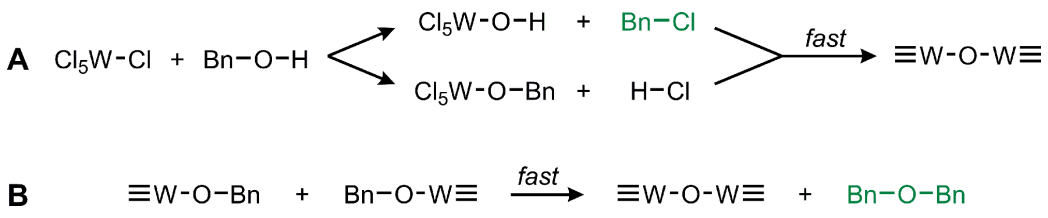

Scheme 2.1 : General proposed routes of WCl_6 and BnOH reacting via **(A)** halide elimination and **(B)** ether elimination. The observed by-products are in green text.

2.3.2 Electronic Structure Before Photocatalysis

In attempting to probe photocatalytic activity on MW–30, it is therefore imperative that charge separation and transfer to the oxidizable substrate are efficient. As such, the charge separation was observed for the presently studied material. With the obtained photoluminescence spectra, the movement of the photogenerated charge carriers is observed. From the presented spectra in Figure 2.2a, a prominent blue emission is displayed at 460 nm, commonly found for WO_3 materials.[27] This feature is attributed to the radiative recombination of conduction band electrons and valence band holes, and the energy of this transition is close to the observed band gap of the oxide, 2.7 eV (Figure A.5). This data also agrees with the spectra collected for the commercially available WO_3, which shows a similar blue emission and recombination (Figure A.6).

Further the MW–30 nanoparticles were characterized to probe the defect structure in the synthesized material. To start, EPR spectroscopy was performed on neat powder, and the spectrum is presented in Figure 2.2b. The observed broad resonances with Landé *g* factors at 4.22 and 2.02

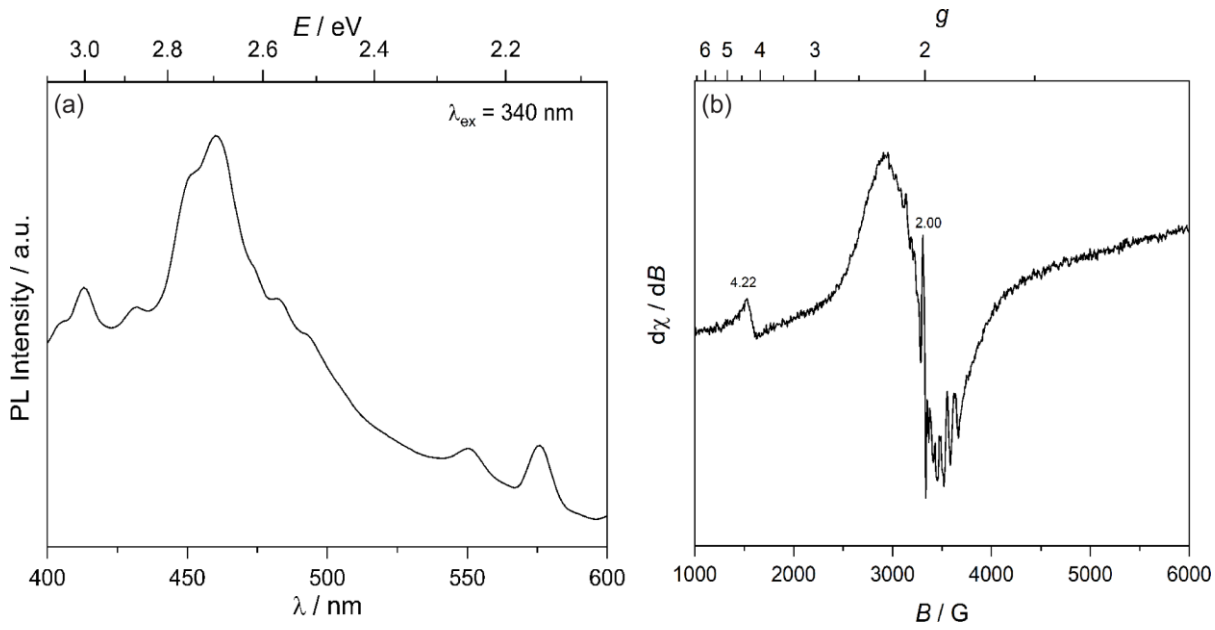

Figure 2.2 : (a) Room temperature photoluminescence spectra for the as-synthesized MW–30 particles. Spectra were collected with an excitation wavelength of 340 nm. **(b)** Room temperature EPR spectra for the as-synthesized MW–30 particles.

can be assigned to the presence of W^{5+} impurities. There is also a very sharp feature centered at g = 2.00, indicative of F^{+} centers in the form of electrons trapped on oxygen vacancies.[28] These defects are those typically found in *n*-type WO_3.

X-ray photoelectron spectroscopy (XPS) was then used to confirm surface reduction of tungsten. From the spectrum in Figure 2.3a of the 4f orbitals on tungsten, the main spin-orbit coupled ^2F lines seen at 35 eV and 37.5 eV can be attributed to W^{6+} in the oxide. However, small shoulders appear at lower binding energy, which corroborates having reduced W^{5+} in the material. Integrating the deconvoluted peaks reveals only a 4.6 mol% W^{5+} content. Such an occurrence is not uncommon, as seen in our previous report, among others, on the reduction of tungsten in the synthesis of WO_3.[29] This minimal W^{5+} content is also observed in the commercially available WO_3 powder with 2.6% W^{5+}, calculated from the deconvoluted W 4f XPS spectra (Figure A.7). In MW–30, further reduction likely arises from the known strong reducing power of alcohols under solvothermal conditions wherein W^{6+} is easily reduced as a small quantity of benzyl alcohol solvent is oxidized to benzaldehyde, as observed by GC-MS. Further mechanistic analysis is also

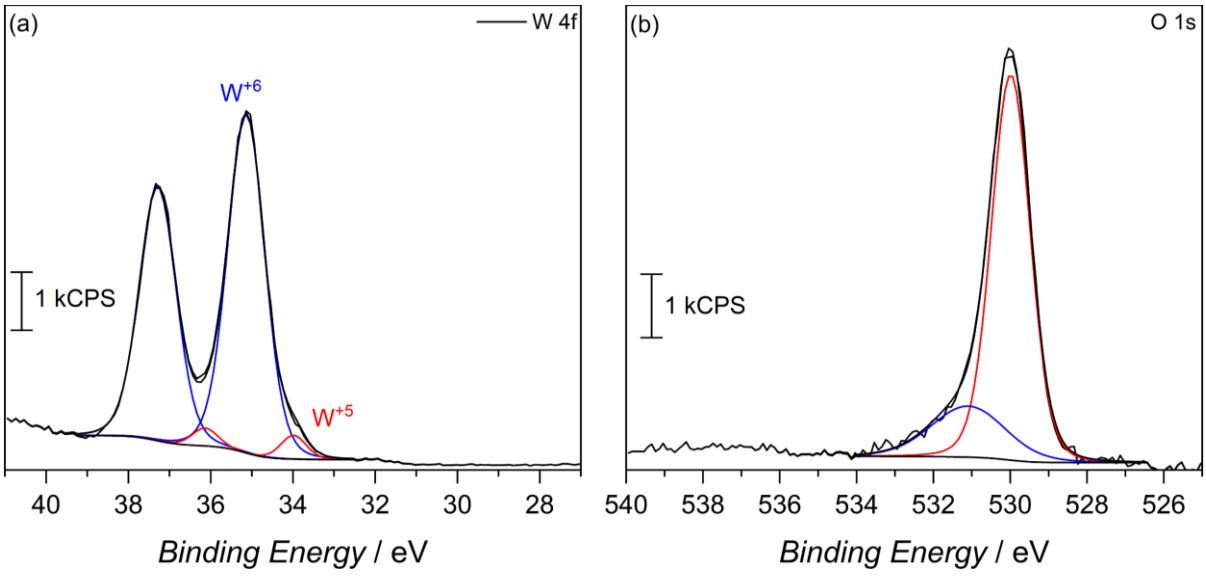

Figure 2.3 : (a) W 4f and **(b)** O 1s XPS spectra for the as-synthesized MW–30 particles.

revealed in the O 1s spectra (Figure 2.3b). Deconvolution of the O 1s spectra to give peaks at 530 eV and 531 eV, respectively, and correspond to W-O-W bonds and W-O-H bonds respectively, indicating hydroxy termination at the surface of the synthesized material.[30]

2.3.3 Microwave Assisted Particle Size Change and Photocatalytic Reaction with 1º Amines

To demonstrate how particle size alters the rate of photocatalytic reactions, larger particles were synthesized by lengthening the hold time of the microwave protocol to 60 minutes. These particles also match the same monoclinic phase for WO_3 (Figure A.8) but have an average grain size of 40 nm, twice as large as the WO_3 obtained from a 30-minute hold time. The TEM images agree with this calculated grain size, and show increased agglomeration, though the platelet morphology is retained. Accordingly, the surface area for these particles is lower, 26 $m^2 \bullet g^{-1}$. In addition, larger WO_3 particles were obtained from a commercial source. The commercially available particles show an average grain size of 100 nm and a surface area that is much lower, only 2.63 $m^2 \bullet g^{-1}$.

To assess the observed size disparities between the obtained particles, kinetics experiments were conducted for benzylamine photo-oxidation to N-benzylidenebenzylamine (N-BB) as a test case. In previous reports, various metal oxides have proven successful (TiO_2[4,31], $BiVO_4$[32,33], and $CuWO_4$[32]) in the photochemical oxidation, wherein the presence of molecular oxygen served as the oxidant. For all cases of WO_3 particles, $BnNH_2$ oxidation is achieved with visible light illumination according to the balanced equation in Scheme 2.2.

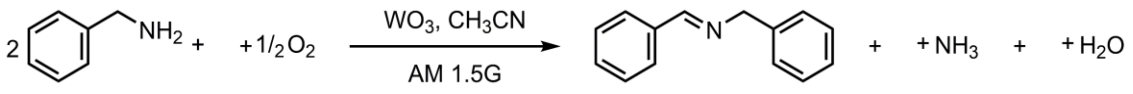

Scheme 2.2 : The balanced chemical equation for the photocatalytic oxidation of benzylamine on WO_3 nanoparticles in air with acetonitrile as the solvent.

The reaction is first order in $BnNH_2$ starting substrate. The data in Figure 2.4 represent the average and standard deviation for the kinetics of photochemical oxidation of $BnNH_2$ on smaller particles synthesized in 30-minutes (MW–30), on larger particles synthesizes in 60 minutes (MW–60), and on bulk commercial WO_3. For MW–30, the reaction rate increases reproducibly between 12 and 18 hours of illumination, and the observed rate constant after this initial induction period is 2.10 $h^{-1}g^{-1}$ WO_3. Neither the larger particles nor bulk WO_3 show this change in reaction kinetics, and the rate constants are smaller, 0.91 $h^{-1}g^{-1}$ MW–60, and 0.71 $h^{-1}g^{-1}$ bulk WO_3. This result suggests that substrate adsorption is a necessary step in the reaction pathway since the rate constant decreases as the surface area of the particles decreases; the surface area of the commercial particles is 2.63 $m^2 \bullet g^{-1}$. In addition to an increase in reaction rate as the particle size decreases, high chemoselectivity is achieved for the N-BB product; MW–30 has a selectivity of >99% and a yield of 90% for N-BB after 96 hours of converting benzylamine. These results agree with previously reported cases of metal oxide catalyzed photochemical $BnNH_2$ oxidation.[32]

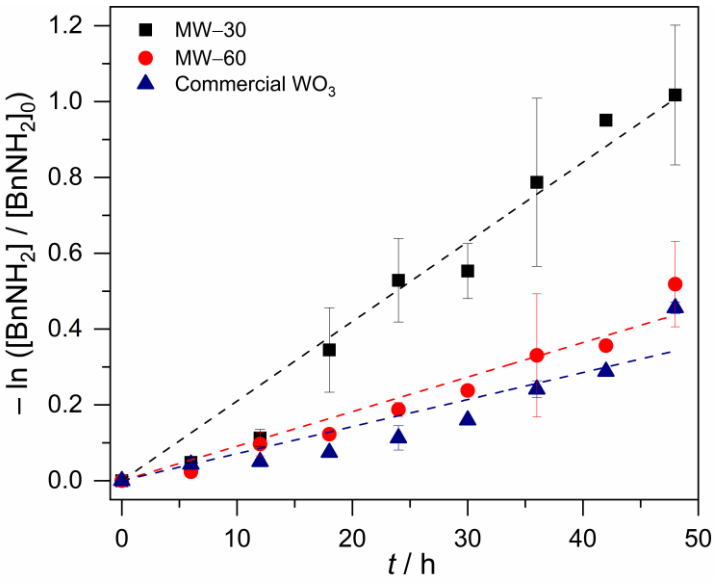

Figure 2.4 : First order rate plot for photocatalytic benzylamine oxidation on MW–30 (black squares), MW–60 (red circles), and bulk WO_3 - (blue triangles). Data are for 4 reactions performed with the full AM1.5G spectrum and water filters from a 150 W Xe arc lamp.

2.3.4 Photocatalytic Reactions with 1º Alcohols

In looking to address the state of energy-relevant catalytic conversions, a model substrate that has proven successful in being oxidized on metal oxides is benzyl alcohol.[34,35] As such, kinetics for photocatalytic benzyl alcohol oxidation to benzaldehyde served as a test case with visible light illumination according to the proposed balanced chemical equation in Scheme 2.3. All photochemical alcohol oxidations as to be described were performed using a single wavelength blue LED (460nm) with an average irradiance of 150 mW•cm^{-2}, to confirm the need for visible light to induce a successful reaction.

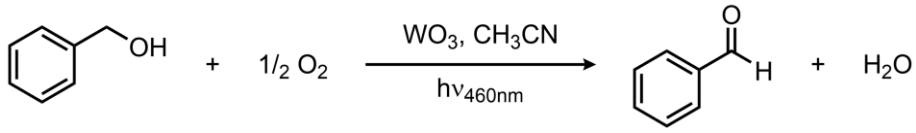

Scheme 2.3 : The balanced chemical equation for the photocatalytic oxidation of benzyl alcohol on WO_3 nanoparticles in air with acetonitrile as the solvent.

To again further demonstrate how particle size alters the reaction rate, photocatalytic tests were performed on the two extreme cases for particle size and catalytic rate as observed from the oxidation of benzylamine. Initial efforts to oxidize benzyl alcohol on MW–30 proved successful. When illuminated under O_2, a conversion of 16% was achieved after 3 days of illumination, corresponding to a rate constant of 2.6×10^{-3} h^{-1}. When this same reaction is performed on bulk WO_3 particles, the rate is much slower. By GC analysis, the disappearance of benzyl alcohol could not be measured as well as for the microwave particles (Figure A.11). However, the appearance of the single product benzaldehyde could be measured for this process. A trend is still observed as evidence in Figure 2.5, wherein the appearance of benzaldehyde is much faster for our microwave synthesized particles than on their commercial counterparts. At the end of the photocatalytic process there is a 3.5-fold increase in the yield of benzaldehyde for conversions performed on the smaller microwave synthesized particles than for the WO_3 of a larger scale (Figure A.12). Notable

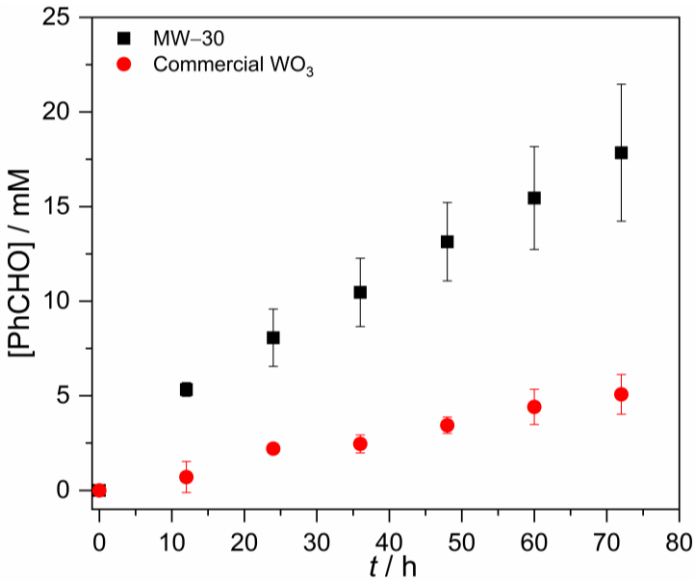

Figure 2.5 : Benzaldehyde production during the photocatalytic oxidation of benzyl alcohol on MW–30 (black squares) and bulk WO_3 (red circles) using 460 nm blue LEDs.

is that the control experiment—carrying out the reaction under an air-free N_2-filled atmosphere—results in no substrate conversion after 24 hours, showing the need for O_2 as a reductant in the reactions. Over the course of the 3-day reaction, the temperature varies from 22 – 25 ºC (Figure A.2), which is not different than the variation in room temperature. This result confirms the expected relationship that smaller particles with larger surface areas lead to faster photocatalysis.

As with the previously described photochemical analysis, high chemo-selectivity is achieved for the *benzaldehyde* product (Figure A.13); both catalysts have a selectivity of >99% benzaldehyde. After the 3-day reaction, the catalyst stability was also confirmed by recycling the catalyst. Over the course of five three-day reaction cycles, the recycled catalytic conversion presented in Figure 2.6 shows sustained stability and similar conversion over the first four successive catalytic cycles. At cycle 5, it is noted that the catalyst achieves the same average yield,

but a larger variance in the conversion. This behavior is explained by changes in the surface composition of the WO_3 during photocatalysis (*vide infra*).

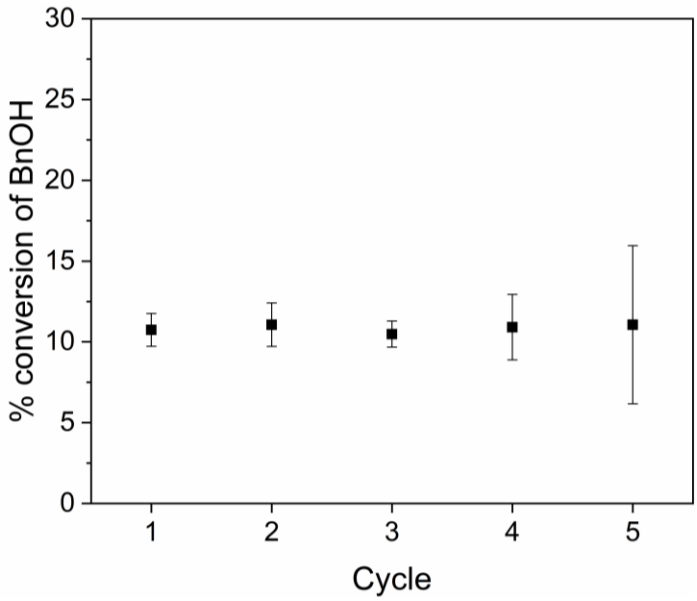

Figure 2.6 : Recyclability of WO_3 for photocatalytic oxidation of benzyl alcohol.

In the same regime of energy-relevant conversions, initial test reactions were performed in the oxidation of a common biomass derived compound. 5-(hydroxymethyl)-2-furaldehyde (HMF) is a well-known biomass derived product whose catalytic production from other known biomass feedstocks has seldom been explored. As well, unlike the substrates presented above, there are limited investigations into its further transformations into value-added chemicals like 2,5-diformylfuran (DFF)[36,37] and 2,5-furandicarboxylic acid (FDCA). As such, initial findings on the photocatalytic oxidation of HMF into DFF on the microwave synthesized WO_3 illuminated by blue LEDs are presented. Monitored by GC-MS, the first order rate data presented in Figure 2.7 shows a conversion rate constant, k of 0.01 h^{-1}. With a much faster reaction, the direct rate comparison can be made between our nanoscale particles and the larger particles purchased commercially. When compared to the bulk, commercial WO_3 counterpart the same trend as before is observed; the increased particle size is accompanied by a decrease in experimental photocatalytic rate. For

these commercial particles, the photocatalytic oxidation of HMF into DFF proceeds at a rate constant, k of 6.3×10^{-3} h^{-1}.

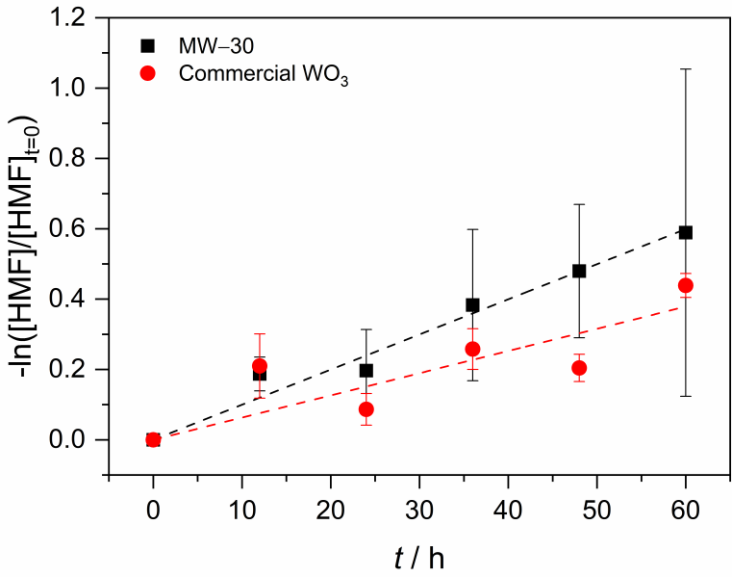

Figure 2.7 : First order rate plot for the photocatalytic oxidation of HMF on MW–30 (black squares) and bulkWO_3 (red circles) using 460 nm blue LEDs.

2.3.5 Phase, Morphology, and Electronic Structure after Photocatalysis

After alcohol photocatalysis, the suspended particles were separated from the reaction solution by centrifugation, washed with acetonitrile to remove any surface bound species, and dried overnight. The X-ray diffractograms remain unchanged from those of the as-synthesized materials. In addition, TEM imaging in Figure 2.8a reveals a retention of particle morphology with no observable change in particle size. The platelets are less agglomerated which allows for analyzing the particle size distribution here. The 23(9) nm × 19(7) nm dimensions are consistent with the diffraction data in Figure 2.1. The single crystalline nature of the WO_3 particles after photocatalysis remains clear from the TEM image in Figure 2.8b. The 0.385 nm lattice spacing corresponds to the (002) Bragg reflection of WO_3. The lack of particle degradation combined with steady kinetics suggests

that WO_3 synthesized by the described microwave-assisted method is photochemically stable for visible-light driven primary alcohol photocatalysis.

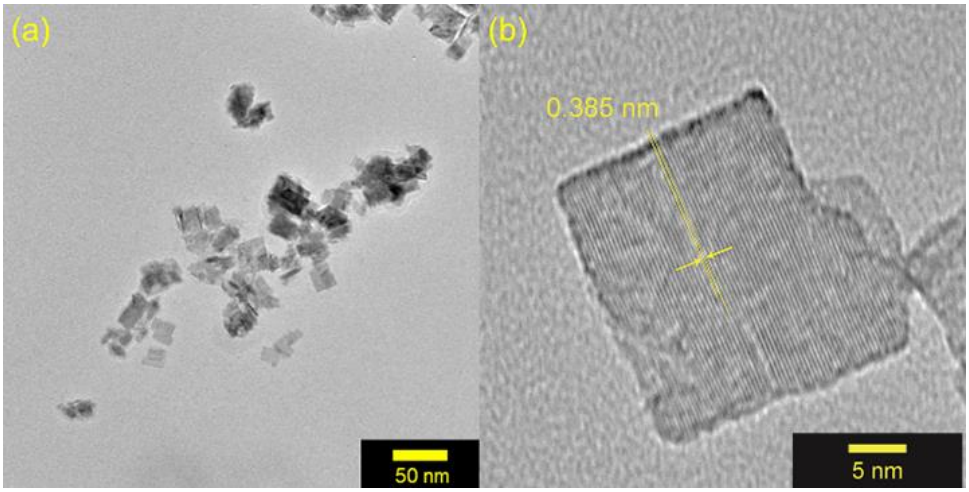

Figure 2.8 : (a) TEM images of MW–30 particles after photocatalysis on benzyl alcohol. **(b)** High resolution TEM image of a WO_3 nanoplatelet after photocatalysis.

Key changes to the material post photocatalysis reside in the distribution of electrons in W^{5+} and F^+ center defects. The post-photocatalysis EPR spectrum reveals an increase in the signals with *g* factors attributed to the presence of W^{5+} (Figure A.14), suggesting that during photocatalysis, more W^{6+} gets reduced to W^{5+}. This result is corroborated by XPS analysis (Figure A.15), where the W^{5+} content increases to 21.7%. This reduction is likely due to trapping conduction band electrons (formally W^{5+}) that cannot diffuse to the surface in order to participate in the coupled oxygen reduction reaction needed to complete the catalytic cycle. Accompanying this increase in W^{5+} content, XPS analysis of the O(1s) spectrum reveals the emergence of a new lower binding energy feature ascribed to weaker binding interactions between the oxygen and the W^{5+} cation.[38] This weak binding creates an environment with increased electron density around the oxygen participating and results in a peak shift to lower binding energy. To corroborate this claim, quantification of the oxygen content post photocatalysis was performed on this data wherein it is found that this

feature comprises 17.2% of the oxygen in this material. This result is in strong agreement with our presently reported results showing a 17.1% increase in the W^{5+} content from the as-synthesized material to the material post photocatalysis. As such, it is concluded that under illumination, F^+ centers ($V_O^{\bullet}$ in Kröger-Vink notation) which are EPR active, transfer an electron to the W(5d) conduction band (e'_{cb}) to give a non-EPR active oxygen vacancy ($V_O^{\bullet\bullet}$) with an increase in W^{5+} according to the reaction: $V_O^{\bullet} \rightarrow V_O^{\bullet\bullet} + e'_{cb}$.

To support this proposed reaction further, WO_3 was illuminated in presence of O_2, but in the absence of the 1° alcohol substrate. In agreement, a disappearance of the sharp EPR signal indicative of an F^+ center is observed (Figure A.16). With no substrate around to oxidize, the photogenerated carriers simply recombine in this case resulting in no changes to the tungsten valency or oxygen binding from the material pre-photolysis, as confirmed by XPS (Figure A.17). Comparatively, the commercial particles show no major change in W^{5+} content, only 0.7% after photocatalysis by XPS (Figure A.18). Therefore, the improved rates of photocatalysis are not solely due to the diminished particle size. Rather, the rate improvement also results from the increased W^{5+} and oxygen vacancy content that couples the oxidation of the primary alcohol substrate.

2.4 Conclusions

As detailed in this chapter, the fast and low-temperature synthesis of *crystalline* WO_3 nanoplatelets is successfully accomplished without the need for further heat treatment or additional surfactants beyond the solvent. By combining what is known about non-aqueous sol-gel chemistry and microwave heating techniques, particles on a nanoscale are easily achieved. Compared to their bulk counterparts, WO_3 nanoparticles show high photocatalytic activity towards the oxidation of benzylamine, benzyl alcohol, and HMF

upon illumination by visible light. The increased surface area affords faster catalytic rates without sacrificing stability. Though limitations in the efficiency of visible light absorption are present for WO_3, this route proves viable for investigating other small oxide photocatalysts. As well, these particles present themselves as a strong candidate for further exploration into the photocatalytic oxidation of biomass derived substrates into value chemicals.

2.5 References

1. Beatty, J. W.; Stephenson, C. R. J. Amine Functionalization via Oxidative Photoredox Catalysis: Methodology Development and Complex Molecule Synthesis. *Acc. Chem. Res.* **2015**, *48* (5), 1474–1484.

2. Yoon, T. P.; Ischay, M. A.; Du, J. Visible Light Photocatalysis as a Greener Approach to Photochemical Synthesis. *Nat. Chem.* **2010**, *2* (7), 527–532.

3. Prier, C. K.; Rankic, D. A.; MacMillan, D. W. C. Visible Light Photoredox Catalysis with Transition Metal Complexes: Applications in Organic Synthesis. *Chem. Rev.* **2013**, *113* (7), 5322–5363.

4. Augugliaro, V.; Camera-Roda, G.; Loddo, V.; Palmisano, G.; Palmisano, L.; Soria, J.; Yurdakal, S. Heterogeneous Photocatalysis and Photoelectrocatalysis: From Unselective Abatement of Noxious Species to Selective Production of High-Value Chemicals. *J. Phys. Chem. Lett.* **2015**, *6* (10), 1968–1981.

5. Lang, X.; Ma, W.; Zhao, Y.; Chen, C.; Ji, H.; Zhao, J. Visible-Light-Induced Selective Photocatalytic Aerobic Oxidation of Amines into Imines on TiO_2. *Chem. - A Eur. J.* **2012**, *18* (9), 2624–2631.V. Augugliaro, G. Camera-Roda, V. Loddo, G. Palmisano, L. Palmisano, J. Soria and S. Yurdakal, *J. Phys. Chem. Lett.*, 2015, 6, 1968–1981.

6. Abe, R.; Takami, H.; Murakami, N.; Ohtani, B. Pristine Simple Oxides as Visible Light Driven Photocatalysts: Highly Efficient Decomposition of Organic Compounds over Platinum-Loaded Tungsten Oxide. *J. Am. Chem. Soc.* **2008**, *130* (25), 7780–7781.

7. DePuccio, D. P.; Botella, P.; O'Rourke, B.; Landry, C. C. Degradation of Methylene Blue Using Porous WO_3, SiO_2–WO_3, and Their Au-Loaded Analogs: Adsorption and Photocatalytic Studies. *ACS Appl. Mater. Interfaces* **2015**, *7* (3), 1987–1996.

8. Lhermitte, C. R.; Garret Verwer, J.; Bartlett, B. M. Improving the Stability and Selectivity for the Oxygen-Evolution Reaction on Semiconducting WO_3 Photoelectrodes with a Solid-State FeOOH Catalyst. *J. Mater. Chem. A* **2016**, *4* (8), 2960–2968.

9. Liu, Y.; Li, J.; Li, W.; Yang, Y.; Li, Y.; Chen, Q. Enhancement of the Photoelectrochemical Performance of WO_3 Vertical Arrays Film for Solar Water Splitting by Gadolinium Doping. *J. Phys. Chem. C* **2015**, *119* (27), 14834–14842.

10. Dias, P.; Lopes, T.; Meda, L.; Andrade, L.; Mendes, A. Photoelectrochemical Water Splitting Using WO_3 Photoanodes: The Substrate and Temperature Roles. *Phys. Chem. Chem. Phys.* **2016**, *18* (7), 5232–5243.

11. Townsend, T. K.; Sabio, E. M.; Browning, N. D.; Osterloh, F. E. Photocatalytic Water Oxidation with Suspended Alpha-Fe_2O_3 Particles-Effects of Nanoscaling. *Energy Environ. Sci.* **2011**, *4* (10), 4270.

12. Sabio, E. M.; Chamousis, R. L.; Browning, N. D.; Osterloh, F. E. Photocatalytic Water Splitting with Suspended Calcium Niobium Oxides: Why Nanoscale Is Better than Bulk – A Kinetic Analysis. *J. Phys. Chem. C* **2012**, *116* (4), 3161–3170.

13. Niederberger, M.; Bartl, M. H.; Stucky, G. D. Benzyl Alcohol and Transition Metal Chlorides as a Versatile Reaction System for the Nonaqueous and Low-Temperature Synthesis of Crystalline Nano-Objects with Controlled Dimensionality. *J. Am. Chem. Soc.* **2002**, *124* (46), 13642–13643.

14. Magdalane, C. M.; Kaviyarasu, K.; Vijaya, J. J.; Siddhardha, B.; Jeyaraj, B. Photocatalytic Activity of Binary Metal Oxide Nanocomposites of CeO_2/CdO Nanospheres: Investigation of Optical and Antimicrobial Activity. *J. Photochem. Photobiol. B Biol.* **2016**, *163*, 77–86.

15. Sun, X.; Zhang, Y.-W.; Si, R.; Yan, C.-H. Metal (Mn, Co, and Cu) Oxide Nanocrystals from Simple Formate Precursors. *Small* **2005**, *1* (11), 1081–1086.

16. Zhou, K.; Wang, R.; Xu, B.; Li, Y. Synthesis, Characterization and Catalytic Properties of CuO Nanocrystals with Various Shapes. *Nanotechnology* **2006**, *17* (15), 3939–3943.

17. Hilaire, S.; Süess, M. J.; Kränzlin, N.; Bieńkowski, K.; Solarska, R.; Augustyński, J.; Niederberger, M. Microwave-Assisted Nonaqueous Synthesis of WO_3 Nanoparticles for Crystallographically Oriented Photoanodes for Water Splitting. *J. Mater. Chem. A* **2014**, *2* (48), 20530–20537.

18. *Microwaves in Organic Synthesis*, 3rd Edition.; de la Hoz, A., Loupy, A., Eds.; Wiley-VCH Verlag GmbH & Co. KGaA: Weinheim, Germany, 2012.

19. *Microwaves in Nanoparticle Synthesis*, S. Horikoshi, N. Serpone, Wiley-VCH Verlag GmbH & Co. KGaA: Weinheim, Germany, 2013.

20. Gawade, A. B.; Nakhate, A. V.; Yadav, G. D. Selective Synthesis of 2,5-Furandicarboxylic Acid by Oxidation of 5-Hydroxymethylfurfural over $MnFe_2O_4$ Catalyst. *Catal. Today* **2018**, *309*, 119–125.

21. Bilecka, I.; Niederberger, M. Microwave Chemistry for Inorganic Nanomaterials Synthesis. *Nanoscale* **2010**, *2* (8), 1358.

22. Bilecka, I.; Djerdj, I.; Niederberger, M. One-Minute Synthesis of Crystalline Binary and Ternary Metal Oxide Nanoparticles. *Chem. Commun.* **2008**, No. 7, 886–888.

23. Moorhead-Rosenberg, Z.; Harrison, K. L.; Turner, T.; Manthiram, A. A Rapid Microwave-Assisted Solvothermal Approach to Lower-Valent Transition Metal Oxides. *Inorg. Chem.* **2013**, *52* (22), 13087–13093.

24. Baek, S.; Yu, S.-H.; Park, S.-K.; Pucci, A.; Marichy, C.; Lee, D.-C.; Sung, Y.-E.; Piao, Y.; Pinna, N. A One-Pot Microwave-Assisted Non-Aqueous Sol–Gel Approach to Metal Oxide/Graphene Nanocomposites for Li-Ion Batteries. *RSC Adv.* **2011**, *1* (9), 1687.

25. Niederberger, M.; Garnweitner, G. Organic Reaction Pathways in the Nonaqueous Synthesis of Metal Oxide Nanoparticles. *Chem. - A Eur. J.* **2006**, *12* (28), 7282–7302.

26. Bilecka, I.; Elser, P.; Niederberger, M. Kinetic and Thermodynamic Aspects in the Microwave-Assisted Synthesis of ZnO Nanoparticles in Benzyl Alcohol. *ACS Nano* **2009**, *3* (2), 467–477.

27. Ma, G.; Chen, Z.; Chen, Z.; Jin, M.; Meng, Q.; Yuan, M.; Wang, X.; Liu, J.-M.; Zhou, G. Constructing Novel WO_3/Fe(III) Nanofibers Photocatalysts with Enhanced Visible-Light-Driven Photocatalytic Activity via Interfacial Charge Transfer Effect. *Mater. Today Energy* **2017**, *3*, 45–52.

28. Di Valentin, C.; Pacchioni, G. Spectroscopic Properties of Doped and Defective Semiconducting Oxides from Hybrid Density Functional Calculations. *Acc. Chem. Res.* **2014**, *47* (11), 3233–3241.

29. Breuhaus-Alvarez, A. G.; DiMeglio, J. L.; Cooper, J. J.; Lhermitte, C. R.; Bartlett, B. M. Kinetics and Faradaic Efficiency of Oxygen Evolution on Reduced H_xWO_3 Photoelectrodes. *J. Phys. Chem. C* **2019**, *123* (2), 1142–1150.

30. Meng, J.; Lin, Q.; Chen, T.; Wei, X.; Li, J.; Zhang, Z. Oxygen Vacancy Regulation on Tungsten Oxides with Specific Exposed Facets for Enhanced Visible-Light-Driven Photocatalytic Oxidation. *Nanoscale* **2018**, *10* (6), 2908–2915.

31. Bu, J.; Fang, J.; Leow, W. R.; Zheng, K.; Chen, X. Single-Crystalline Rutile TiO_2 Nano-Flower Hierarchical Structures for Enhanced Photocatalytic Selective Oxidation from Amine to Imine. *RSC Adv.* **2015**, *5* (126), 103895–103900.

32. Proctor, A. D.; Panuganti, S.; Bartlett, B. M. $CuWO_4$ as a Photocatalyst for Room Temperature Aerobic Benzylamine Oxidation. *Chem. Commun.* **2018**, *54* (9), 1101–1104.

33. Yuan, B.; Chong, R.; Zhang, B.; Li, J.; Liu, Y.; Li, C. Photocatalytic Aerobic Oxidation of Amines to Imines on $BiVO_4$ under Visible Light Irradiation. *Chem. Commun.* **2014**, *50* (98), 15593–15596.

34. Higashimoto, S.; Okada, K.; Morisugi, T.; Azuma, M.; Ohue, H.; Kim, T.-H.; Matsuoka, M.; Anpo, M. Effect of Surface Treatment on the Selective Photocatalytic Oxidation of Benzyl

Alcohol into Benzaldehyde by O_2 on TiO_2 Under Visible Light. *Top. Catal.* **2010**, *53* (7–10), 578–583.

35. Li, C.J.; Xu, G.-R.; Zhang, B.; Gong, J. R. High Selectivity in Visible-Light-Driven Partial Photocatalytic Oxidation of Benzyl Alcohol into Benzaldehyde over Single-Crystalline Rutile TiO2 Nanorods. *Appl. Catal. B Environ.* **2012**, *115–116*, 201–208.

36. Yurdakal, S.; Tek, B. S.; Alagöz, O.; Augugliaro, V.; Loddo, V.; Palmisano, G.; Palmisano, L. Photocatalytic Selective Oxidation of 5-(Hydroxymethyl)-2-Furaldehyde to 2,5-Furandicarbaldehyde in Water by Using Anatase, Rutile, and Brookite TiO_2 Nanoparticles. *ACS Sustain. Chem. Eng.* **2013**, *1* (5), 456–461.

37. Zhang, H.; Wu, Q.; Guo, C.; Wu, Y.; Wu, T. Photocatalytic Selective Oxidation of 5-Hydroxymethylfurfural to 2,5-Diformylfuran over Nb_2O_5 under Visible Light. *ACS Sustain. Chem. Eng.* **2017**, *5* (4), 3517–3523.

38. Liu, F.; Chen, X.; Xia, Q.; Tian, L.; Chen, X. Ultrathin Tungsten Oxide Nanowires: Oleylamine Assisted Nonhydrolytic Growth, Oxygen Vacancies and Good Photocatalytic Properties. *RSC Adv.* **2015**, *5* (94), 77423–77428.

Chapter 3

Microwave Synthesis of Ternary Spinel Ferrite Nanoparticles and the Effect of Annealing on Photocatalysis for $MgFe_2O_4$

Portions of this chapter were published:
McDonald, K. D.; Bartlett, B. M. *Inorg. Chem.* **2021**, *60*, 8704–8709

3.1 Introduction

In continuing to target and address alternative energy routes that do not rely on fossil fuels, utilization of solar energy remains as a growing force. Harnessing visible light is easily achieved with heterogeneous metal oxide semiconductors possessing appropriate band gaps to photocatalyze chemical reactions.[1-3] As was shown in Chapter 2, the nanoscaling of particles efficiently leads to improved photocatalytic activity. With an increased surface area and shorter diffusion length for photogenerated charge carriers, targeted chemical reactions are more easily achieved.[4] However, this system was hindered by non-ideal band positions an unable to transfer photogenerated electrons leading to a self-reduction process limiting the catalytic nature. In the face of this knowledge, research interest has shifted to those materials with more appropriate band energies for complete redox processes.

Metal ferrites with spinel structure (MFe_2O_4) have increasingly emerged as a strong collection of candidates with appropriate visible light harnessing capabilities, robust photostability, and stoichiometric tunability.[5-11,14] Transition metal ferrites (M = Co, Zn, Mn, etc.) have garnered prominent interest for studying the photochemical reactivity these materials possess. In aqueous conditions, organic pollutants can be degraded directly on the particles surface or indirectly by

photogenerated hydroxyl radicals.[5-7,9] In very few cases, the reactivity has been expanded into targeted selective organic oxidations for fuel production as a means to efficiently convert solar energy into a useful product.[12,13] While much of this initial work has been extensively covered to transition metal derivatives, those with non-transition metals have seen little exploration. To continue in understanding the robust reactivity for ferrites, this work seeks to better understand the characteristics possessed by magnesium ferrite. $MgFe_2O_4$ is an n-type semiconductor with known visible light absorbing capabilities and a band gap of 1.7-2.4 eV.[14]

Along with exploring what properties control the photochemical reactivity of $MgFe_2O_4$, an important facet to continue incorporating in this thesis is to determine the most efficient synthetic design for nanoparticle synthesis. As such the use of microwave heating in non-aqueous solvents is again sought to achieve rapid particle formation with growth control. Expanding into the ternary regime, and particularly for this material it is expected that external heating will be needed to impart crystallinity into the material.[15] As has been shown in previous studies, high temperature annealing of metal ferrites can lead to an inversion of the metal cations in the crystal structure. This is best represented by a more applicable formula of $(Mg_{1-\delta}Fe_{\delta})_{tet}[Mg_{\delta}\ Fe_{2-\delta}]_{oct}O_4$ where either cation can occupy both tetrahedral and octahedral sites dictated by the inversion parameter δ. When thermodynamically stable, most ferrites crystalize as either normal, where $\delta = 0$ (e.g. $ZnFe_2O_4$)[11,16], or inverse where $\delta = 1$ (e.g. $CoFe_2O_4$)[17,18]. $MgFe_2O_4$ is a less common ferrite that is most stable in a mixed inversion conformation ($\delta = 0.5 – 0.9$).

In all cases, the variability of this class of materials makes it even more ideal for understanding the robust nature across multiple iterations. This chapter presents the fast synthesis of crystalline spinel $MgFe_2O_4$ through rapid microwave heating and subsequent annealing. Utilizing ethanol nanocrystalline particles are achievable through the commonly predicted organic reaction

pathways. Under visible light illumination, the degradation of organic pollutants is possible on the surface of the particles. Variable reactivity arises from changes to the particles electronic and physical structure as the annealing temperature increases. Expansion of this synthetic protocols was also explored for this class of materials. The material preparation was modified to accommodate other ternary metal oxides belonging to this metal ferrite class. Namely the transition metal ferrites with spinel structures were tested for reproducibility using the method to be presented. In addition, those not belonging to the spinel class were also explored as they have similar properties of appropriate thermodynamic band potentials for carrying out redox processes and small band gaps to absorb visible light. Of focus in this sub-class are bismuth ferrites with perovskite ($BiFeO_3$)[19,20] and mullite ($Bi_2Fe_4O_9$)[20,21] structures. To highlight the thermodynamic and optical properties of interest, the band diagrams for each material to be synthesized is displayed in Figure 3.1.

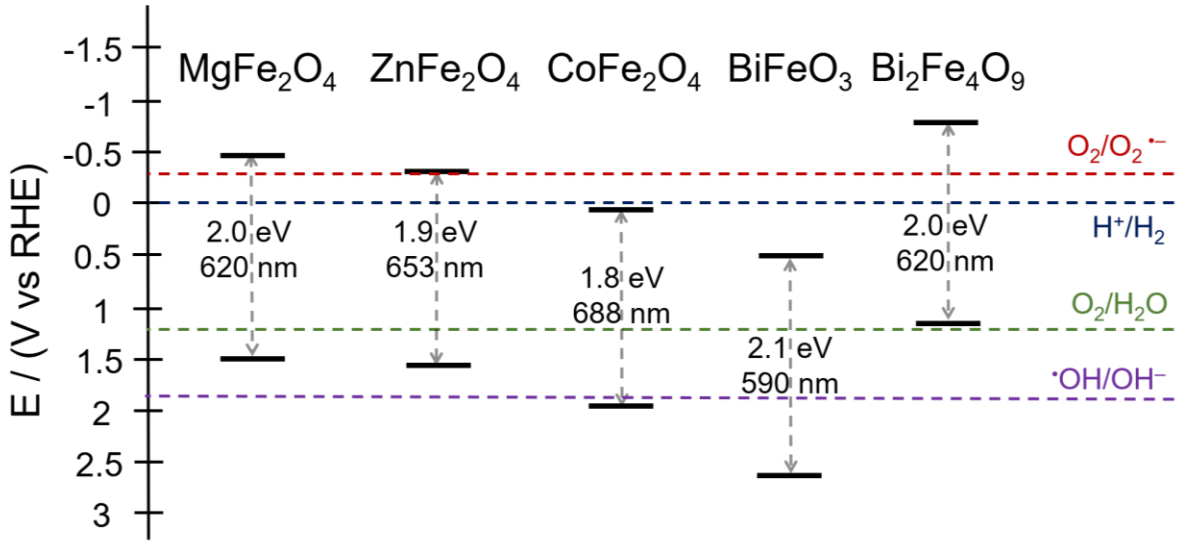

Figure 3.1 : Band structures for the ternary metal ferrite materials discussed in this chapter. Corresponding thermodynamic redox potentials for some targeted processes are shown.

3.2 Experimental Section

3.2.1 Materials

Magnesium acetylacetonate (TCI America, >98%), iron (III) acetylacetonate (Strem Chemicals, 99%), Cobalt (II) acetylacetonate (Alfa Aesar, >98%), Zinc acetylacetonate (Frontier Scientific, 99%), Bismuth (III) Nitrate Pentahydrate (Alfa Aesar, 98%), Iron (III) Nitrate Nonahydrate (Alfa Aesar, >98%), Coumarin (Alfa Aesar, 98%), Methylene blue trihydrate (MB) and ethanol (200 proof) were purchased from Fisher. Tetramethyl ammonium hydroxide pentahydrate (Acros Organics, 98%) was purchased from Sigma-Aldrich. All other chemicals were used as received. All procedures can be carried out safely with standard laboratory safety & chemical hygiene training.

3.2.2 Microwave Synthesis

In the typical synthesis of $MgFe_2O_4$, 0.9 mmol of magnesium acetylacetonate and 1.0 mmol of iron (III) acetylacetonate precursors were added to 5 mL of stirring ethanol. For all other metal ferrites, 0.6 mmol of metal acetylacetonate precursor was added. Separately, 2.0 mmol of tetramethylammonium hydroxide pentahydrate (Me_4NOH) was dissolved in another 5 mL of ethanol. The two solutions were mixed together in a glass microwave vial with an inner volume of 30 mL, sealed with a PTFE-lined cap. The mixture was sonicated for ~15 minutes to fully dissolve the dispersed precursors upon which a dark red solution was formed. During microwave heating, stirring was maintained with a magnetic stir bar in the reaction mixture at 800 rpm. The organic reaction was induced by automatic adjustments to the microwave power to rapidly heat the solution to 180°C (Figure B.1). This temperature is held constant for 15 minutes before being quenched with compressed air and cooled to room temperature. The temperature and pressure are controlled and maintained via an internal IR thermometer and pressure sensor, respectively. After irradiation,

the resulting precipitate is collected by centrifugation and thoroughly washed with ethanol(3x). The powders were dried in a vacuum oven (Fisher Scientific) at 60 °C overnight. Samples were annealed at their specified temperatures for 1 hour achieved with a heating rate of 10 °C•min^{-1}. All samples are denoted at by their annealing temperatures, *T* in ºC.

3.2.3 Material Characterization

The microwave experiments were conducted using an Anton Paar Monowave 400 synthesis reactor. Powder X-ray diffraction data (XRD) were collected on a Panalytical Empyrean diffractometer at a power of 1.8 kW (45 kV, 40 mA) with Cu Kα (λ = 1.5418 nm) radiation. The detector was a X'Celerator Scientific, a position sensitive 1D detector equipped with Bragg-BrentanoHD X-ray optic delivering only Kα radiation. Patterns were collected with a sampling step of 0.020 and a scan rate of 0.080°• s^{-1} while spinning at a rate of 0.25 Hz. Thermogravimetric analysis (TGA) was performed on a TA Q50 TGA with a platinum pan, heating rate of 10 °C min^{-1}, and a compressed air flow rate of 20 mL•min^{-1}. Transmission electron microscopy (TEM) and energy dispersive X-ray spectroscopy (EDX) was performed on a Thermo Fisher Talos F200x G2 high-resolution electron microscope operated at 200 kV. The samples were ground with a mortar and pestle and then suspended in ethanol. One drop of this suspension was deposited on a carbon grid and the ethanol was allowed to evaporate before sample imaging. Brunauer−Emmett−Teller (BET) surface area measurements of the catalysts were obtained on a Quantachrome NOVA4200e. A Varian Cary 5000 spectrophotometer equipped with an external diffuse reflectance accessory was used for UV-vis measurements. Spectra were collected in reflectance mode and transformed into absorbance using the Kubelka-Monk function. Barium sulfate was used as a 100% reflectance standard. Fluorescence and photoluminescence (PL) spectra were collected using a Horiba Quanta Master Fluorimeter with a Xe-arc lamp as the

excitation source. X-ray photoelectron spectroscopy (XPS) was performed on a Kratos Axis Ultra using a monochromatic Al source. Collected spectra were corrected for charging by referencing the C(1s) peak to 284.8 eV. All peaks were fitted in Casa XPS with the Shirley-type background.

3.2.4 Photocatalytic Activity Tests

A 10 ppm solution of MB was prepared in 18.2MΩ water (Millipore). Reactions were run in 30 mL quartz vials containing 20 mg of catalyst and 20 mL of MB solution. All photocatalytic reactions were carried out in front of a Newport-Oriel 150W Xe arc lamp solar simulator equipped with a 420 nm cut-on filter and water filter. Vials placed in front of the lamp received a front cell irradiance of 150mW•cm^{-2}. Prior to irradiation the solutions were stirred for an hour in the dark to establish an adsorption-desorption equilibrium. The reactions were then illuminated. To monitor the reaction progression, 3 mL aliquots were removed at 1-hour intervals and centrifuged at 4000 rpm for 3 minutes. The absorbance of the supernatant solution was monitored at 665 nm and the aliquot then reintroduced to the reaction solution.

3.3 Results and Discussion

3.3.1 Synthesis, Phase, and Surface Structure

Magnesium ferrite nanoparticles were achieved through rapid microwave heating and subsequent annealing to impart crystallinity. Prior literature examples showed that synthesis attempted using precursor stoichiometry resulted in lingering iron oxide impurities.[22] As such for this work an excess of magnesium precursor was employed to avoid the formation of these impurities upon annealing. The powder X-ray diffraction (PXRD) pattern for the resulting powders is shown in Figure 3.2. All of the diffraction peaks can be assigned to the spinel phase of $MgFe_2O_4$(PDF #88-1942). Energy dispersive X-ray spectroscopy confirms the ideal stoichiometry

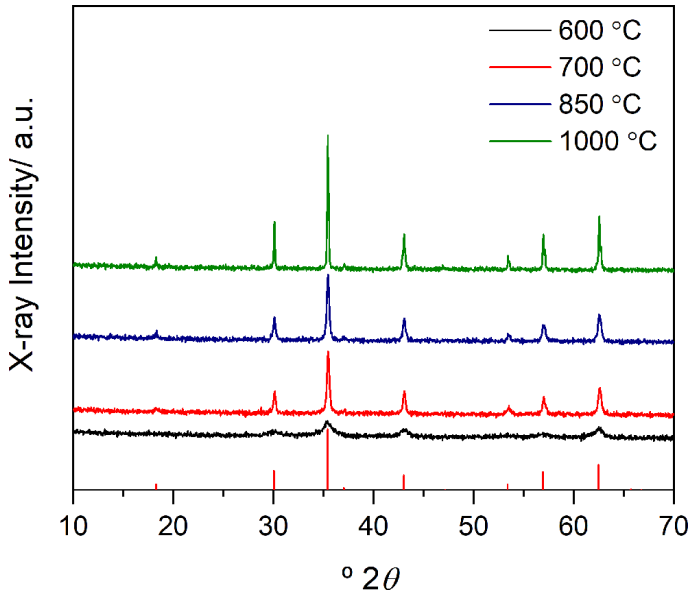

Figure 3.2 : Powder XRD pattern of $MgFe_2O_4$ nanoparticles annealed at 600 °C (black), 700 °C (red), 850 °C (blue), and 1000 °C (green) and reference pattern (vertical red lines) corresponding to spinel $MgFe_2O_4$.

for the ternary systems. The average domain size for each annealed sample calculated using the Scherrer equation on the (311) reflection, the inversion parameter from the Rietveld refinement, the lattice constant, band gap, and surface area from N_2 sorption isotherms are presented in Table 3.1. Transmission electron microscopy (TEM) of each sample agrees with the trend observed of increased domain size as the annealing temperature increases (Figure 3.3). The low particle size is

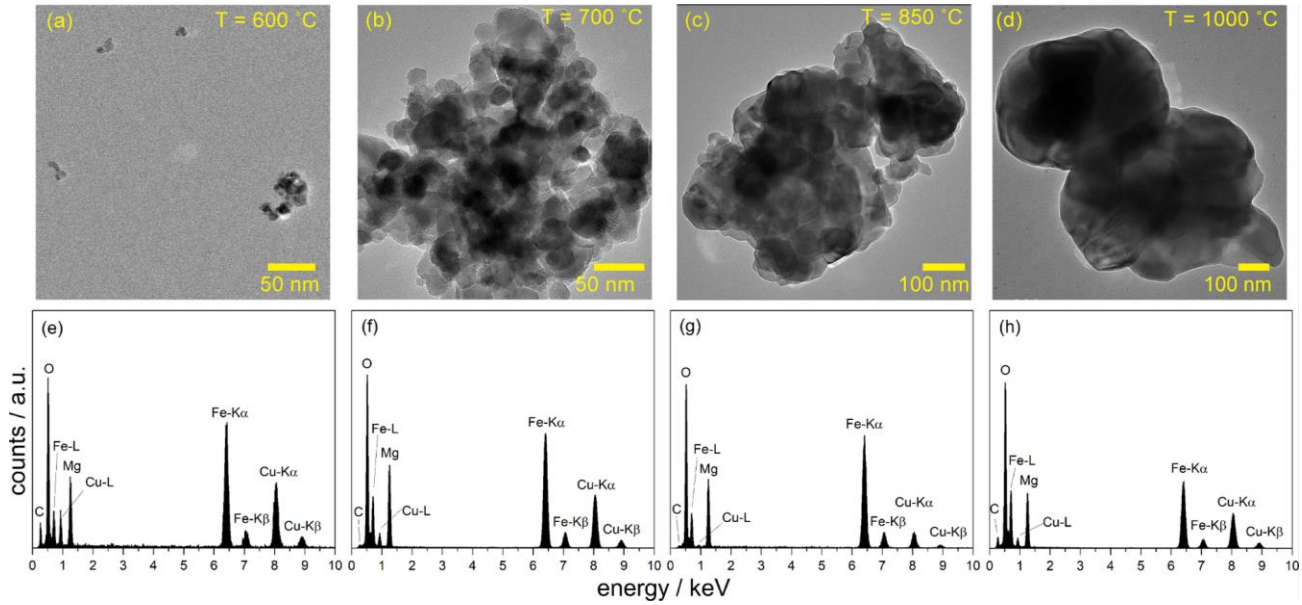

Figure 3.3 : (a–d) TEM images and **(e–h)** corresponding EDS spectra of $MgFe_2O_4$ particles.

retained from the capping of the particles during the synthesis from the tetramethylammonium hydroxide (Me_4NOH) mineralizer. The particles present as individual grains ~5-10 nm that begin to agglomerate at higher annealing temperatures; attributed to the loss of this Me_4NOH capping ligand. Infrared spectroscopy confirms this as C−H, N−H, bending modes and O−H stretches are found for the 600 ºC sample at ~1419 cm^{-1}, ~1494 cm^{-1}, and 3358 cm^{-1} respectively. (Figure B.2) As the higher temperatures are reached these features disappear from the spectra. As well thermal gravimetric analysis shows the corresponding mass loss for this phenomenon with two loss features beginning at 50 °C and again at 300°C. (Figure B.3)

3.3.2 Annealing Effects on Cation Inversion and Electronic Structure

As is found in the literature, it is expected that electronic changes will occur within the material corresponding to changes to the degree of inversion for each annealed sample.[11,23] First, the degree of cation inversion had to be determined with respect to each annealed sample. X-ray photoelectron spectroscopy confirms the appropriate oxidation state for magnesium and iron. The distribution of magnesium and iron across the octahedral and tetrahedral sites is observed for the surface of each sample through the deconvolution of the Mg(2p) and Fe(2p) XPS spectra (Figures B.4 – B.7). For each, tetrahedral and octahedral Mg^{2+} are assigned to 49 eV and 50 eV respectively and tetrahedral and octahedral Fe^{3+} to 712 eV and 710 eV; matching literature appointments.[10,23-24] Deconvolution of the O(1s) spectra gives peaks at 529.5 eV and 531 eV corresponding to the lattice M−O−M and surface M−O−H respectively. To obtain the δ_{RR} numerical inversion parameters of the bulk ferrites in Table 3.1, Rietveld refinement was carried out in GSAS-II software with EXPGUI interface[25] for the high crystalline 700, 850, and 1000 ºC samples (Figure B.8). As expected, the magnesium ferrite samples all present with inversion parameters indicative of mixed inversion but show an increase in δ_{RR} as the annealing temperature increases.

Physical and bulk compositional changes to the material upon annealing are presently shown to influence the behavior of the nano ferrites. In seeking to probe the trend in photochemical reactivity resulting from annealing temperature, however, it is imperative that the band gap for the material match what is expected, and that charge separation is possible. To first determine the band gap, UV-Vis diffuse reflectance spectroscopy was used. Through Tauc analysis, all of the band gaps (E_g) are ~ 2 eV, independent of annealing temperature (Figure B.9). These values are reported in Table 3.1.

Annealing Tempeature / ºC	$d_{Scherrer}$ / nm	δ_{RR}	*a* /Å	E_g / eV	SA_{BET} / $m^2\ g^{-1}$
600	7.3	—	—	2.01	118.1
700	26.8	0.49	8.394	1.99	72.3
850	27.5	0.62	8.395	1.97	105.4
1000	47.4	0.73	8.392	1.97	79.6

Table 3.1 : Crystallite Size, Inversion Parameter from Rietveld Refinement, Lattice Constant, Band Gap, and Surface Area of Annealed $MgFe_2O_4$ Samples

3.3.3 Photochemical Production of Reactive Hydroxyl Radicals and Determination of Band Energies

To better understand the ability for these particles to participate in photochemical conversions the formation of hydroxyl radicals was used to determine the oxidative ability of photogenerated holes. To detect hydroxyl radicals, a 2 mM solution of coumarin served as a radical trap forming 7-hydroxycoumarin, as detailed by the equation in Scheme 3.1.

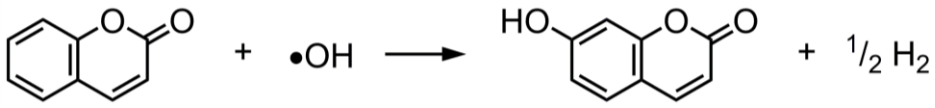

Scheme 3.1 : (a) Reaction scheme for the trapping of hydroxyl radicals with coumarin to for the fluorescent 7-hydroxycoumarin product.

The highly fluorescent nature of 7-hydroxycoumarin allows it to be detected using fluorescence spectroscopy with a prominent emission peak at 505 nm in a pH 8 solution, illustrated in Figure 3.4. The samples have the capacity to form hydroxyl radicals using their photogenerated holes, with the 600 ºC sample producing the most hydroxyl radical. This observation, however,

disagrees with the redox capabilities of $MgFe_2O_4$. The valence band maximum for $MgFe_2O_4$ (~1.4 V vs RHE)[14,26] lies at a potential less positive than the 1.9 V vs RHE[27] required to oxidize

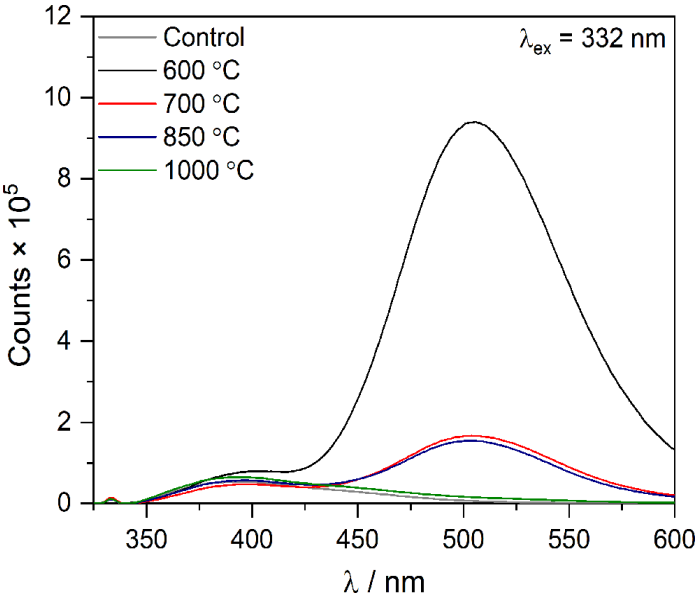

Figure 3.4 : Emission fluorescence spectra of a solution containing 2mM coumarin dye and no catalyst (gray) or $MgFe_2O_4$ nanoparticles annealed at 600 °C (black), 700 °C (red), 850 °C (blue), and 1000°C (green) after illumination with visible light. The peak at ~390 nm is from coumarin, and the peak at ~505 nm is attributed to 7-hydroxycoumarin.

hydroxide anion into hydroxyl radical or the 2.7 V vs RHE[27-28] required to oxidize water into hydroxyl radical. Valence band XPS analysis shows valence-band edges of ~1.4 – 1.5 eV for all annealed cases (Figure B.10). Coupled with the band gap of 2.0 eV, the corresponding conduction band edge is ~ –0.5 eV. This potential is sufficiently negative for the photogenerated electrons to reduce O_2 to O_2^- in solution (~ –0.35 V vs RHE).[27]

Given that the photogenerated holes do not have sufficient oxidizing power to oxidize the solution hydroxide anion into hydroxyl radical, this observed formation of •OH on this sample is attributed to the remaining presence of hydroxide on the surface. To corroborate this assessment, the $MgFe_2O_4$ nanoparticles annealed at 600 °C were washed with a 1 M HCl solution (2×) followed by a wash with Milli-Q water (2×). This acid wash allowed for the removal of the surface capping Me_4NOH species as evidenced by the FTIR spectra collected on the washed and dried powder

(Figure B.11). XRD was also performed on the acid-washed sample to ensure that there were no significant changes to the crystallographic nature of the sample. (Figure B.12). With these particles the above-described experiment was again performed to detect the formation of hydroxyl radical upon visible light illumination. The fluorescence spectra reveals that removing of the surface capping species indeed yields no hydroxyl radical formation from the photogenerated holes (Figure B.13). The hypothesis is confirmed that the capping species contributes to the oxidation of hydroxide anion into hydroxyl radical on the surface of the nanoparticles.

3.3.4 Benchmarking of $MgFe_2O_4$ Catalyst Performance Through Dye Degradation

The degradation of methylene blue dye was then used to benchmark the full-scale redox capabilities of the magnesium ferrite samples. Briefly 20 mg of catalyst were dispersed in 20 mL of a 10 ppm solution of the dye and allowed to stir for 1 hour before illumination to establish an adsorption/desorption equilibrium. The suspension was then illuminated under visible light (> 420 nm) and the rate monitored every hour to a total reaction time of 6 hours using the 665 nm absorbance feature. This process was also performed in the dark to ensure that dye degradation is indeed photocatalytic. (Figures B.14-B.15) The first order rate plots for this process are presented in Figure 3.5. The optimum annealing temperature to give the fastest rate is 600°C with a corresponding degradation rate of 0.061 h^{-1}. The photogenerated electrons are expected to facilitate dye degradation with formed reduced oxygen species. To confirm that the generated electrons are free to reduce adsorbed oxygen, XPS analysis of the Fe(2p) features was performed on the material after the full 6-hour degradation process for the sample annealed at 600 °C (Figure B.16). The primary peak for Fe $2p^{3/2}$ occurs the same binding energy of ~ 710.8 eV. Based on this result it is concluded that after catalysis, iron remains in the Fe^{3+} state rather than being reduced to Fe^{2+} by trapped electrons.

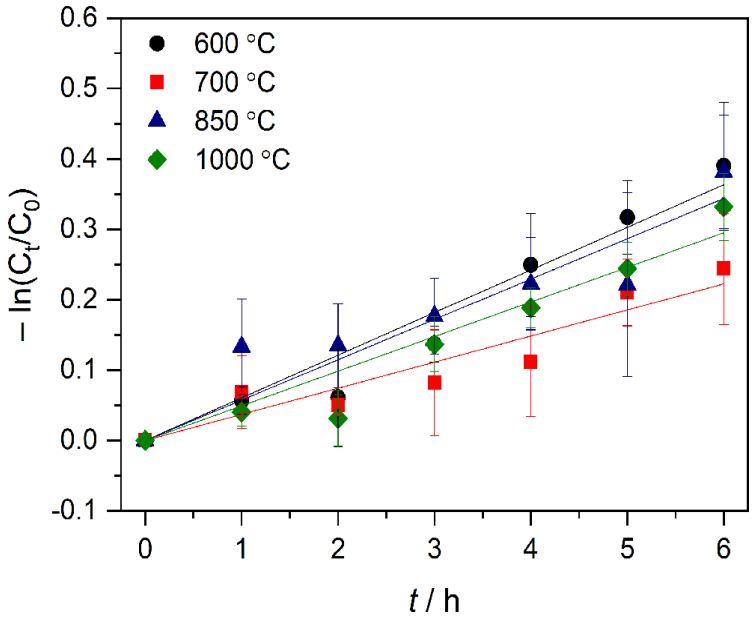

Figure 3.5 : First order rate plots for the photochemical degradation of methylene blue dye on $MgFe_2O_4$ nanoparticles annealed at 600 °C (black circles), 700 °C (red squares), 850 °C (blue triangles), and 1000 °C (green diamonds).

The remaining degradation rates do not follow a trend in accordance with annealing temperature. Rates of 0.057 h^{-1}, 0.049 h^{-1}, an 0.037 h^{-1} are calculated for samples annealed at 850 ºC, 1000 ºC, and 700 ºC respectively. The corresponding reactivity for the given particles, also does not follow expected trends for ternary metal ferrites with respect to their inversion parameter. As such, it is predicted that the primary influence on the reactivity is due to physical changes to the particles. As discussed, at this lower temperature of 600°C, there remains Me_4NOH capping the particles on the surface. As the sample is annealed to higher temperatures the removal of the capping ligand proceeds. With this immediate removal beyond the annealing temperature of 600 °C, the particles experience a stark agglomeration event creating small pores in the bulk particle structure; trapping remaining organic ligand. Continued heating to 850 °C aids in the release of this trapped ligand opening the pores and exposing more of the surface area. Eventually, the ligand removal completes and the application of a 1000 °C annealing temperature causes sintering of the particles. The obtained C1s XPS spectra are in agreement with this assessment. (Figures B.4-B.7)

Each spectrum shows a collection of three prominent features; adventitious carbon present at ~284.8 eV used for reference, a C–O/C–N features present at ~286 eV, and a C=O feature present at ~289 eV. The latter two features are assigned in accordance with the organic species present on the material. They present with high concentration for the initial sample annealed at 600 ºC and see a trending decrease for each successive sample. In relating the above calculated reaction rates to the observed surface area for each annealed sample, it is clear that the rate of degradation is highly influenced by the surface area of the $MgFe_2O_4$ particles (Figure B.17). The ability to maintain a small particle size and large surface area from the presented synthesis method allows for control of the reaction rate through simple changes to the physical nature of the nanoparticles.

3.3.5 Expanding the Synthetic Design of Ternary Metal Ferrites with Spinel Structures

With the appropriate synthetic scheme developed for $MgFe_2O_4$, the next steps for development in this class of ternary ferrite materials is to determine the protocol's suitability for other cations to replace magnesium. As was discussed in the introduction to this chapter, spinel ferrites with transition metal cations have been well studied for their photochemical redox activity. As such, the conclusions made from work completed in this chapter makes expansion to this regime of other ternary ferrites more useful. To begin attempting this, the magnesium acetylacetonate precursor presented in Section 3.2 was replaced with transition metal acetylacetonates belonging to cobalt and zinc. In brief, the same protocol was followed by dispersing the acetylacetonate precursors in ethanol with Me_4NOH mineralizer, rapidly heating the solution in the microwave, and subsequently annealing. For simplicity and ease of comparison, the samples were annealed at 600°C, the lowest necessary annealing temperature and most active sample of $MgFe_2O_4$. The powder XRD patterns for the resulting powders after annealing for $CoFe_2O_4$ (Figure 3.6a) and $ZnFe_2O_4$ (Figure 3.6b) match the respective assigned peaks for their spinel phases. The

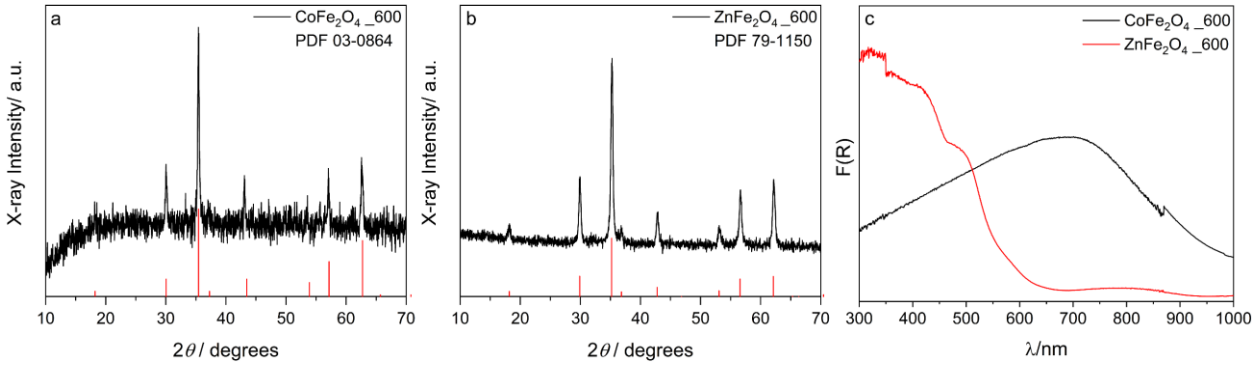

Figure 3.6 : Powder XRD pattern of **(a)** $CoFe_2O_4$ and **(b)** $ZnFe_2O_4$ nanoparticles synthesized and annealed at 600 °C. Corresponding references patterns (vertical red lines) are for the spinel phases. (c) UV-Vis diffuse reflectance spectra of $CoFe_2O_4$ (black) and $ZnFe_2O_4$ (red) nanoparticles annealed at 600 °C.

diffractogram peaks are sharper than what was received for $MgFe_2O_4$, indicating higher crystallinity and potentially larger particle grain size. In addition, UV-Vis diffuse reflectance spectroscopy is provided in Figure 3.6c to corroborate the formation of this material, matching absorption measurements and band gap analysis reported in the literature. This proposed protocol shows initial success in producing a range of ternary metal ferrites with the spinel structure.

As well, there are other ternary ferrite materials that possess interesting compositions and band gaps to fulfill the requirements of a visible light active, metal oxide photocatalyst. These materials of interest are bismuth ferrites with the formulas $BiFeO_3$ and $Bi_2Fe_4O_9$. For their synthesis, the corresponding nitrate salts of the metals was used in place of the acetylacetonate salts. The ethanol solvent and Me_4NOH mineralizer remained constant. Of interesting note for this class of materials, the starting precursor ratio highly influenced the composition and identity of the final material after annealing. As the bismuth loading content increased beyond the stoichiometric bounds, the amount of perovskite $BiFeO_3$ dominated over the mullite $Bi_2Fe_4O_9$. At higher loadings of bismuth (III) nitrate relative to iron (III) nitrate, $BiFeO_3$ would be the only phase present; with Bi_2O_3 emerging as the bismuth loading reached an extreme. This trend is best illustrated in Figure 3.7a of the corresponding powder XRD data with assigned reference patterns for each phase. A mix of the two phases could be achieved by accessing intermediate precursor concentrations. This

observation of precursor stoichiometry dependence is in direct disagreement with reports that compositional phase changes for these materials primarily occurs with adjustments to annealing temperature.[20] The optical nature is as well confirmed for these phases with the UV-Vis-diffuse reflectance spectra showing strong visible light absorption across a range of wavelengths (Figure 3.7b)

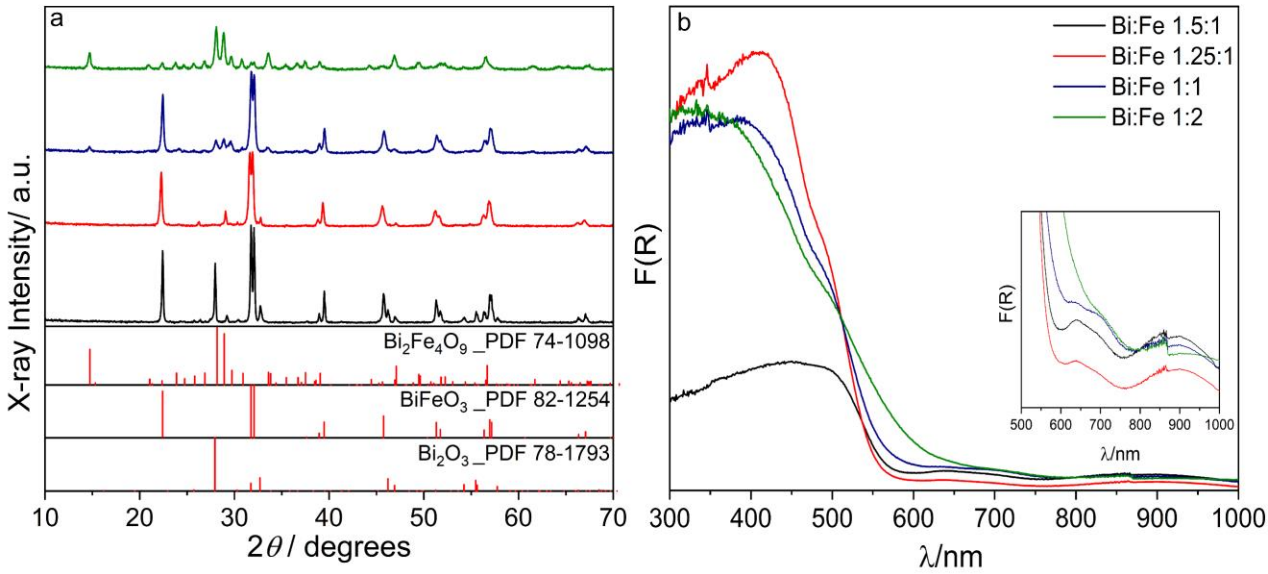

Figure 3.7 : (a) Powder XRD pattern of bismuth ferrite nanoparticles synthesized with Bi:Fe precursor ratios of 1.5:1 (black), 1.25:1 (red), 1:1 (blue), and 1:2 (green); annealed at 600 °C. Corresponding references patterns (vertical red lines) are for the orthorhombic-$Bi_2Fe_4O_9$, hexagonal-$BiFeO_3$, and tetragonal-Bi_2O_3 phases. **(b)** UV-Vis diffuse reflectance spectra of bismuth ferrite nanoparticles synthesized with different precursor ratios and annealed at 600 °C. The inset shows a zoomed in region of the spectra near the onset of absorption detailing minor absorption features for each sample.

3.4 Conclusions

In this chapter, the synthesis of metal oxide nanoparticles was expanded to those of ternary phases with prominent visible light absorption. Through rapid microwave heating in non-aqueous media magnesium ferrite nanoparticles are efficiently achieved. With the use of an added mineralizer and capping agent, the particles retain nano-scale size through the high temperature annealing needed to induce crystallization. Increased annealing temperatures is shown to alter the electronic and site ordering properties of the magnesium ferrites samples, similar to well-studied

transition metal ferrites. Hydroxide capping remaining on the surface through annealing allows for the formation of reactive hydroxyl radicals under visible light illumination. The formation of these radicals subsequently facilitates the degradation of a test methylene blue due solution. The synthetic protocol explored for $MgFe_2O_4$, proves to be applicable for other ternary metal ferrites with spinel crystal structures and with other crystal structures.

3.5 References

1. Augugliaro, V.; Camera-Roda, G.; Loddo, V.; Palmisano, G.; Palmisano, L.; Soria, J.; Yurdakal, S. Heterogeneous Photocatalysis and Photoelectrocatalysis: From Unselective Abatement of Noxious Species to Selective Production of High-Value Chemicals. *J. Phys. Chem. Lett.* **2015**, *6* (10), 1968–1981.

2. Lang, X.; Chen, X.; Zhao, J. Heterogeneous Visible Light Photocatalysis for Selective Organic Transformations. *Chem. Soc. Rev.* **2014**, *43* (1), 473–486.

3. Kou, J.; Lu, C.; Wang, J.; Chen, Y.; Xu, Z.; Varma, R. S. Selectivity Enhancement in Heterogeneous Photocatalytic Transformations. *Chem. Rev.* **2017**, *117* (3), 1445–1514.

4. McDonald, K. D.; Bartlett, B. M. Photocatalytic Primary Alcohol Oxidation on WO_3 Nanoplatelets. *RSC Adv.* **2019**, *9* (49), 28688–28694.

5. Cao, S.-W.; Zhu, Y.-J.; Cheng, G.-F.; Huang, Y.-H. $ZnFe_2O_4$ Nanoparticles: Microwave-Hydrothermal Ionic Liquid Synthesis and Photocatalytic Property over Phenol. *J. Hazard. Mater.* **2009**, *171* (1–3), 431–435.

6. Fu, Y.; Wang, X. Magnetically Separable $ZnFe_2O_4$–Graphene Catalyst and Its High Photocatalytic Performance under Visible Light Irradiation. *Ind. Eng. Chem. Res.* **2011**, *50* (12), 7210–7218.

7. Fu, Y.; Chen, H.; Sun, X.; Wang, X. Combination of Cobalt Ferrite and Graphene: High-Performance and Recyclable Visible-Light Photocatalysis. *Appl. Catal. B Environ.* **2012**, *111–112*, 280–287.

8. Dom, R.; Chary, A. S.; Subasri, R.; Hebalkar, N. Y.; Borse, P. H. Solar Hydrogen Generation from Spinel $ZnFe_2O_4$ Photocatalyst: Effect of Synthesis Methods. *Int. J. Energy Res.* **2015**, *39* (10), 1378–1390.

9. Jesudoss, S. K.; Vijaya, J. J.; Kennedy, L. J.; Rajan, P. I.; Al-Lohedan, H. A.; Ramalingam, R. J.; Kaviyarasu, K.; Bououdina, M. Studies on the Efficient Dual Performance of $Mn_{1-x}Ni_xFe_2O_4$ Spinel Nanoparticles in Photodegradation and Antibacterial Activity. *J. Photochem. Photobiol. B Biol.* **2016**, *165* (7), 121–132.

10. Guijarro, N.; Bornoz, P.; Prévot, M.; Yu, X.; Zhu, X.; Johnson, M.; Jeanbourquin, X.; Le Formal, F.; Sivula, K. Evaluating Spinel Ferrites MFe_2O_4 (M = Cu, Mg, Zn) as Photoanodes for Solar Water Oxidation: Prospects and Limitations. *Sustain. Energy Fuels* **2018**, *2* (1), 103–117.

11. Li, Y.; Li, Y.; Xu, X.; Ding, C.; Chen, N.; Ding, H.; Lu, A. Structural Disorder Controlled Oxygen Vacancy and Photocatalytic Activity of Spinel-Type Minerals: A Case Study of $ZnFe_2O_4$. *Chem. Geol.* **2019**, *504*, 276–287.

12. Bilecka, I.; Kubli, M.; Amstad, E.; Niederberger, M. Simultaneous Formation of Ferrite Nanocrystals and Deposition of Thin Films via a Microwave-Assisted Nonaqueous Sol–Gel Process. *J. Sol-Gel Sci. Technol.* **2011**, *57* (3), 313–322.

13. Gawade, A. B.; Nakhate, A. V.; Yadav, G. D. Selective Synthesis of 2, 5-Furandicarboxylic Acid by Oxidation of 5-Hydroxymethylfurfural over $MnFe_2O_4$ Catalyst. *Catal. Today* **2018**, *309*, 119–125.

14. Taffa, D. H.; Dillert, R.; Ulpe, A. C.; Bauerfeind, K. C. L.; Bredow, T.; Bahnemann, D. W.; Wark, M. Photoelectrochemical and Theoretical Investigations of Spinel Type Ferrites ($M_xFe_{3-x}O_4$) for Water Splitting: A Mini-Review. *J. Photonics Energy* **2016**, *7* (1), 012009.

15. Xavier, C. S.; Candeia, R. A.; Bernardi, M. I. B.; Lima, S. J. G.; Longo, E.; Paskocimas, C. A.; Soledade, L. E. B.; Souza, A. G.; Santos, I. M. G. Effect of the Modifier Ion on the Properties of $MgFe_2O_4$ and $ZnFe_2O_4$ Pigments. *J. Therm. Anal. Calorim.* **2007**, *87* (3), 709–713.

16. Mozaffari, M.; Eghbali Arani, M.; Amighian, J. The Effect of Cation Distribution on Magnetization of $ZnFe_2O_4$ Nanoparticles. *J. Magn. Magn. Mater.* **2010**, *322* (21), 3240–3244.

17. Chandramohan, P.; Srinivasan, M. P.; Velmurugan, S.; Narasimhan, S. V. Cation Distribution and Particle Size Effect on Raman Spectrum of $CoFe_2O_4$. *J. Solid State Chem.* **2011**, *184* (1), 89–96.

18. Safi, R.; Ghasemi, A.; Shoja-Razavi, R.; Ghasemi, E.; Sodaee, T. Rietveld Structure Refinement, Cations Distribution and Magnetic Features of $CoFe_2O_4$ Nanoparticles Synthesized by Co-Precipitation, Hydrothermal, and Combustion Methods. *Ceram. Int.* **2016**, *42* (5), 6375–6382.

19. Lam, S. M.; Sin, J. C.; Mohamed, A. R. A Newly Emerging Visible Light-Responsive $BiFeO_3$ perovskite for Photocatalytic Applications: A Mini Review. *Mater. Res. Bull.* **2017**, *90*, 15–30.

20. Zhang, T.; Shen, Y.; Qiu, Y.; Liu, Y.; Xiong, R.; Shi, J.; Wei, J. Facial Synthesis and Photoreaction Mechanism of $BiFeO_3/Bi_2Fe_4O_9$ Heterojunction Nanofibers. *ACS Sustain. Chem. Eng.* **2017**, *5* (6), 4630–4636.

21. Wu, T.; Liu, L.; Pi, M.; Zhang, D.; Chen, S. Enhanced Magnetic and Photocatalytic Properties of $Bi_2Fe_4O_9$ Semiconductor with Large Exposed (001) Surface. *Appl. Surf. Sci.* **2016**, *377*, 253–261.

22. Kirchberg, K.; Becker, A.; Bloesser, A.; Weller, T.; Timm, J.; Suchomski, C.; Marschall, R. Stabilization of Monodisperse, Phase-Pure $MgFe_2O_4$ Nanoparticles in Aqueous and Nonaqueous Media and Their Photocatalytic Behavior. *J. Phys. Chem. C* **2017**, *121* (48), 27126–27138.

23. Zhu, X.; Guijarro, N.; Liu, Y.; Schouwink, P.; Wells, R. A.; Le Formal, F.; Sun, S.; Gao, C.; Sivula, K. Spinel Structural Disorder Influences Solar-Water-Splitting Performance of $ZnFe_2O_4$ Nanorod Photoanodes. *Adv. Mater.* **2018**, *30* (34), 1801612.

24. Suchomski, C.; Breitung, B.; Witte, R.; Knapp, M.; Bauer, S.; Baumbach, T.; Reitz, C.; Brezesinski, T. Microwave Synthesis of High-Quality and Uniform 4 Nm $ZnFe_2O_4$ Nanocrystals for Application in Energy Storage and Nanomagnetics. *Beilstein J. Nanotechnol.* **2016**, *7* (1), 1350–1360.

25. Toby, B. H.; Von Dreele, R. B. GSAS-II : The Genesis of a Modern Open-Source All Purpose Crystallography Software Package. *J. Appl. Crystallography.* **2013**, *46* (2), 544–549.

26. Dillert, R.; Taffa, D. H.; Wark, M.; Bredow, T.; Bahnemann, D. W. Photoelectrochemical Water Splitting and Photocatalytic Hydrogen Production Using Ferrites (MFe_2O_4) under Visible Light Irradiation. *APL Mater.* **2015**, *3* (10), 104001.

27. Armstrong, D. A.; Huie, R. E.; Koppenol, W. H.; Lymar, S. V.; Merényi, G.; Neta, P.; Ruscic, B.; Stanbury, D. M.; Steenken, S.; Wardman, P. Standard Electrode Potentials Involving Radicals in Aqueous Solution: Inorganic Radicals. *Pure Appl. Chem.* **2015**, *87* (11–12), 1139–1150.

28. Wardman, P. Reduction Potentials of One-Electron Couples Involving Free Radicals in Aqueous Solution. *J. Phys. Chem. Ref. Data* **1989**, *18* (4), 1637–1755.

Chapter 4

Improving the Stability of Cadmium Selenide Through Core@Shell Structures for Photochemical Alcohol Oxidations

4.1 Introduction

Chapters 2 and 3 discussed and highlighted how metal oxide materials are easily synthesized through non-aqueous and microwave assisted routes. Their photochemical activity was accessible under visible light illumination and in this photoactive capacity they were able to perform useful redox reactions in the space of biomass upgrading and environmental remediation. However, even on the nanoscale they are harder for broader implementation. On their own, they are still limited by drawbacks from poor charge separation and charge. In some cases, as with the WO_3 nanoplatelets presented in Chapter 2, they do not possess enough thermodynamic energy to complete both redox half reactions. A way around this, is to explore the reactivity of photocatalytic materials not containing oxygen with more ideal electronic properties.

Metal chalcogenide materials with the formula M_xE_y; where M is a transition metal and E is a chalcogen (i.e. S, Se, Te); represent another class of well-studied semiconductor materials with direct band gaps.[1] Similar to metal oxides, these materials have been investigated towards organic dye degradation[2], solar fuel production[3], and general organic C-C bond formation reactions.[4] As well, they have shown great utility and exploration in the realm of biomass upgrading through alcohol oxidations. When adhered to the surface of other active catalysts as a composite they are even able to facilitate the proton reduction half reaction in making hydrogen (H_2) gas.[5] However, major drawbacks to utilizing these materials arise from their photo-corrosion in aerobic aqueous

solutions. While it is not clearly known what leads to this degradation, research has speculated that the corrosion results from either the presence of O_2 or reactive intermediates formed during photo-catalyzed water splitting (Scheme 4.1).[6-7] Even still in non-aqueous systems, similar corrosion is experienced accompanied by the leaching of toxic elements into solution.[8] To combat this

Scheme 4.1 : Reaction scheme of the dissolution of cadmium sulfide under aerobic conditions.

corrosion, altering the surface of these materials will be crucial to preventing any corrosion and loss of overall catalytic reactivity.

Given the high stability and recyclability of metal oxides, it stands to reason that they make good candidates for surface functionalization. Next steps lie, in how to incorporate this metal oxide into the structure. Composite materials as those previously mentioned still allow for the degradation pathways to be accessed. The key in this hypothesis relies on minimal to no exposure of the reaction solution to the chalcogenide surface. With this idea, a core@shell structure comes to mind. Having shown some success for bulk particles, the same material alteration will be explored for particles on the nanoscale.[9-12] Through various routes an oxide shell can be grown on the surface of the chalcogenide nanoparticles as they are made. In this design plan, a major goal

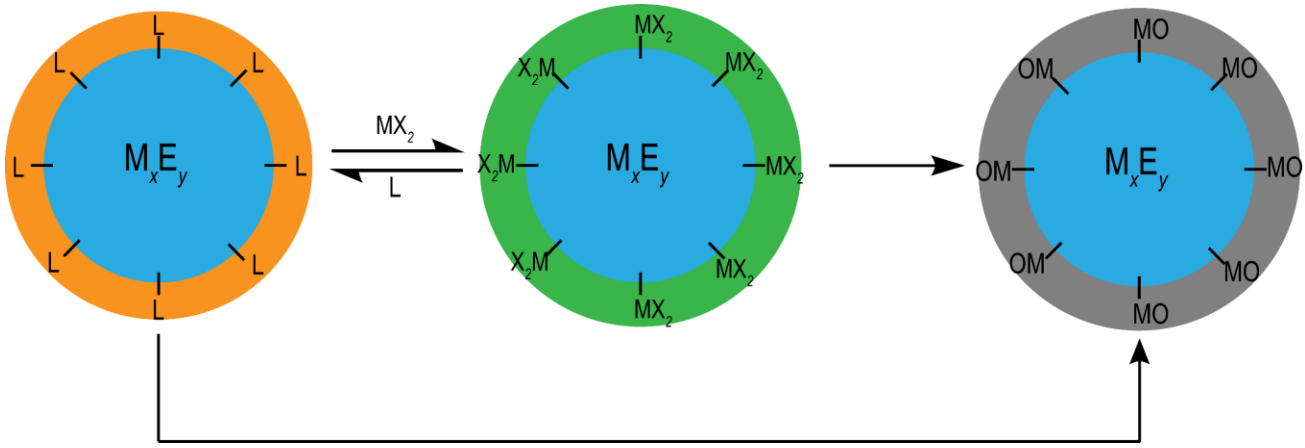

Figure 4.1 : Schematic for the formation of a metal oxide (MO) shell around a metal chalcogenide (M_xE_y) core. From left to right are the metal chalcogenide synthesized with an L-type ligand (L), exchange for a Z-type ligand (MX_2), and formation of the final oxide shell.

will be to retain the optical and electronic nature of the metal chalcogenide, possible with a thin oxide shell. Two types of routes undertaken are depicted in Figure 4.1: *(1) a one-step route from the organic L-type ligand and (2) a two-step route facilitated by a ligand exchange with a Z-type ligand in the form of the metal salt of interest.*

Buhro and coworkers have extensively studied the initial steps for the displayed two-step mechanism on cadmium selenide (CdSe).[13-15] Their synthetic approach to CdSe quantum dots is undertaken using a surfactant assisted method. Here-in, the surface capping L-type amine ligands form a shell around the surface of the particles and protect the surface from the surrounding solution. Recently, their research has shown that these L-type surfactants can easily be displaced with Z-type ligands, commonly metal salts.[16-17] Successful displacement of the ligand can be confirmed using infrared (IR) spectroscopy and powder X-ray diffraction. With the new metal salt capping the quantum dots, utilizing the low temperature non-aqueous approach detailed in the previous chapters can convert the salt into the metal oxide. With the oxide coated CdSe, their photochemical stability can be measured when performing photo-driven organic oxidations in aqueous and non-aqueous media. This chapter will briefly discuss the photocatalytic implications a metal oxide shell will have on CdSe nanoparticles when performing the oxidation of 2-mercaptoethanol. To further develop this science a collaboration with the Buhro Lab will explore the stability of their coated quantum belts by performing an oxidation of benzyl alcohol.

4.2 Experimental Section

4.2.1 Materials

Cadmium chloride (99.9%), Selenium powder (99.5%), Titanium (IV) isopropoxide (97%), Octylamine (99%), Oleylamine (70%), 2-mercaptoethanol (>99%), chlorobenzene (99+%, for spectroscopy), and tetramethyl ammonium hydroxide pentahydrate (Acros Organics, 98%) were

purchased from Sigma-Aldrich. Trioctlphosphine (Alfa Aesar, 90%), benzyl alcohol (Certified ACS), and ethanol (200 proof) were purchased from Fisher. All other chemicals were used as received. All procedures can be carried out safely with standard laboratory safety & chemical hygiene training.

4.2.2 Metal Chalcogenide Synthesis

For the microwave synthesis of cadmium selenide nanoparticles, 1.5 mmol of cadmium chloride and 4.5 mmol of selenium powder were added to a glass microwave vial with an inner volume of 30 mL under an N_2 atmosphere. To this, 7.5 mL of octylamine and 7.5 mL of oleylamine were added and the vessel was sealed with a PTFE-lined cap. During microwave heating, stirring was maintained with a magnetic stir bar in the reaction mixture at 800 rpm. The organic reaction was induced by automatic adjustments to the microwave power to heat the solution to 100°C, over a 14-minute period (Figure C.1). This temperature is held constant for 2 hours before being quenched with compressed air and cooled to room temperature. The temperature and pressure are controlled and maintained via an internal IR thermometer and pressure sensor, respectively. After irradiation, the product was precipitated by addition of ethanol containing trioctylphosphine (TOP) and collected by centrifugation. The powder was thoroughly washed with the ethanol/TOP mixture (2x) and pure ethanol (2x). The powders were dried in a vacuum oven (Fisher Scientific) at 80 °C overnight. This powder is labeled CdSe@amine. Cadmium selenide quantum belts were obtained from collaborators Professor William Buhro and Dr. Yuewei Yao; prepared separately.

4.2.3 Synthesis of Metal Oxide Coated CdSe Nanoparticles

Exchange of the surface ligand was performed by first dispersing the CdSe@amine in toluene under sonication. Separately, two stoichiometric equivalents of titanium isopropoxide was dissolved in ethanol. The two solutions were mixed together and allowed to stir for 10 minutes to

promote the exchange following the addition of two equivalents tetramethylammonium hydroxide. The final powder was collected by centrifugation, washed with a 50/50 ethanol/toluene mixture (3x) and dried overnight. This material is denoted as CdSe@$Ti(OH)_4$. Finally, the oxide shell was formed using microwave irradiation. The intermediate CdSe@$Ti(OH)_4$ powder was dispersed in 10 mL of ethanol in a 30 mL glass microwave vial and the vessel was sealed with a PTFE-lined cap. During microwave heating, stirring was maintained with a magnetic stir bar in the reaction mixture at 800 rpm. The organic reaction was induced by automatic adjustments to the microwave power to rapidly heat the solution to 160°C (Figure C.2). This temperature is held constant for 30 minutes before being quenched with compressed air and cooled to room temperature. The powder was thoroughly washed with ethanol (3x) and dried in a vacuum oven (Fisher Scientific) at 80 °C overnight. This final material is denoted as CdSe@TiO_2.

4.2.4 Material Characterization

The microwave experiments were conducted using an Anton Paar Monowave 400 synthesis reactor. Powder X-ray diffraction data (XRD) were collected on a Panalytical Empyrean diffractometer at a power of 1.8 kW (45 kV, 40 mA) with Cu Kα (λ = 1.5418 nm) radiation. The detector was a X'Celerator Scientific, a position sensitive 1D detector equipped with Bragg-BrentanoHD X-ray optic delivering only Kα radiation. Patterns were collected with a sampling step of 0.020 and a scan rate of 0.080°• s^{-1} while spinning at a rate of 0.25 Hz. Energy dispersive X-ray fluorescence spectroscopy (EDXRF) was performed on a Thermo Scientific ARL Quant'X EDXRF Spectrometer. X-ray photoelectron spectroscopy (XPS) was performed on a Kratos Axis Ultra using a monochromatic Al source. Collected spectra were corrected for charging by referencing the C(1s) peak to 284.8 eV. All peaks were fitted in Casa XPS with the Shirley-type background.

4.2.5 Photocatalytic Activity and Stability Tests

Photocatalytic oxidation of 2-mercaptoethanol was carried out using narrow linewidth blue LEDs (460 nm) with an irradiance of ~150 mW•cm^{-2}. Reactions were capped with a rubber septum; and kept under an O_2 atmosphere using balloons. Reactions were run in 4 mL glass dram vials containing 10 mg of catalyst and 2 mL of 100 mM substrate solution in acetonitrile or 18.2MΩ water (Millipore). For the aqueous reactions, the pH was adjusted to 8 using 1M NaOH. Photocatalytic oxidation of benzyl alcohol was carried out in front of a Newport-Oriel 150W Xe arc lamp solar simulator equipped with a water filter. Vials placed in front of the lamp received a front cell irradiance of 200mW•cm^{-2}. A fan was used to keep the reaction at room temperature. Reactions were run in 4 mL glass dram vials containing 10 mg of catalyst and 2 mL of 250 mM substrate solution in acetonitrile. Prior to irradiation, all solutions were stirred for an hour in the dark to establish an adsorption-desorption equilibrium before having an aliquot taken out to determine the initial concentration of substrate in each solution. Reaction progression was monitored by GC with a flame ionization detector on a Trace 1310 GC-FID system with a TG-5MS Amine column. Argon was used as the carrier gas. Data were collected with chlorobenzene as an internal standard and were then converted to first order rate plots where specified. Product analysis for the oxidation of 2-mercaptoethanol was performed using ^{1}H NMR spectroscopy with sodium formate as an internal standard in D_2O. Before NMR analysis, each reaction was filtered through a nylon syringe filter to remove the catalyst. ^{1}H NMR data was collected on a Varian MR400 NMR spectrometer equipped with a Varian 5 mm PFG AutoX Dual Broadband probe.

4.2.6 Leaching Detection Tests

Cadmium, selenium, and titanium concentrations in the post photocatalysis solution were determined via inductively coupled plasma mass spectrometry (ICP-MS) using a PerkinElmer

Nexion 2000 ICP-MS instrument. The post-photocatalysis suspension was filtered through a syringe filter. A known aliquot of this solution was dissolved in Milli-Q water and filtered through a new syringe filter. Samples were referenced to an external standard (20 ppb) on indium, yttrium, and scandium respectively. Concentrations were determined via a series of standard solutions prepared from a 1000 ppm Cd, Se, or Ti reference solution (Sigma-Aldrich).

4.3 Results and Discussion

4.3.1 Microwave Synthesis of CdSe Nanoparticles and Observation of their Photochemical Instability

Cadmium selenide (CdSe) was synthesized through microwave heating of cadmium chloride and excess elemental selenium in organic surfactant media. Powder X-ray diffraction (pXRD) for the resulting powders, shown in Figure 4.2, shows diffraction peaks matching the assigned wurtzite phase. Energy dispersive X-ray fluorescence spectroscopy (EDXRF) reveals near ideal stoichiometry with cadmium to selenium ratios of ~1:0.8. With confirmation that the material has formed its photochemical activity and stability can be monitored.

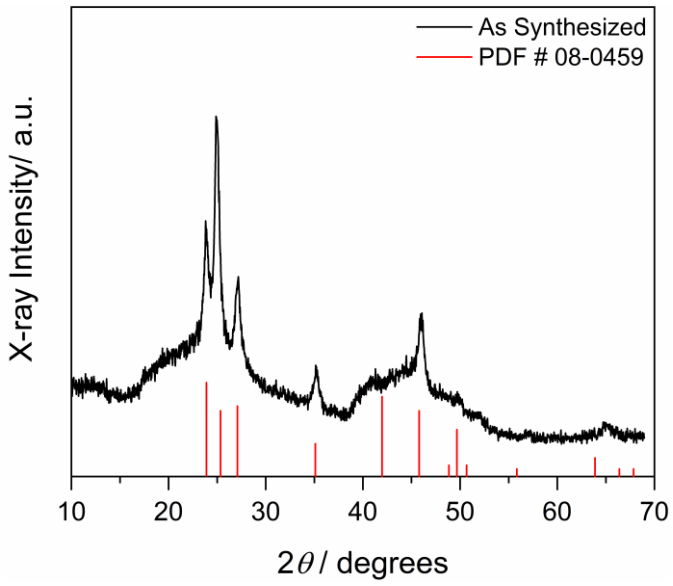

Figure 4.2 : Powder XRD pattern of CdSe nanoparticles (black) and reference pattern (red) corresponding to hexagonal CdSe

For CdSe, its photochemical reactivity towards biomass relevant substrates is relatively unknown. As such, to probe the initial reactivity and stability for this metal chalcogenide, a simpler reaction was tested. Since CdSe is known to drive thiol oxidation photochemically, 2-mercaptoethanol will serve as a suitable model substrate for monitoring particle stability.[16-17] The production of the 2-hydroxyethyl disulfide oxidation product was monitored through kinetics experiments in aqueous and non-aqueous media (Scheme 4.2). Figure 4.3 details the fast kinetics

Scheme 4.2 : The balanced chemical equation for the photocatalytic oxidation of 2-mercaptoethanol on CdSe nanoparticles in air using visible light.

for thiol oxidation with near complete conversion after 120 minutes in alkaline media and 10 minutes in organic media. The identity of the disulfide product formation was confirmed with NMR spectroscopy (Figure C.3). However, as expected, accompanying the fast kinetics is a rapid material degradation event. Of initial note, in the reaction with acetonitrile as the solvent, the material visibly changed with increasing irradiation time. Present in Figure C.4 is a color image of the catalyst powder at each reaction time point from 0 minutes of irradiation to 90 minutes of irradiation. An amorphous dark red material is produced after 90 minutes of photolysis. Based on this color and the expected degradation route, it is likely that the material produced is cadmium oxide. By inductively coupled plasma mass spectrometry (ICP-MS) the leaching of dissolved selenium was detected. A 302.1 (±17.6) ppm concentration was detected in the reaction solution after the catalytic process. The leaching does not follow an increasing trend in the acetonitrile

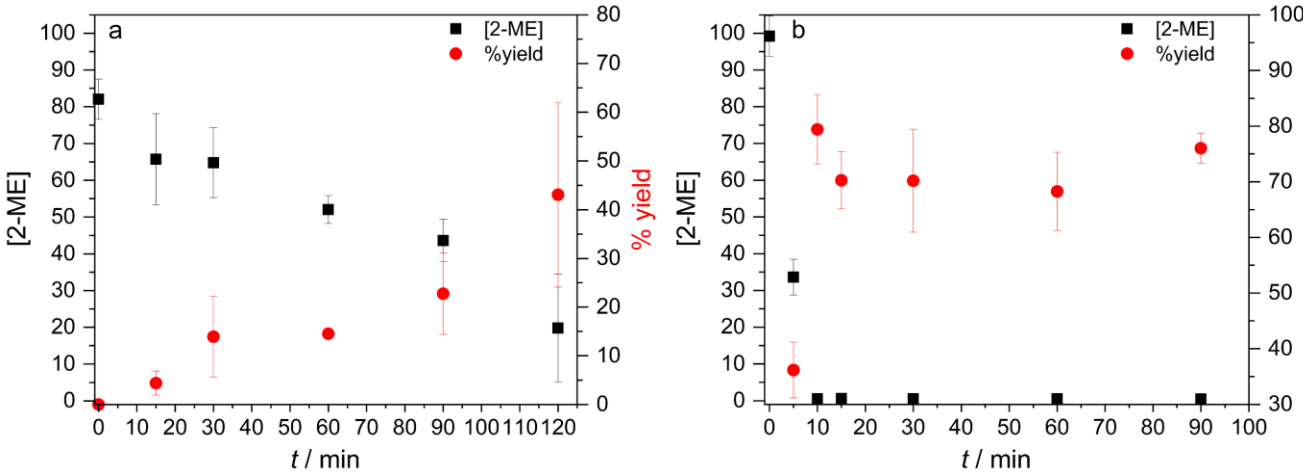

Figure 4.3 : 2-mercaptoethanol consumption (black squares) and yield of 2-hydroxyethyldisulfide (red circles) on CdSe nanoparticles using 460 nm blue LEDs in (a) alkaline water and (b) acetonitrile.

solvent, likely due to the material composition changing where selenium may be leaching and adsorbing back into the material as the degradation event occurs. No cadmium is detected in solution by ICP-MS. In the alkaline photolysis environment both cadmium and selenium are detected by ICP-MS as the dispersed catalyst powder dissolves into solution. Table 4.1 notes the full leaching detected at each timepoint measured for both the aqueous and non-aqueous photocatalytic reactions.

Time (min)	Cd (ppm)_Water	Se (ppm)_Water	Se (ppm)_Acetonitrile
0	0.5±0.3	9.9±10.7	7.0±0.8
5	—	—	55.6±6.6
10	—	—	302.1±17.6
15	2.7±0.3	8.6±3.6	360.4±29.0
30	1.6±0.9	6.8±4.3	261.0±25.7
60	2.4±0.4	6.3±3.8	234.3±13.2
90	2.7±0.8	7.5±4.8	207.1±48.9
120	5.8±1.3	9.4±2.8	—

Table 4.1 : Concentrations of cadmium and selenium in ppm detected by ICP-MS after photo-oxidation of 2-mercaptoethanol in water and acetonitrile.

4.3.2 Synthesis of CdSe@TiO_2 Nanoparticles and Photochemical Characterization

Seeking to improve upon this stability, a core@shell structure was explored. Following known protocols, a titanium dioxide (TiO_2) shell was formed on the surface of the CdSe nanoparticles according to the procedure described above. Through an exchange of the amine capping ligand on the CdSe surface for a titanium hydroxide species, the TiO_2 shell was formed after microwave heating the particles in ethanol solvent. Each conversion stage was monitored by pXRD (Figure 4.4a) and FTIR spectroscopy (Figure 4.4b) to determine the success of the exchange and subsequent microwave conversion. The FTIR data confirms the ligand exchange process showing key N-H stretches (3130-3150 cm^{-1}) and C-H stretches (2850-2920 cm^{-1}) expected for the amine ligand along with the introduction of a broad O-H feature at 3215 cm^{-1} after the exchange. The ligand, however, remains in small amounts after the conversion to the oxide, likely due to the strong binding nature of amine surfactants. Incorporation of the titanium was confirmed with elemental analysis through EDXRF spectroscopy where the elemental Cd:Se:Ti ratios are 1.0:0.8:2.1.

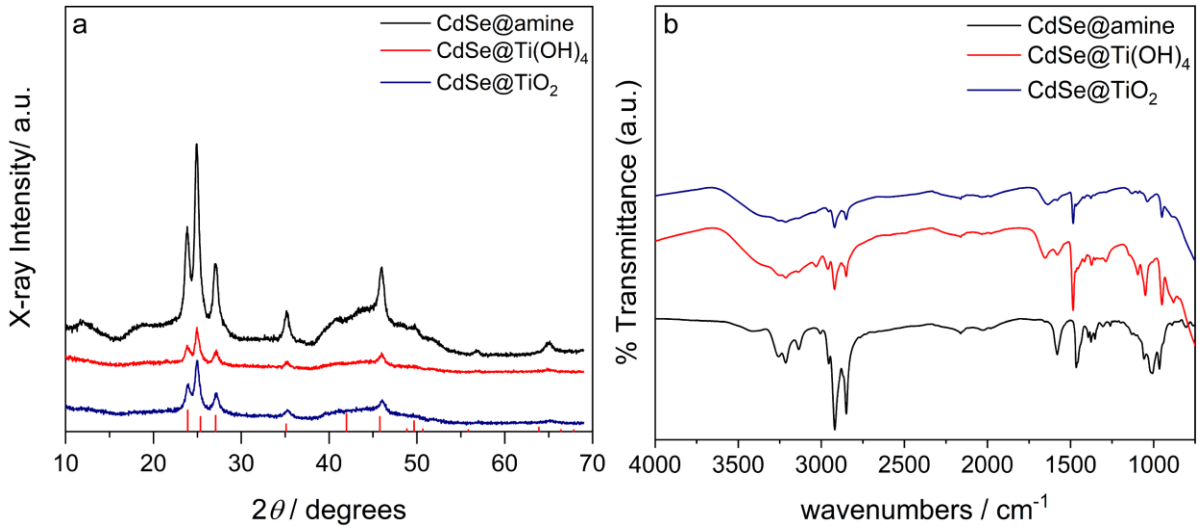

Figure 4.4 : (a) Powder X-ray diffractogram and (b) FTIR of amine coated CdSe (black) titanium hydroxide exchanged CdSe (red) and titanium dioxide coated CdSe (blue).

Similar thiol oxidation experiments were performed on the oxide coated CdSe to determine the effectiveness of the shell as it was synthesized. The kinetic process was still feasible after the introduction of the TiO_2 shell retaining the fast conversions (Figure C.5). The stability, though, was not significantly improved as the respective elements were detected by ICP-MS having leached during the catalytic process (Table 4.2). While the photoreaction is not hindered by the oxide material adhered to the CdSe surface, the coverage may not be as ideal. Synthetic redesigns need to be considered to ensure complete protecting coverage across the whole particle surface.

Solvent	Time (min)	Cd (ppm)	Se (ppm)	Ti (ppm)
Water	0	2.9	13.9	4.4
	15	1.4	10.5	2.1
	30	5.4	15.2	6.3
	60	5.0	18.1	5.0
	90	13.9	30.2	15.7
	120	18.1	33.7	18.5
Acetonitrile	0	0.7	17.5	0.0
	5	0.4	58.3	0.0
	10	0.4	76.8	0.0
	15	0.3	259.5	0.0
	30	0.2	338.8	0.0

Table 4.2 : Concentrations of cadmium, selenium, and titanium in ppm detected by ICP-MS after photo-oxidation of 2-mercaptoethanol in water and acetonitrile on CdSe@TiO_2 .

4.3.3 Redesigned Synthesis of Metal Oxide Coated CdSe Quantum Belts for Improved Photo-stability

To properly examine and reassess the synthetic design, aid was sought on how to best address this catalyst instability. Surface modification of chalcogenide materials has been well studied by the Professor Willaim Buhro from Washington University in St. Louis. Their expertise in ligand exchanges on CdSe quantum dots and nanoclusters has lent itself to addressing the growing photochemical instability of these materials. As such, their synthetic aid was utilized to

determine the optimal route for improved stability. Starting with octylamine coated CdSe quantum belts previously synthesized, ligand exchange with titanium ethoxide and its subsequent oxidation into TiO_2 was observed by the Buhro and coworkers. FTIR spectroscopy at each stage of the exchange confirmed the removal of the amine ligand and displacement with the titanium alkoxide ligand. Since XRD of this oxide coated species could not be clearly ascertained, Raman spectroscopy was used to confirm the success of this step as the resulting peaks match the known spectrum for anatase TiO_2 particles (Figure 4.5).[18]

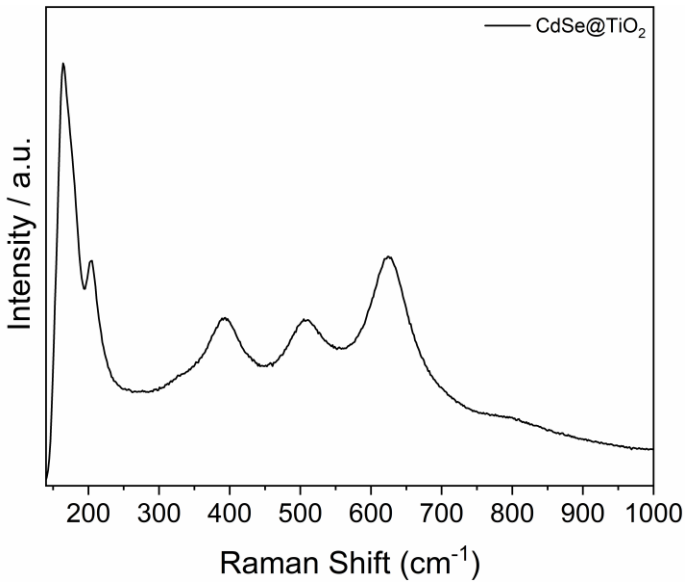

Figure 4.5 : Raman spectra of TiO_2 coated CdSe quantum belts.

In addition, the surface electronic structure and incorporation of TiO_2 was further confirmed with X-ray photoelectron spectroscopy. Deconvolution of the spectra allows for an assignment of each elemental state. As it is synthesized, the amine coated CdSe contains Cd^{2+} assigned to 404.8 eV in the Cd(3d) spectrum along with Se^{2-} and Se(0) assigned to 54.3 eV and 56.2 eV respectively in the Se(3d) spectrum (Figure C.6). After the growth of the TiO_2 layer, the surface and interface structure begin to change (Figure C.7). The Ti(2p) and O(1s) orbitals, respectively, confirm the formation of TiO_2 on the chalcogenide surface. Ti^{4+} presents with the peak at 458.3 eV. Lattice oxygen along with surface hydroxide are present as expected for oxide

materials with features at 529.8 eV and 531.1 eV. Cadmium remains as it presented in the amine coated sample, however selenium shows a minimal amount of surface oxidation explained by a new XPS feature arising at 61.8 eV. This is oxidation is expected to accompany the TiO_2 growth on the surface.

Initial assessment of the stability of this coating was confirmed using ICP-MS analysis. Briefly, suspensions of the coated particles were stirred in water for a 24-hour period both illuminated with visible light and in the dark. After this time, the solutions were tested for the presence of trace metals that may have leached. The illuminated suspensions afforded only 2.75 ppm and 0.56 ppm of cadmium and selenium leaching respectively. This accounts for ~0.004% of the starting Cd and Se content. No titanium leaching was detected. The solution stirred in the dark resulted in no observed cadmium or titanium leaching and minimal selenium leaching (~0.002%). Based on this assessment, the substantial binary metal oxide coating prevented any significant photo-corrosion to the particles surface when illuminated in aqueous media.

4.3.4 Photochemical Stability of Redesigned CdSe@TiO_2 following Primary Alcohol Oxidation

In combination with the proposed analysis described above, assessing the photocatalytic activity of these particle on the aerobic oxidation of alcohols will be necessary for confirming the success of the oxide coating surrounding the chalcogenide material. In concert, the work presented in this section will serve to determine if the charge carriers produced from CdSe upon illumination will sufficiently oxidize the model biomass substrate benzyl alcohol and if the TiO_2 oxide shell properly protects the CdSe core during this catalysis. For the photochemical oxidation of benzyl alcohol acetonitrile will serve as the solvent to ensure complete solubility of the substrate and

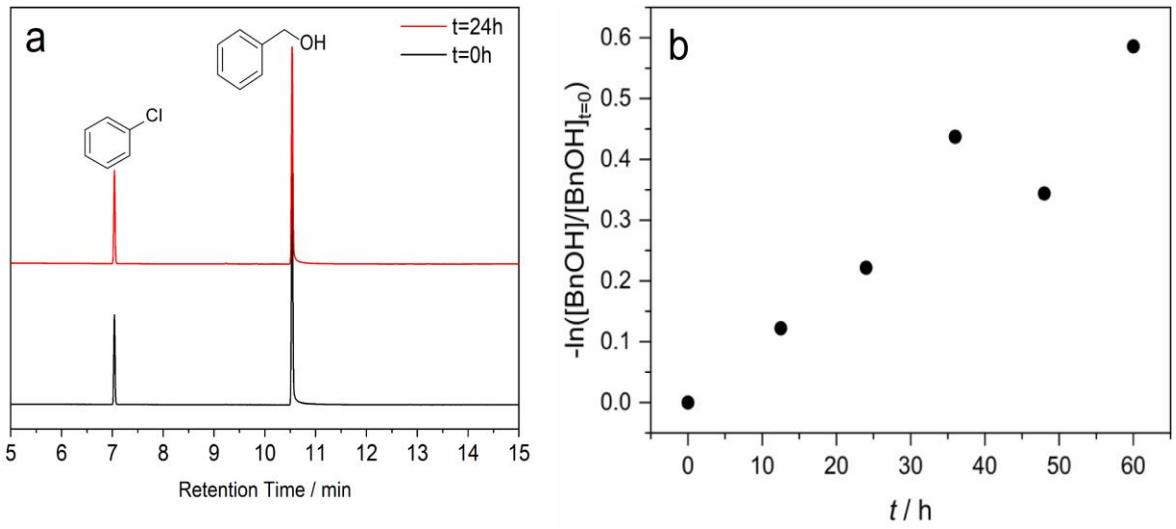

Figure 4.6 : (a) Gas chromatograph for the photochemical oxidation of benzyl alcohol on CdSe@amine (b) first order rate plot for the photochemical oxidation of benzyl alcohol on CdSe@TiO_2.

avoid any unwanted side reactions due to water oxidation. This will allow for the observation of the photodegradation process as a result of the organic oxidation.

Under visible light illumination, the oxidation of benzyl alcohol to benzaldehyde was monitored on the CdSe@TiO_2 nanoparticles. With GC analysis the production of the benzaldehyde product could be observed. A kinetics experiment highlights the first-order kinetics for this process (Figure 4.6b). While this process was achievable for the coated material, the uncoated chalcogenide was not able to produce the same result (Figure 4.6a). No substrate conversion was observed over a 24-hour period of illumination. As such an appropriate comparison could not be made for these materials in this photochemical system. Despite this, the observed leaching of the

Time (min)	Cd (ppm)	Se (ppm)	Ti (ppm)
0	5.6	0.9	0.0
3	4.3	1.5	0.0
6	5.4	2.8	0.0
9	5.2	3.5	0.0
12	7.2	4.6	0.0
24	0.1	2.3	0.0

Table 4.3 : Concentrations of cadmium, selenium, and titanium in ppm detected by ICP-MS after photo-oxidation of benzyl alcohol in acetonitrile on CdSe@TiO_2 .

elements was minimized showing cadmium and selenium during the first 24-hour period, with no titanium detected (Table 4.3).

While the degree of leaching was diminished, the solid phase of the material still proceeded through a degradation pathway. Visually the solid powder went through another color change as depicted in Figure C.8. This observation suggests that the surface composition and structure are being altered. To confirm this XPS was performed to determine the electronic structure after catalysis (Figure 4.7). Notably the cadmium and selenium signals significantly decrease highlighting the loss and alteration of the solid material. The Cd(3d) spectrum retains the Cd^{2+} features present at 405 eV. In the Se(3d) spectrum however, complete oxidation of the remaining solid selenium is observed with an increase in the peak center to 61 eV. Accompanying this, the Ti(2p) and O(1s) spectra as well show newly reduced features at lower binding energies; 457 eV and 528.5 eV respectively. Based on this observation, the oxidation of selenium during catalysis creates new electronic environments for titanium and oxygen bound to selenium at the metal chalcogenide and metal oxide interface. Producing a different material, the TiO_2 coating still allows for the photochemically driven degradation of CdSe. The complete coverage of the oxide shell on the chalcogenide core proves unsuccessful.

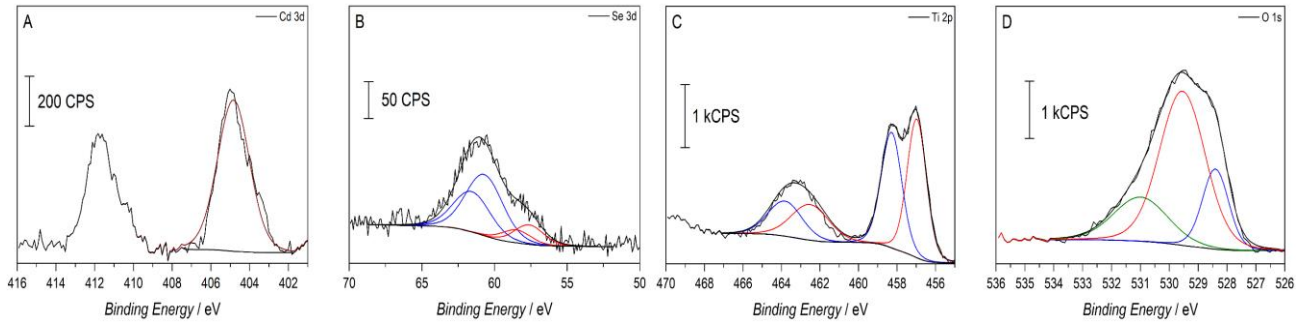

Figure 4.7 : (a) Cd 3d, (b) Se 3d, (c) Ti 2p, and (d) O 1s XPS spectra for CdSe@TiO_2 quantum belts after the photochemical oxidation of benzyl alcohol.

4.4 Conclusion

The utility of cadmium selenide to photochemically drive organic redox reactions is poor in aqueous and non-aqueous media. Despite being an efficient visible light absorbing catalyst, corrosion of the nanoparticle surface during photolysis creates a challenge in poor longevity and high toxicity of the active material. To address this stability issue, the implementation of a metal oxide shell around the photo-active chalcogenide core was explored. The stability was progressively improved for a short time with the leaching of toxic elements diminished when illuminated in the presence of redox active substrates. However, solid changes at the materials surface revealed synthetic challenges to using this solution on the nanoscale. An inability to establish complete coverage of the TiO_2 around the CdSe allowed for the surface corrosion to continue. As this work is further researched, a key hypothesis to explore is how the crystalline identity of the intended oxide shell impacts the degree of coverage. It is possible that efficient ligand exchange and successive coverage will be better suited for an oxide material that matches the crystal class of the core chalcogenide. Accounting for the material composition, the coverage must also be confirmed at each stage in the surface alterations to ensure that the chalcogenide surface is protected and can remain active to drive these useful organic reactions. Transmission electron microscopy (TEM) with elemental mapping will appropriately identify the shell transformation at each stage and ensure even coverage across the collection of particles. In addition, particle size analysis is suggested to account for individual particle structures in the core@shell network and the absence of particle aggregation as the nature of the shell is further altered. These combined techniques will allow for the efficient synthesis of stable oxide coated chalcogenide nanoparticles and provide thorough evaluation of the shell coverage, leading to improved photostability.

4.5 References

1. Furdyna, J. K.; Dong, S.-N.; Lee, S.; Liu, X.; Dobrowolska, M. The Ubiquitous Nature of Chalcogenides in Science and Technology. In *Chalcogenide*; Elsevier, 2020; pp 1–30.

2. Davis, A. P.; Huang, C. P. The Removal of Substituted Phenols by a Photocatalytic Oxidation Process with Cadmium Sulfide. *Water Res.* **1990**, *24* (5), 543–550.

3. Kuehnel, M. F.; Wakerley, D. W.; Orchard, K. L.; Reisner, E. Photocatalytic Formic Acid Conversion on CdS Nanocrystals with Controllable Selectivity for H_2 or CO. *Angew. Chemie Int. Ed.* **2015**, *54* (33), 9627–9631.

4. Fagnoni, M.; Dondi, D.; Ravelli, D.; Albini, A. Photocatalysis for the Formation of the C−C Bond. *Chem. Rev.* **2007**, *107* (6), 2725–2756.

5. Han, G.; Jin, Y.-H.; Burgess, R. A.; Dickenson, N. E.; Cao, X.-M.; Sun, Y. Visible-Light-Driven Valorization of Biomass Intermediates Integrated with H_2 Production Catalyzed by Ultrathin Ni/CdS Nanosheets. *J. Am. Chem. Soc.* **2017**, *139* (44), 15584–15587.

6. Meissner, D.; Memming, R.; Kastening, B.; Bahnemann, D. Fundamental Problems of Water Splitting at Cadmium Sulfide. *Chem. Phys. Lett.* **1986**, *127* (5), 419–423.

7. Xi, L.; Lek, J. Y.; Liang, Y. N.; Boothroyd, C.; Zhou, W.; Yan, Q.; Hu, X.; Chiang, F. B. Y.; Lam, Y. M. Stability Studies of CdSe Nanocrystals in an Aqueous Environment. *Nanotechnology* **2011**, *22* (27), 275706.

8. DiMeglio, J. L.; Bartlett, B. M. Interplay of Corrosion and Photocatalysis During Nonaqueous Benzylamine Oxidation on Cadmium Sulfide. *Chem. Mater.* **2017**, *29* (17), 7579–7586.

9. Yang, Z.; Guo, L.; Zu, B.; Guo, Y.; Xu, T.; Dou, X. CdS/ZnO Core/Shell Nanowire-Built Films for Enhanced Photodetecting and Optoelectronic Gas-Sensing Applications. *Adv. Opt. Mater.* **2014**, *2* (8), 738–745.

10. Zhou, Y.; Wen, T.; Chang, B.; Yang, B.; Wang, Y. Core–Shell $Cd_{0.2}Zn_{0.8}S$@BiOX (X = Cl, Br and I) Microspheres: A Family of Hetero-Structured Catalysts with Adjustable Bandgaps, Enhanced Stability and Photocatalytic Performance under Visible Light Irradiation. *Dalt. Trans.* **2016**, *45* (35), 13709–13716.

11. Zhang, P.; Liu, Y.; Tian, B.; Luo, Y.; Zhang, J. Synthesis of Core-Shell Structured CdS@CeO_2 and CdS@TiO_2 Composites and Comparison of Their Photocatalytic Activities for the Selective Oxidation of Benzyl Alcohol to Benzaldehyde. *Catal. Today* **2017**, *281*, 181–188.

12. Ning, X.; Zhen, W.; Wu, Y.; Lu, G. Inhibition of CdS Photocorrosion by Al_2O_3 Shell for Highly Stable Photocatalytic Overall Water Splitting under Visible Light Irradiation. *Appl. Catal. B Environ.* **2018**, *226*, 373–383.

13. Zhou, Y.; Wang, F.; Buhro, W. E. Large Exciton Energy Shifts by Reversible Surface Exchange in 2D II–VI Nanocrystals. *J. Am. Chem. Soc.* **2015**, *137* (48), 15198–15208.

14. Yao, Y.; Zhou, Y.; Sanderson, W. M.; Loomis, R. A.; Buhro, W. E. Metal-Halide-Ligated Cadmium Selenide Quantum Belts by Facile Surface Exchange. *Chem. Mater.* **2018**, *30* (8), 2848–2857.

15. Yao, Y.; DeKoster, G. T.; Buhro, W. E. Interchange of L-, Z-, and Bound-Ion-Pair X-Type Ligation on Cadmium Selenide Quantum Belts. *Chem. Mater.* **2019**, *31* (11), 4299–4312.

16. Thackeray, J. W.; Natan, M. J.; Ng, P.; Wrighton, M. S. Interaction of Diethyldithiocarbamate with N-Type Cadmium Sulfide and Cadmium Selenide: Efficient Photoelectrochemical Oxidation to the Disulfide and Flat-Band Potential of the Semiconductor as a Function of Adsorbate Concentration. *J. Am. Chem. Soc.* **1986**, *108* (13), 3570–3577.

17. Dong, F.; Han, H.; Liang, J.; Lu, D. Study on the Interaction between 2-Mercaptoethanol, Dimercaprol and CdSe Quantum Dots. *Luminescence* **2008**, *23* (5), 321–326.

18. Chu, L.; Qin, Z.; Yang, J.; Li, X. Anatase TiO_2 Nanoparticles with Exposed {001} Facets for Efficient Dye-Sensitized Solar Cells. *Sci. Rep.* **2015**, *5* (1), 12143.

Chapter 5

Conclusions and Future Directions

5.1 Summary of Presented Work

The work completed in this thesis set to develop synthetic routes for phase pure, metal oxide semiconductor nanomaterials using solvent-assisted low temperature methods through controlled microwave heating. This work focuses on those materials known for performing useful catalytic transformations on organic substrates and studies how their syntheses can be adapted to offer improved stability to other known useful metal chalcogenide semiconductors. In Chapter 2, nanocrystalline WO_3 was formed faster and at lower temperatures than conventional synthesis methods. The photochemical activity of these particles was monitored with the selective oxidation of benzylamine, benzyl alcohol, and 5-hydroxymethylfurfural to the corresponding products. Modification to the particle size through continued microwave heating and testing with commercial micron-sized particles revealed changes to the reaction rates expected based on literature assessment. An increased specific surface area and a decreased distance for charge carriers to diffuse was key in affording the improved catalysis. Drawbacks presented, however, limit the breadth of reactions possible for continued use of this catalyst.

To further expand upon this work Chapter 3 explores ternary metal ferrite materials as a class of photochemically active oxide materials with more ideal thermodynamic band potentials. Adapting similar microwave principles to that studied in Chapter 2, spinel phase $MgFe_2O_4$ could be synthesized with the aid of high temperature annealing. Though annealing techniques were

necessary to induce crystallization of this material, the nano-size of the particles and high surface area could be retained. Through the annealing it was discovered that the physical and electronic properties of the material were altered with increasing temperature. In benchmarking activity to the photochemical degradation of methylene blue dye, kinetics experiments led to the conclusion that the catalysis was more heavily influenced by maximizing particle surface area and maintaining reactive surface hydroxyl groups, contrary to the site ordering characteristic changes. The work in this chapter in concert with the work in Chapter 2 drives home the importance of minimizing the overall size of the oxide particles and creating a large surface area for the redox reactions to progress at fast rates.

Continued exploration of the synthetic scope of microwave chemistry led to utilizing the knowledge gained in the synthesis of oxide materials for the improvement of chalcogenide catalytic systems. Chapter 4 presents the photostability of CdSe in the space of aqueous and non-aqueous organic oxidaiton of 2-mercaptoethanol and benzyl alcohol, impeded by photocorrosion. Microwave techniques were explored for the implementation of an oxide shell to provide a stabilizing covering of the chalcogenide surface. Synthetic challenges resulted in no improvements to the photostability of the CdSe nanoparticles. To better develop this science, a collaboration with Professor William Buhro's lab at Washington University in St. Louis was undertaken. Initial assessment of the photo-stability continued to show stark catalyst degradation of the control particles upon which, with the addition of the oxide shell leaching of toxic elements was suppressed. Still there is room to grow in this work as complete coverage of the nanoparticles and quantum belts could not be fully achieved.

Overall, advancements were made in the direction of improving the synthesis of photoactive semiconductor nanomaterials. Further growth in this field will rely on optimized material choices

for targeting specific reactions. The conclusions from this thesis outline only a few factors one must consider for achieving the highest outcome of catalytic success. However, the techniques utilized above provide ample foundation for the study of more focused features belonging to these solid-state materials. The remainder of this chapter presents two main considerations in this regard as suggested routes to begin the next steps of this work.

5.2 Composite Materials for Advanced Photocatalysis

This thesis highlights efficient solution-based routes for the synthesis of binary and ternary metal oxide and metal chalcogenide materials. However, with limitations inherent in their electronic structures future goals in this field need to center on routes of improvement. Even on the nanoscale and when the thermodynamics are favorable, rapid charge recombination is limiting rates for targeted 1º alcohol oxidation reactions. As presented in the introduction, improvement efforts can be sought with complex composite materials. These efforts offer aid to the charge separation and transfer properties that cause low reactivity for many bulk catalysts.

Z-scheme composite materials contain the catalyst of interest and are typically bound to polymeric, carbon-based materials like reduced graphene oxide (rGO).[1,2] or graphitic carbon nitride (g-C_3N_4).[3,4] These materials are conductive and have large surface areas to allow for easy anchoring of semiconductors. Acting as an electron sink, they present an alternative mechanism for limiting electron-hole recombination. Single and multi-step approaches have already been implemented and shown success for improving photocatalytic reactions rates. As well, adapting this synthesis for microwave synthesis has been successful for the binary oxides SnO_2 and Fe_3O_4 grown directly on to rGO.[5] In this work reduction of graphene oxide is achieved by the benzyl alcohol solvent. Simultaneously, the rGO surface is activated by absorbed microwave irradiation to facilitate direct growth of the binary oxides and adsorption to the surface. As common with non-

aqueous microwave assisted approaches the reaction is successful in short reaction times and with a retention of the particle size. One can expect similar activation and single-pot success with other semiconductor materials. As such, this endeavor reinvigorates the call for new ternary materials with the potential for success in the photochemical oxidation of organic substrates.

Beyond carbon-based materials, composites can also be designed with other metal or metal oxide semiconductors through Z-scheme binding or a heterjunction. Acting under a similar principle the anchoring of two photo(electrochemically) active materials can provide an effective means to prevent photo charge carriers from recombining.[6-8] In addition, with these materials' appropriate optimization of electronic properties can give new access to previously unattainable reactions. For materials like WO_3 that are unable to drive the reduction of oxygen or protons, this electronic design can creatively alter the functionality of a catalyst for the better. For materials like the ternary metal ferrites, charge recombination can be greatly diminished to improve catalysis. This case was preliminarily explored on the microwave synthesized $MgFe_2O_4$ nanoparticles presented in Chapter 3. Modified for microwave heating, platinum (Pt) nanoparticles are loaded

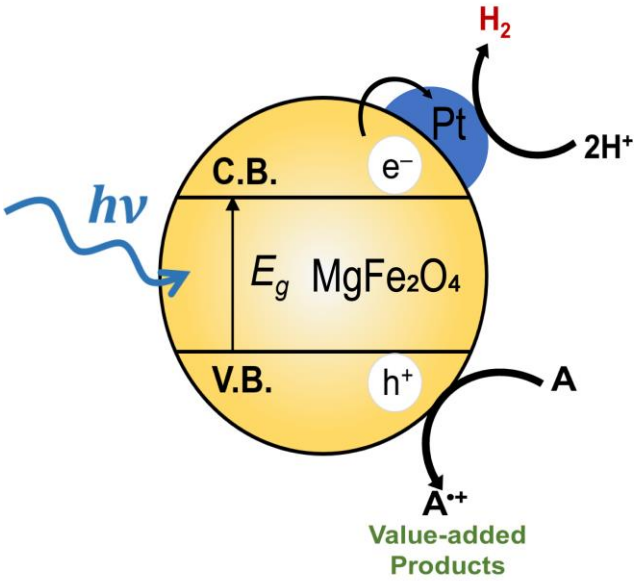

Figure 5.1: Diagram detailing the photocatalytic process for metal oxide semiconductor particles interfaced with platinum particles for increased charge separation and access to the hydrogen evolution reaction.

onto the metal oxide to facilitate the charge separation and can further aid in the process of proton reduction as detailed in Figure 5.1.

In brief, Pt nanoparticles were first prepared by the reduction of $H_2PtCl_6 \cdot 6H_2O$ in an ethylene glycol/water solvent mixture of 1:1. This solution was heated under microwave irradiation at 130°C for 1 hour and then stirred for 2 hours at room temperature before being neutralized to pH 7. Pt loading onto $MgFe_2O_4$ nanoparticles was achieved under light heating (Figure 5.2a). The photochemical activity of the new composite was tested for the oxidation of methanol to formaldehyde under visible light illumination. Increased product formation was observed for the composite material when compared to the performance of the native oxide (Figure 5.2b).

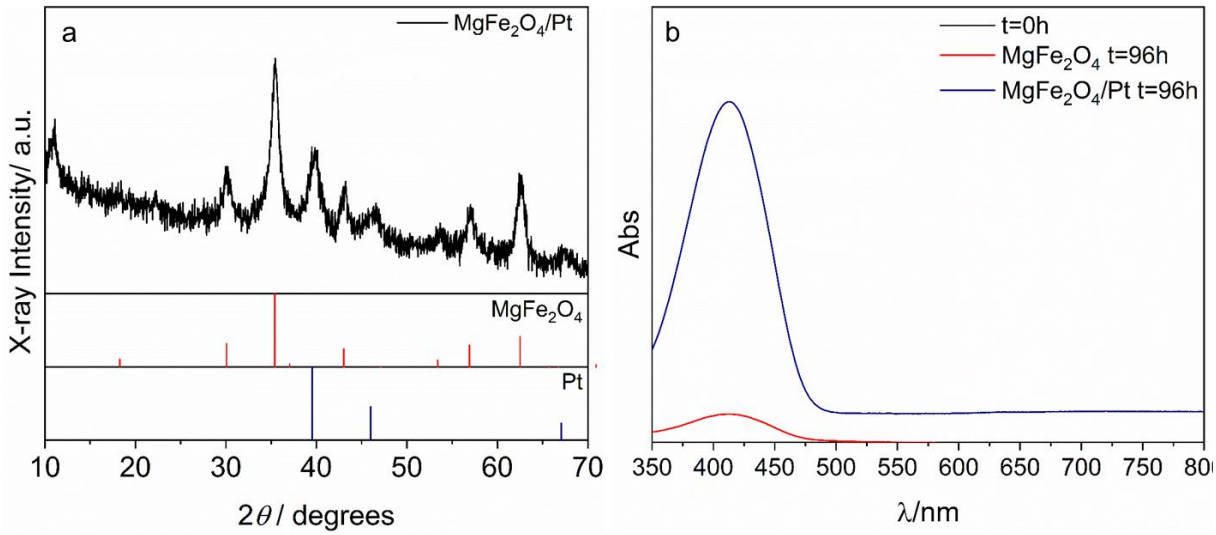

Figure 5.2: (a) Powder XRD of platinized $MgFe_2O_4$ and (b) UV-vis spectra of formaldehyde production measured through a colorimetric test at λ = 412 nm.

5.3 Microwave Assisted Synthesis of Metal Oxide Thin Films

Driving redox reactions under purely photochemical means is the most scalable and robust route. However, the limitations expressed in this thesis raise necessary questions on how to explore the combination of new catalytic materials in new reaction systems. To address problems due to slow reaction kinetics and poor thermodynamics for either half reaction, it can be beneficial to

study interesting materials through photoelectrochemical means. Adhered to a conductive substrate (i.e. fluorinated or indium tin oxide glass) applied external potential can greatly influence the observed reaction. The synthesis and anchoring of these materials onto the conductive substrates presents new avenues for materials exploration.

Adoption of microwave synthesis techniques for the preparation of simple and complex metal oxide photocatalysts has proven very fruitful.[9] The use of organic solvents to facilitate the synthetic inorganic components offers a robust and adaptable route for further materials exploration. These materials synthesized in short reaction times and controlled environments continue to reveal interesting chemistry for photo driven redox processes. Having explored the improved synthesis of colloidal metal oxide nanoparticles, expansion of this chemistry into the synthesis of metal oxide thin films is increasingly imperative.

Looking to the literature reveals the multi-step electrosynthesis and thermolysis of multi-metal oxides to guide a potential initial approach.[10,11] Often though, the first step of electrosynthesis requires complex reaction solutions and presents challenges in reproducibility. In contrast to these routes, the electrosynthesis step can be replaced with microwave assisted deposition of semiconductor materials and templates.(Figure 5.3) The uniform heating afforded by microwave irradiation will provide a controlled and robust synthesis environment for the growth of solid materials directly on to the conductive fluorinated-tin-oxide (FTO) substrate.[12] These thin film

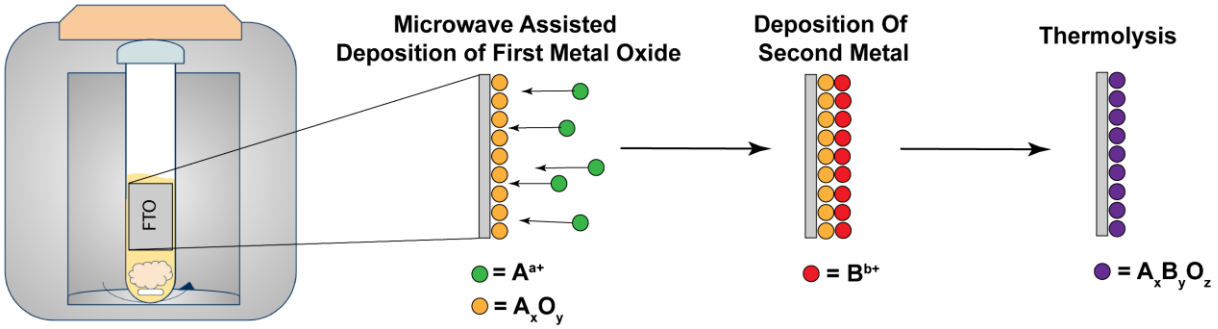

Figure 5.3: Diagram of the proposed multi-step synthesis of ternary metal oxide photoelectrodes using microwave heating.

templates will serve as a substantial backing for the formation of ternary oxide materials with varied compositions.

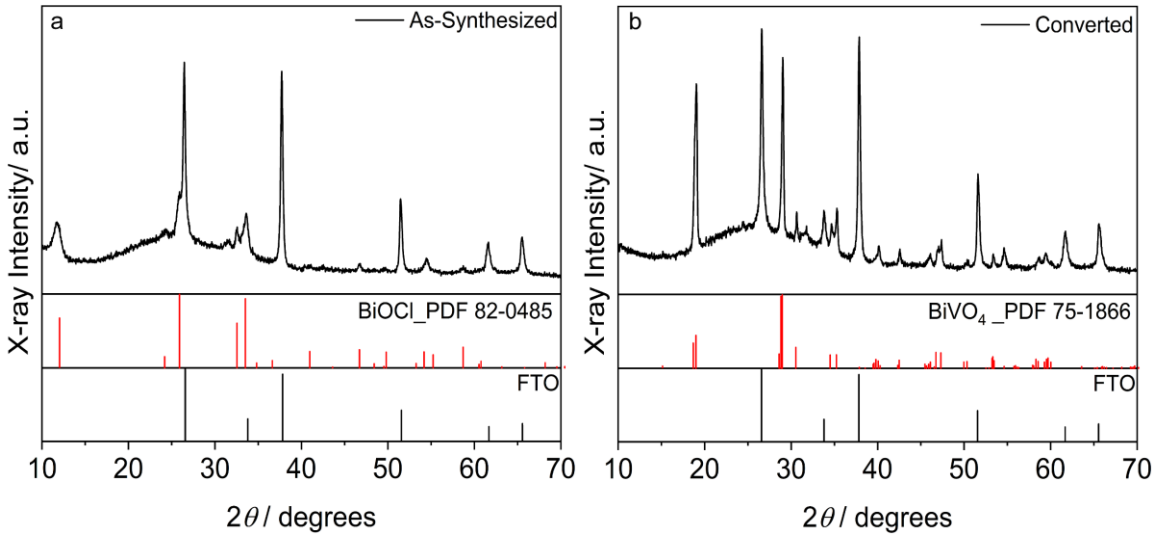

Figure 5.4: Powder XRD of (a) BiOCl grown directly onto FTO through microwave synthesis and (b) $BiVO_4$ formed after vanadium drop-casting and thermolysis. Corresponding references provided for FTO (black lines) and the respective semiconductors (red lines).

Initial success in this proposal has been explored and achieved. Bismuth oxychloride (BiOCl) templates can be directly grown onto FTO through microwave irradiation. In ethylene glycol solvent, soluble bismuth nitrate and potassium chloride precursors are all that is necessary to grow crystalline BiOCl nanoparticles in a short reaction time of 30 minutes at a temperature of 180°C. With this film template the ternary monoclinic phase of bismuth vanadate ($BiVO_4$) can be formed following adapted protocols. Powder X-ray diffraction confirms the identity of each material at their respective synthetic steps (Figure 5.4). Corresponding scanning electron microscopy (SEM) images for each stage in the oxide film synthesis details nano-fibrous clusters that upon conversion transform into a thin oxide network (Figure 5.5). This proposed direction offers a large toolbox of ternary and composite materials that can be accessed through microwave chemistry for photoelectrochemical analysis.

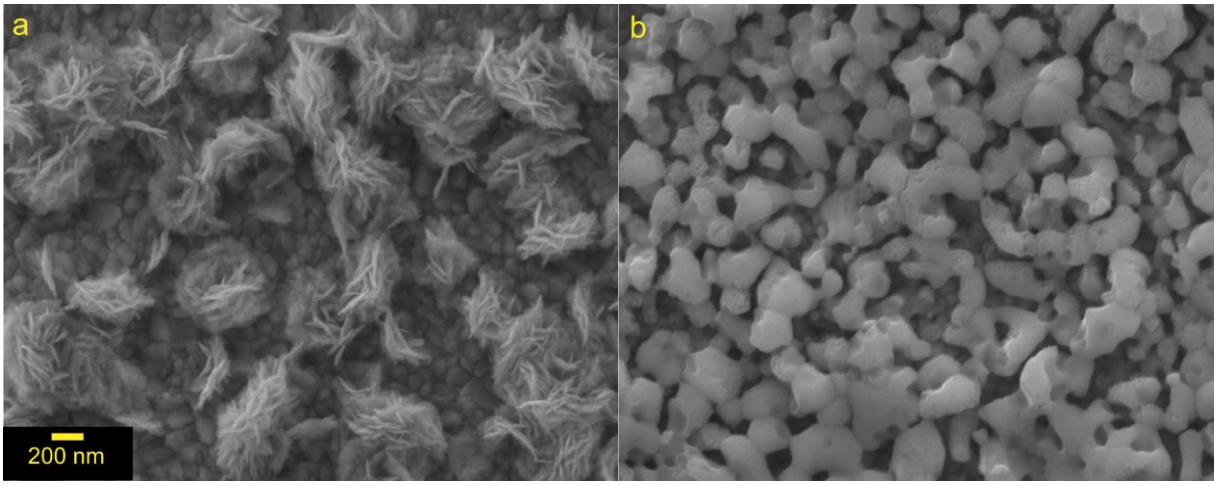

Figure 5.5: SEM of (a) BiOCl grown directly onto FTO through microwave synthesis and (b) $BiVO_4$ formed after vanadium drop-casting and thermolysis. Corresponding scale bar provided for both images.

5.4 References

1. Li, P.; Zhou, Y.; Li, H.; Xu, Q.; Meng, X.; Wang, X.; Xiao, M.; Zou, Z. All-Solid-State Z-Scheme System Arrays of $Fe_2V_4O_{13}$/RGO/CdS for Visible Light-Driving Photocatalytic CO_2 Reduction into Renewable Hydrocarbon Fuel. *Chem. Commun.* **2015**, *51* (4), 800–803.

2. Sadiq, M. M. J.; Shenoy, U. S.; Bhat, D. K. Novel RGO–$ZnWO_4$–Fe_3O_4 Nanocomposite as High Performance Visible Light Photocatalyst. *RSC Adv.* **2016**, *6* (66), 61821–61829.

3. He, Y.; Wang, Y.; Zhang, L.; Teng, B.; Fan, M. High-efficiency conversion of CO_2 to fuel over ZnO/g-C_3N_4 photocatalyst. *Appl. Catal., B* **2015**, 168-169,1−8.

4. He, Y. M.; Zhang, L. H.; Fan, M. H.; Wang, X. X.; Walbridge, M. L.; Nong, Q. Y.; Wu, Y.; Zhao, L. H. Z-scheme SnO_{2-x}/g-C_3N_4 composite as an efficient photocatalyst for dyes degradation and photocatalytic CO_2 reduction. *Sol. Energy Mater. Sol. Cells* **2015**, *137*, 175−184.

5. Baek, S.; Yu, S.-H.; Park, S.-K.; Pucci, A.; Marichy, C.; Lee, D.-C.; Sung, Y.-E.; Piao, Y.; Pinna, N. A One-Pot Microwave-Assisted Non-Aqueous Sol–Gel Approach to Metal Oxide/Graphene Nanocomposites for Li-Ion Batteries. *RSC Adv.* **2011**, *1* (9), 1687.

6. Jayaraman, S.; Jaramillo, T. F.; Baeck, S.-H.; McFarland, E. W. Synthesis and Characterization of Pt−WO_3 as Methanol Oxidation Catalysts for Fuel Cells. *J. Phys. Chem. B* **2005**, *109* (48), 22958–22966.

7. Bellardita, M.; García-López, E. I.; Marcì, G.; Palmisano, L. Photocatalytic Formation of H2 and Value-Added Chemicals in Aqueous Glucose (Pt)-TiO_2 Suspension. *Int. J. Hydrogen Energy* **2016**, *41* (14), 5934–5947.

8. Wang, F.; Gu, Y.; Yang, Z.; Xie, Y.; Zhang, J.; Shang, X.; Zhao, H.; Zhang, Z.; Wang, X. The Effect of Halogen on BiOX (X = Cl, Br, I)/Bi_2WO_6 Heterojunction for Visible-Light-Driven Photocatalytic Benzyl Alcohol Selective Oxidation. *Appl. Catal. A Gen.* **2018**, *567*, 65–72.

9. Bilecka, I.; Niederberger, M. Microwave Chemistry for Inorganic Nanomaterials Synthesis. *Nanoscale* **2010**, *2* (8), 1358.

10. Vali, A.; Jee, H.; Myung, N.; Rajeshwar, K. Combining Electrosynthesis with Thermolysis: A Safe/Scalable Route to Multinary Oxide Semiconductor Films. *ChemElectroChem* **2021**, *8* (7), 1251–1258.

11. Lee, D. K.; Choi, K.-S. Enhancing Long-Term Photostability of $BiVO_4$ Photoanodes for Solar Water Splitting by Tuning Electrolyte Composition. *Nat. Energy* **2018**, *3* (1), 53–60.

12. Rana, A. ul H. S.; Kang, M.; Kim, H.-S. Microwave-Assisted Facile and Ultrafast Growth of ZnO Nanostructures and Proposition of Alternative Microwave-Assisted Methods to Address Growth Stoppage. *Sci. Rep.* **2016**, *6* (1), 24870.

Appendix A

Supporting Information for Chapter 2

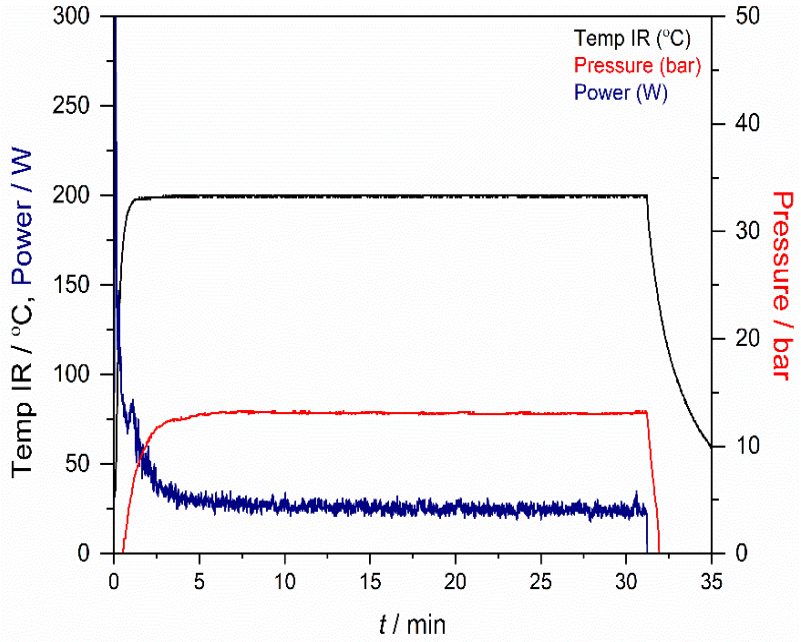

Figure A.1. Temperature, Pressure, and Power readings observed during microwave heating at 200°C for 30 minutes.

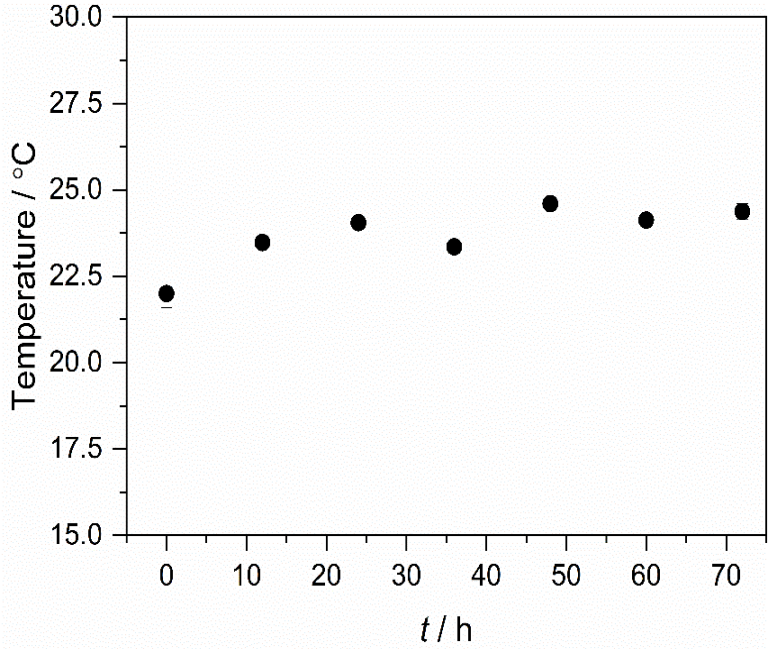

Figure A.2. Heating profile for a bare acetonitrile solution when illuminated by the blue LED's.

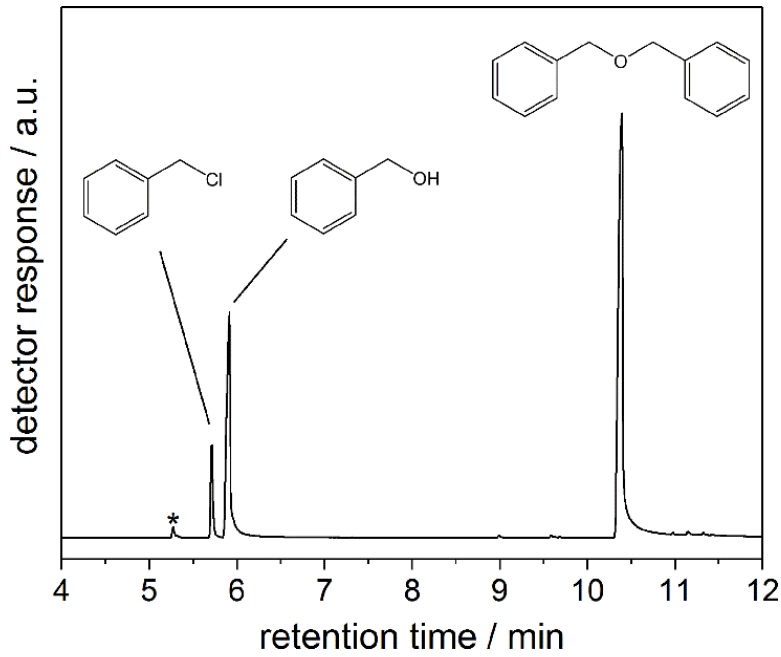

Figure A.3. Gas chromatogram for the MW–30 reaction solution. The four peaks correspond to benzaldehyde (5.27 min), benzyl chloride (5.72 min), benzyl alcohol (5.95 min), and dibenzyl ether (10.43 min).

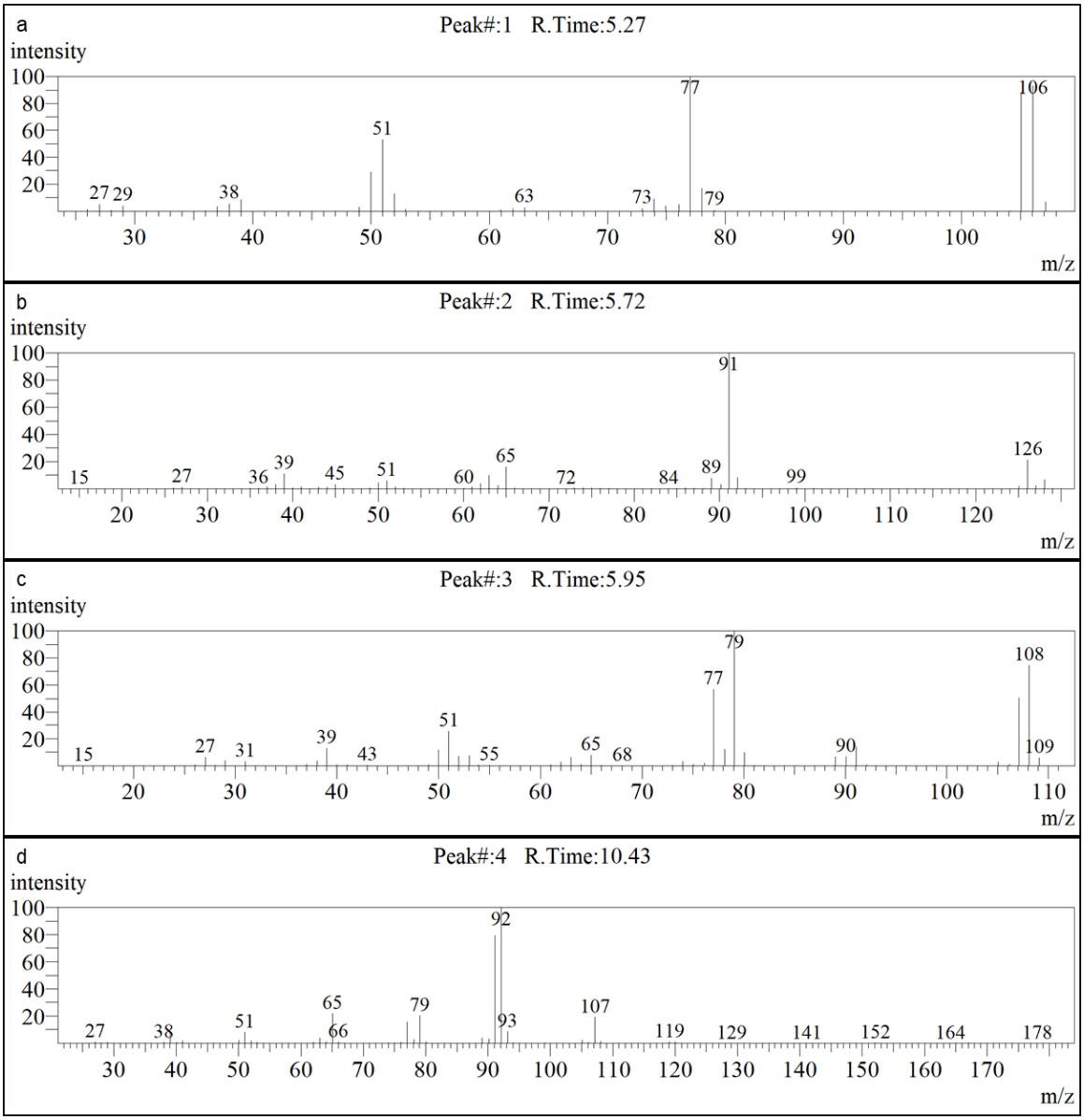

Figure A.4. Corresponding mass spectra for the organic by-products observed from GC-MS analysis on the post-synthesis reaction solution. In order, the spectra match to (a) benzaldehyde, C_7H_6O (m/z^+ = 106 Da); (b) benzyl chloride, C_7H_7Cl (m/z^+ = 126 Da); (c) benzyl alcohol, C_7H_8O (m/z^+ = 108 Da); and (d) dibenzyl ether, $C_7H_8^+$ fragment (m/z^+ = 92 Da).

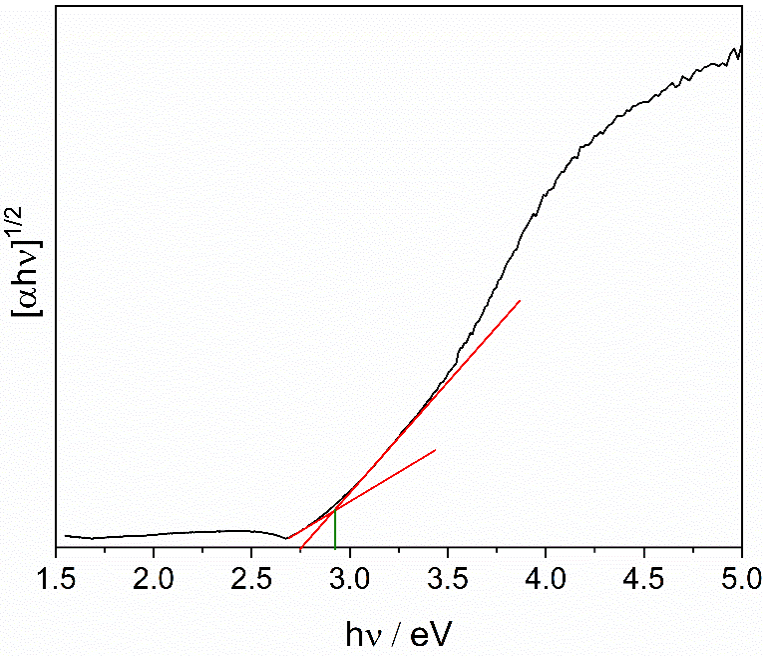

Figure A.5. UV-Vis Diffuse Reflectance spectra for WO_3 nanoplatelets.

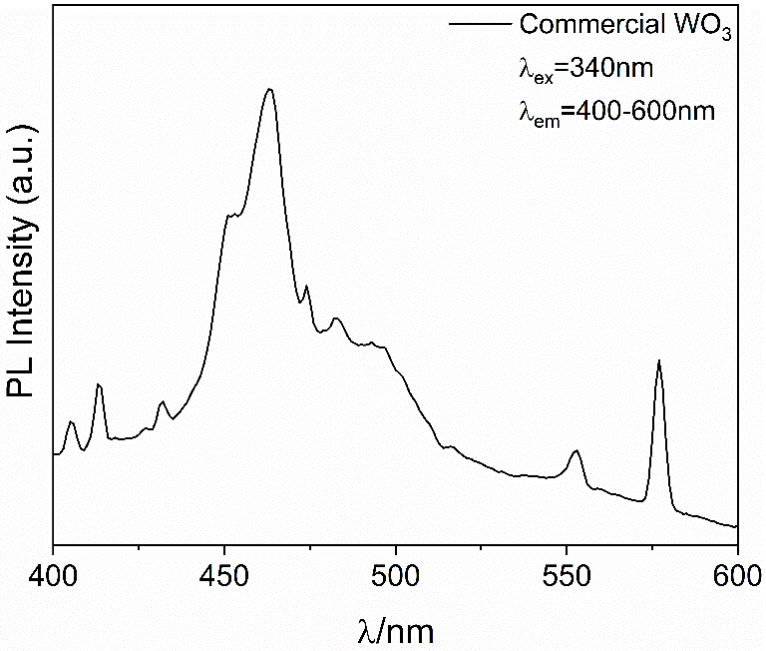

Figure A.6. Room temperature photoluminescence spectra for commercially available WO_3 particles. Spectra collect with an excitation wavelength of 340 nm.

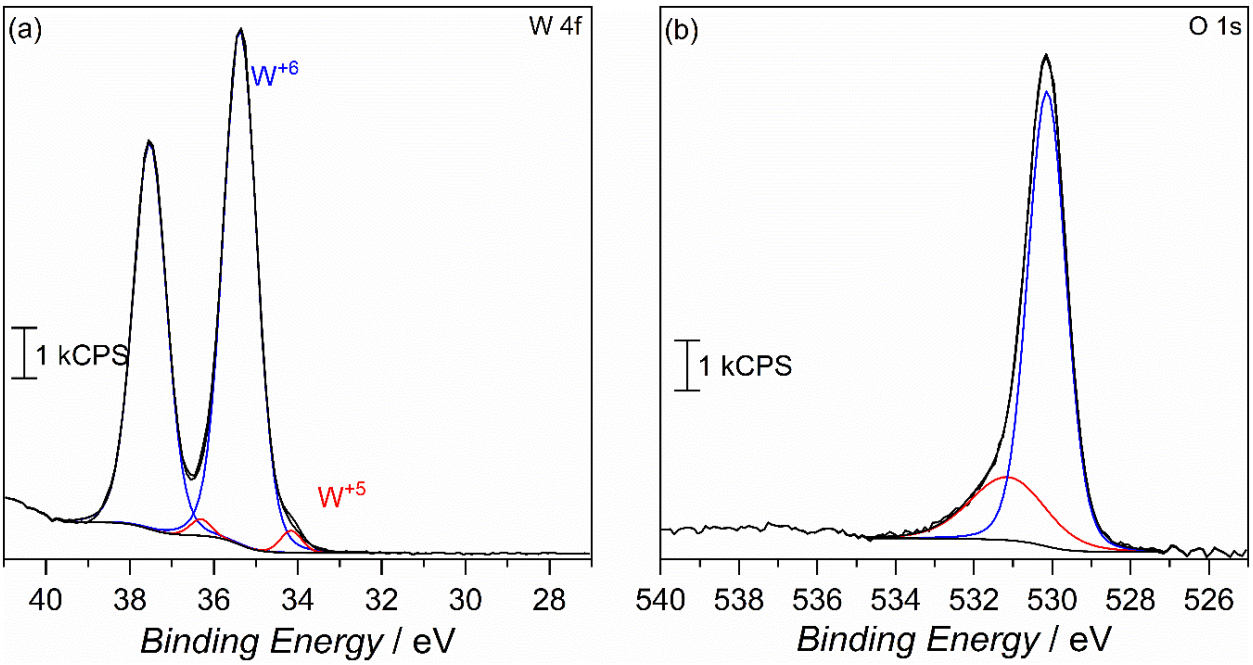

Figure A.7. (a) W 4f and (b) O 1s XPS spectra for the commercially available particles.

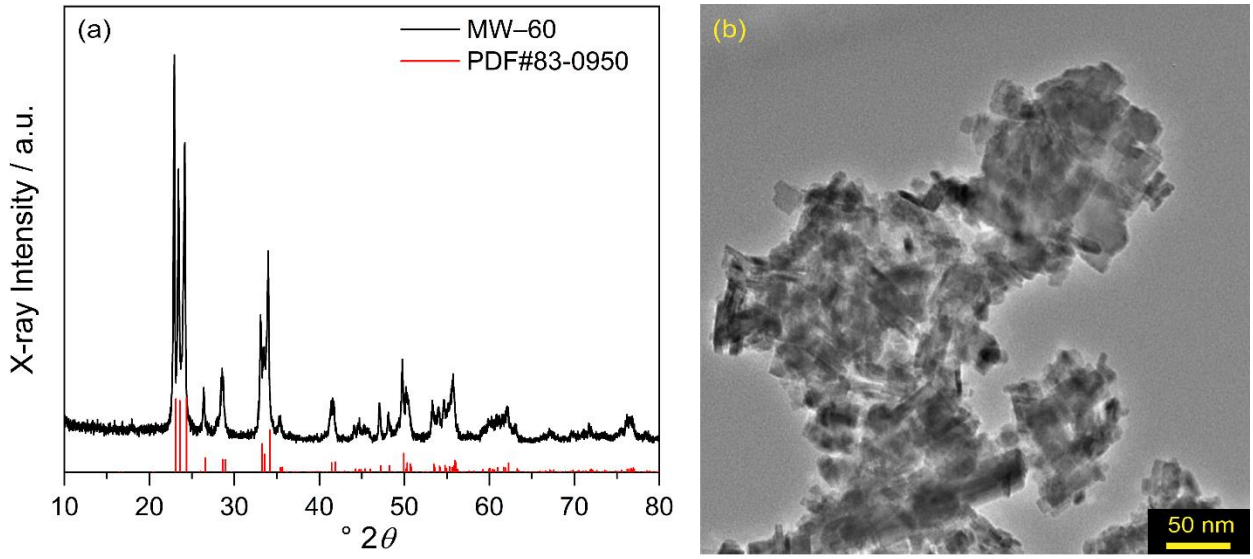

Figure A.8. (a) Powder XRD of the as synthesized WO_3 nanoparticles after 60 minutes of heating (black) and reference pattern (red) for monoclinic WO_3. (b) TEM image of WO_3 particles after 60 minutes of microwave irradiation at 200°C.

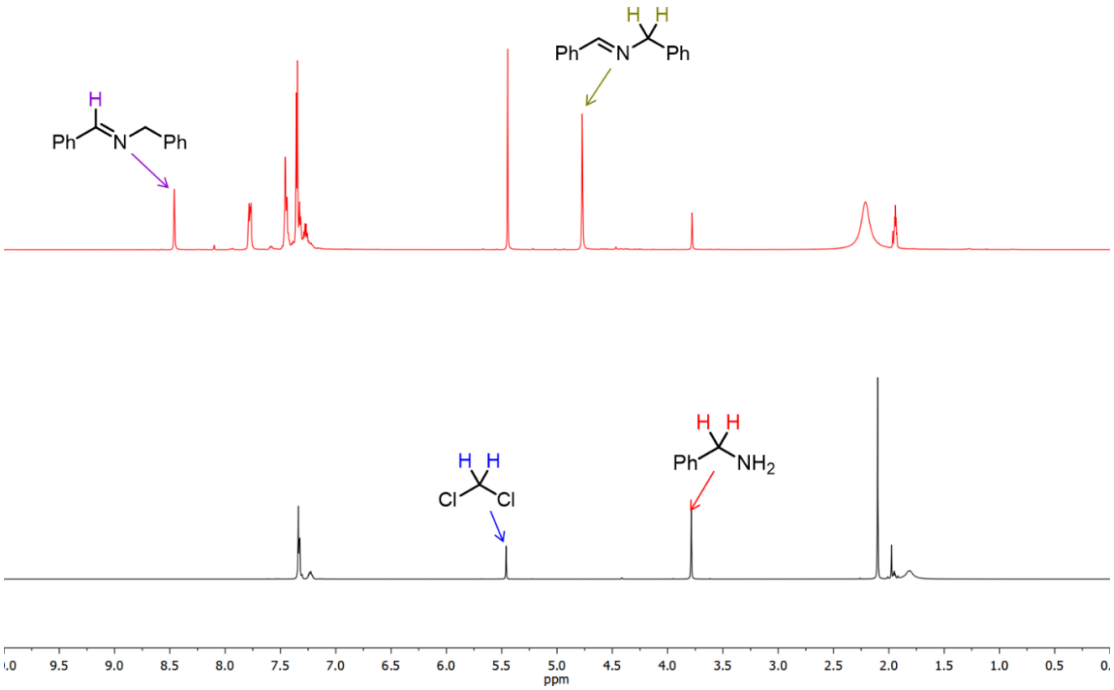

Figure A.9. [1]H-NMR spectra for the pre-photolysis (black) and post-photolysis (red) oxidation of benzylamine. The post-photolysis measurement was obtained after the 250 mM solution of benzylamine was >90% converted; collected at the end of 96 hours. Dichloromethane served as an internal standard for NMR measurements.

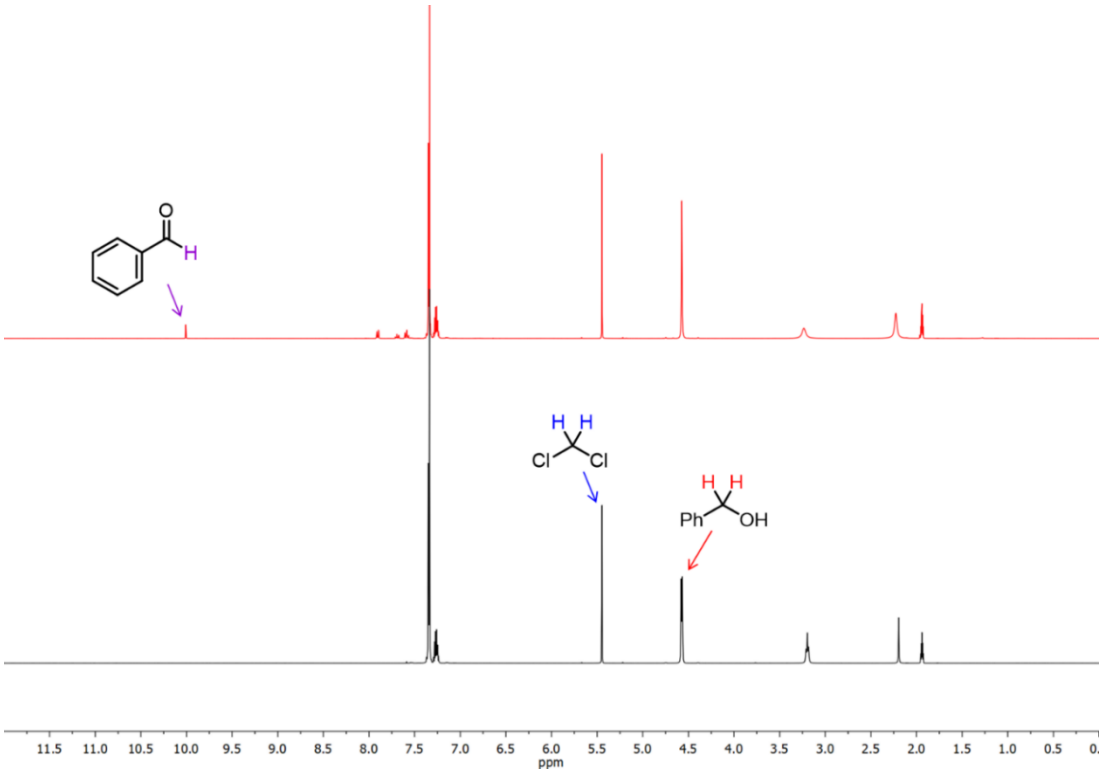

Figure A.10. [1]H-NMR spectra for the pre-photolysis (black) and post-photolysis (red) oxidation of benzyl alcohol. The post-photolysis measurement was obtained after the 250 mM solution of benzyl alcohol was 9.6% converted. Dichloromethane served as an internal standard for NMR measurements.

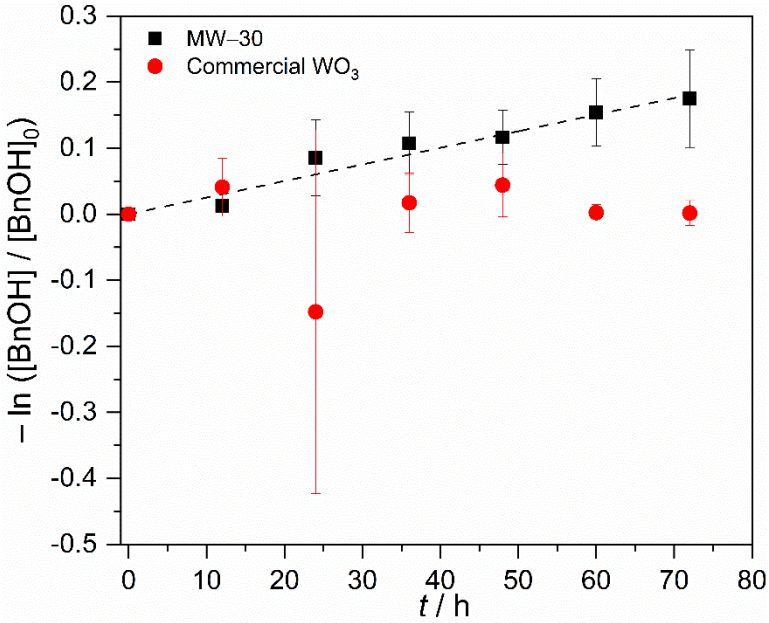

Figure A.11. First order rate plot for the photochemical oxidation of BnOH on MW–30 (black squares) and bulk WO_3 (red circles) using 460 nm blue LED's.

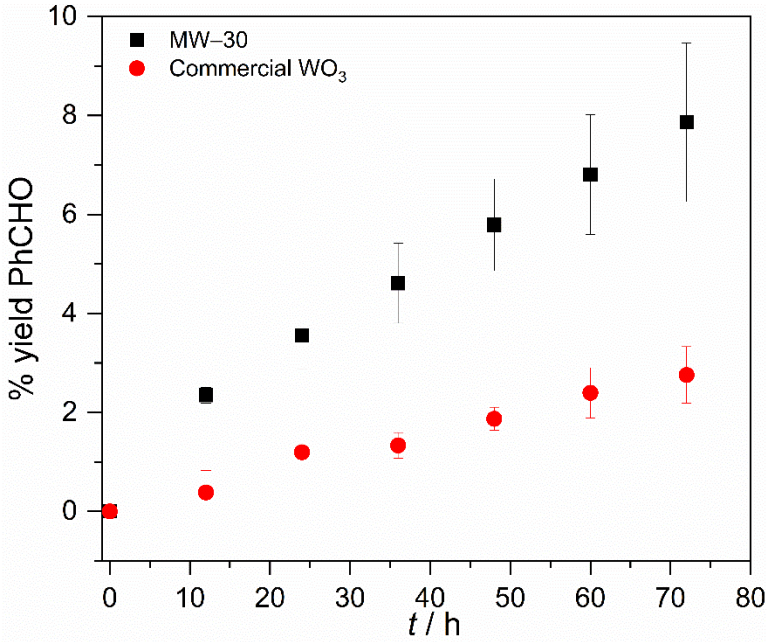

Figure A.12. Yield of benzaldehyde over time after the photochemical oxidation of BnOH on MW–30 (black squares) and bulk WO_3 (red circles) using 460 nm blue LED's.

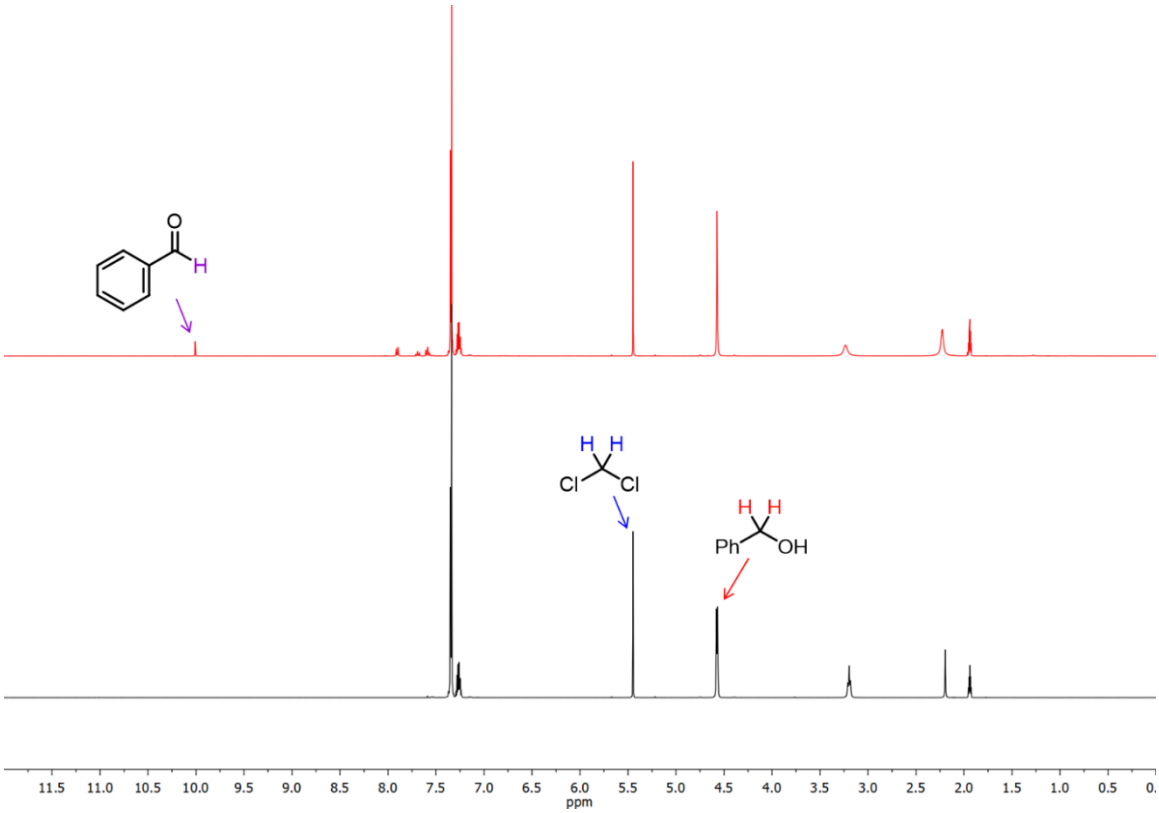

Figure A.13. Sample ^{1}H-NMR spectra for the pre-photolysis (black) and post-photolysis (red) oxidation of benzyl alcohol. The post-photolysis measurement was obtained after the 250 mM solution of benzyl alcohol was 9.6% converted. Dichloromethane served as an internal standard for NMR measurements.

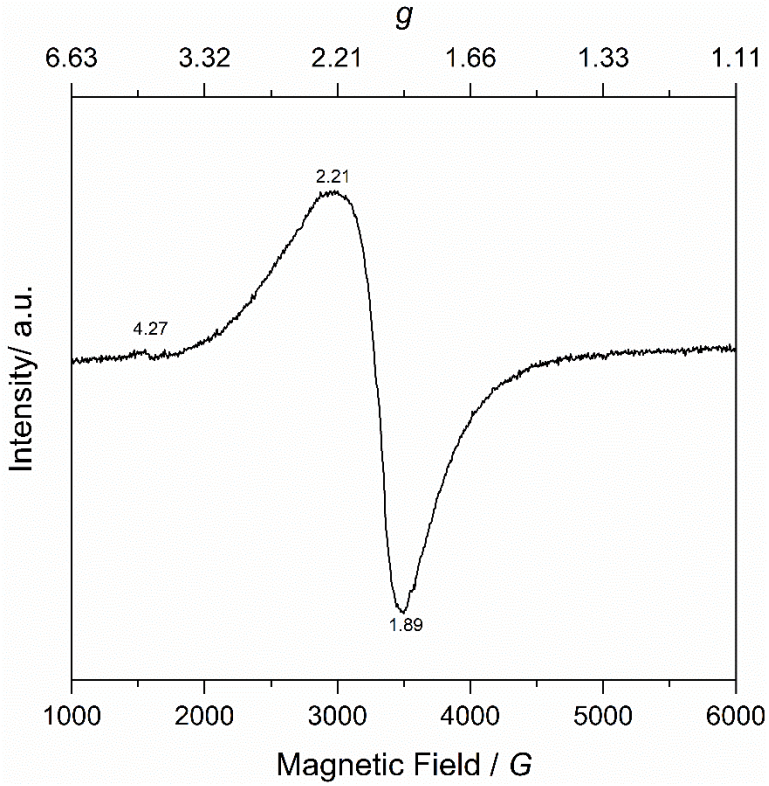

Figure A.14. Room temperature EPR spectra for the MW–30 particles after photocatalysis.

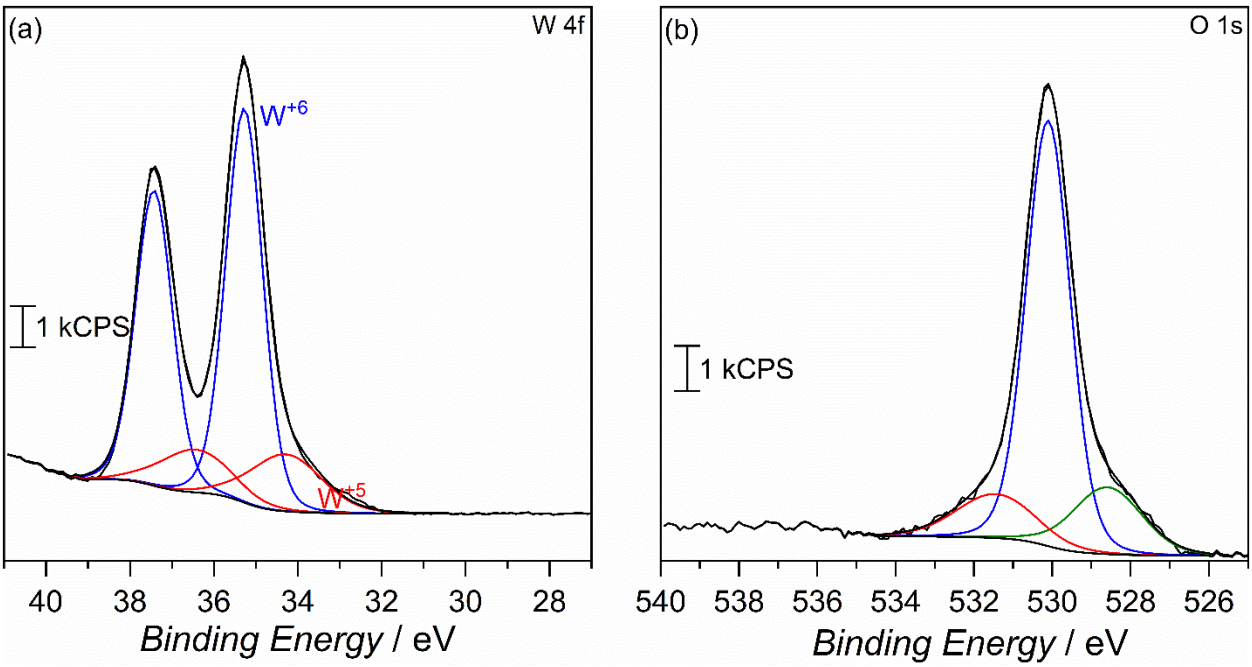

Figure A.15. (a) W 4f and (b) O 1s XPS spectra for the MW–30 particles after photocatalysis.

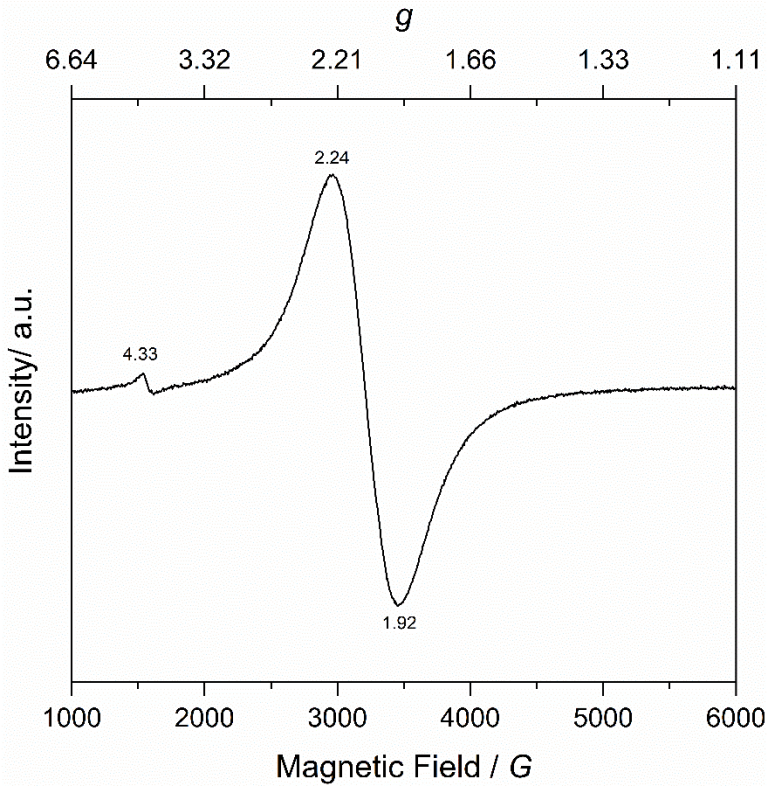

Figure A.16. Room temperature EPR spectra for the MW–30 particles after illumination in a substrate-free solution.

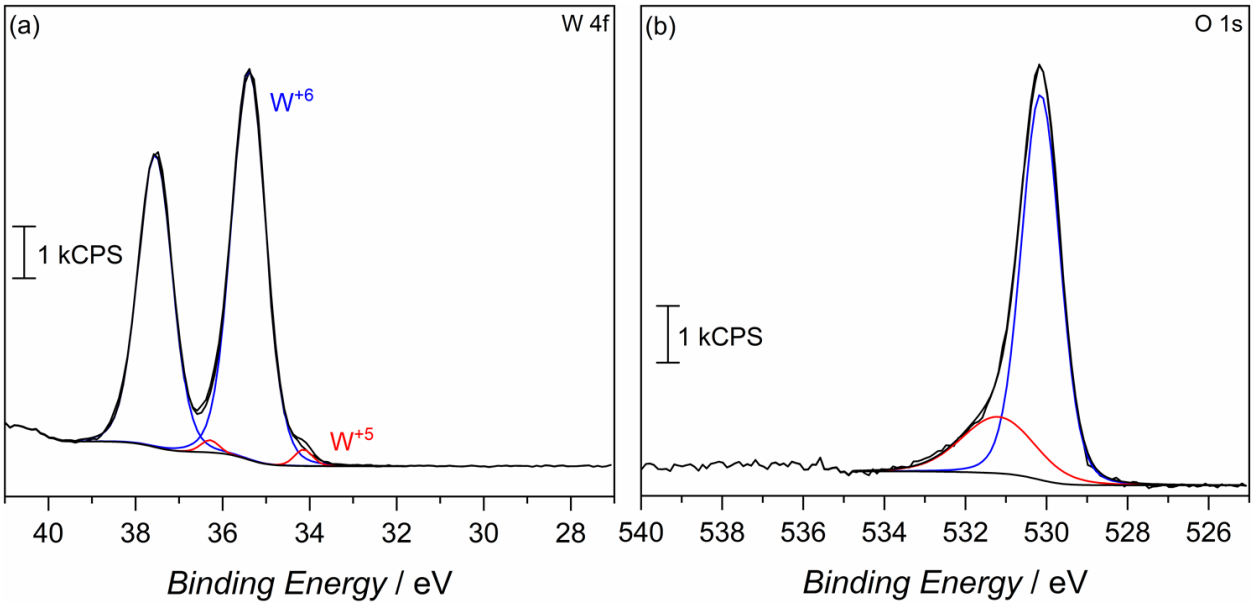

Figure A.17. (a) W 4f and (b) O 1s XPS spectra for the MW–30 particles after illumination in a substrate-free solution.

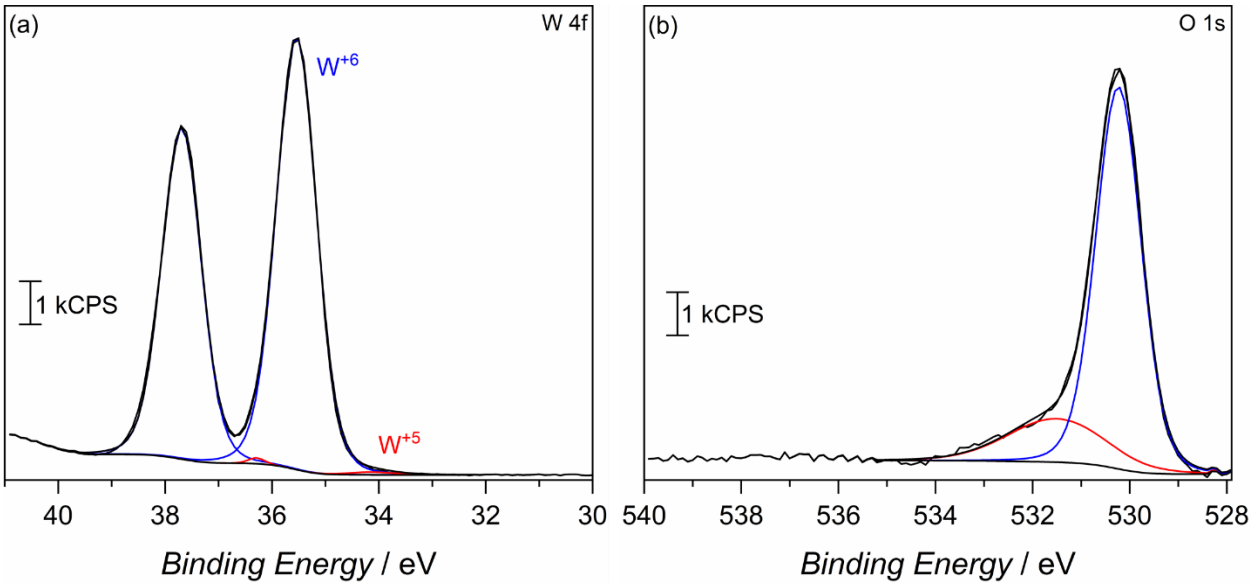

Figure A.18. (a) W 4f and (b) O 1s XPS spectra for the commercial WO_3 particles after photocatalysis.

Appendix B

Supporting Information for Chapter 3

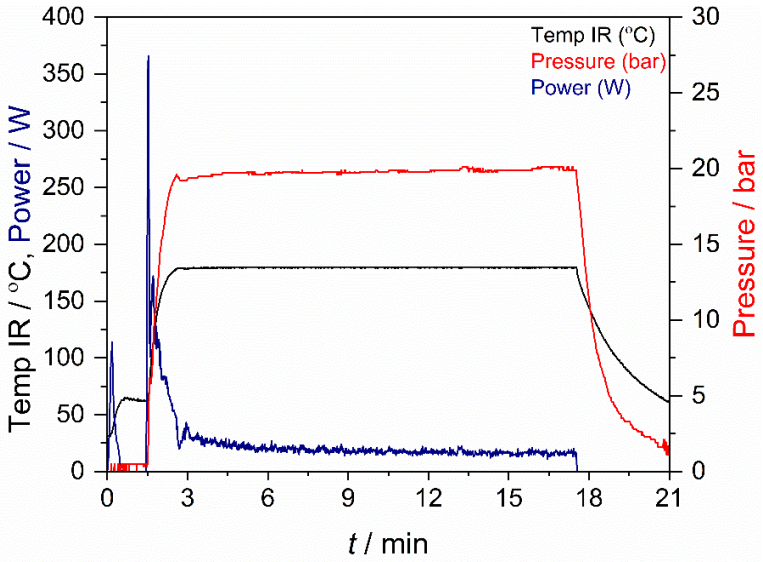

Figure B.1. Temperature, Pressure, and Power readings observed during microwave heating at 180°C for 15 minutes.

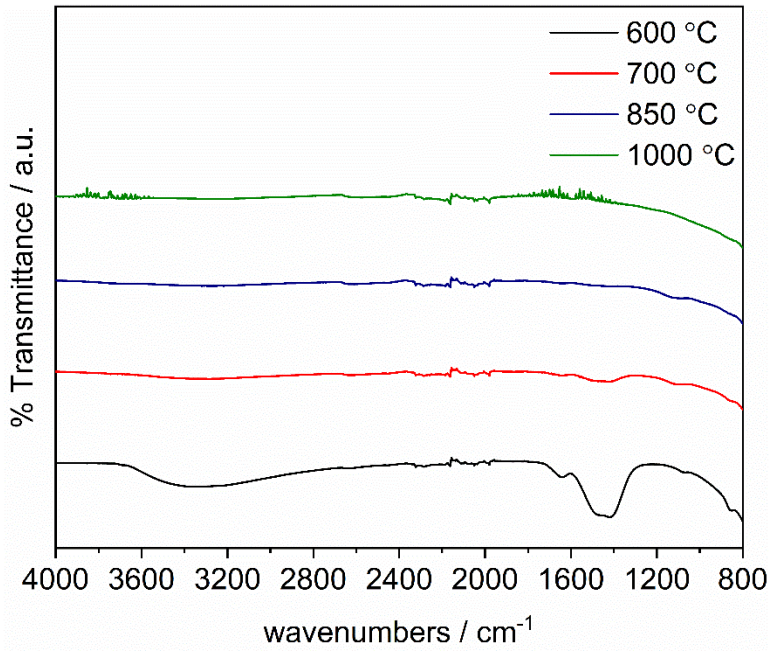

Figure B.2. From bottom to top, FTIR-ATR spectra for $MgFe_2O_4$ nanoparticles annealed at 600 ºC (black), 700 ºC (red), 850 ºC (blue), and 1000 ºC (green).

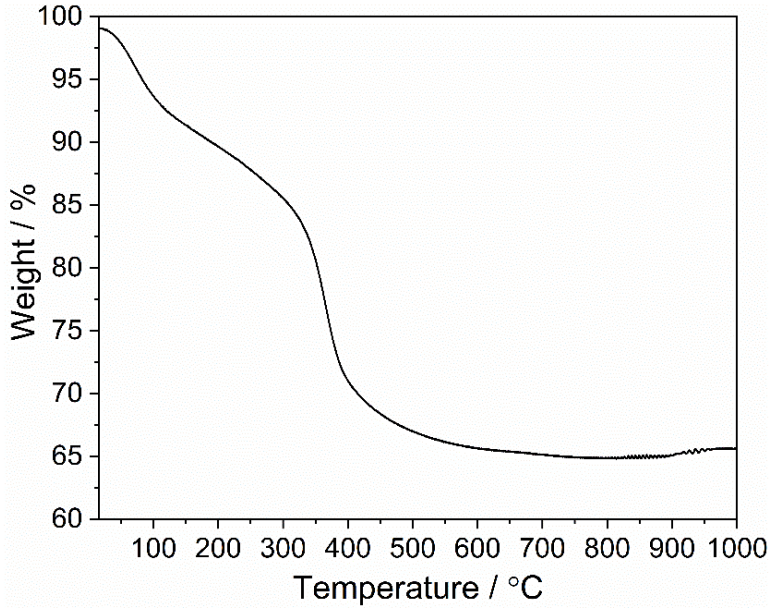

Figure B.3. Thermogravimetric analysis trace recorded in flowing air for unannealed $MgFe_2O_4$.

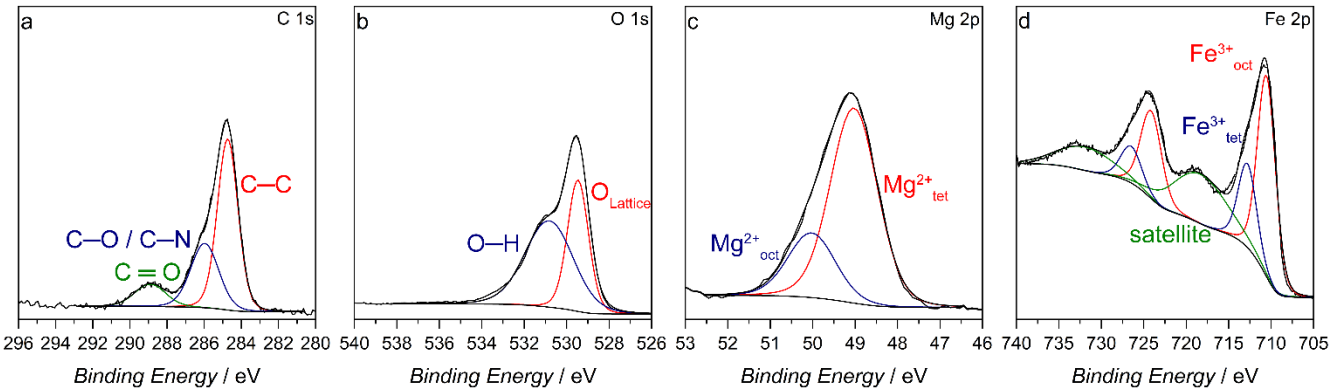

Figure B.4. (a) C 1s, (b) O 1s, (c) Mg 2p, and (d) Fe 2p XPS spectra for $MgFe_2O_4$ nanoparticles annealed at 600 ºC.

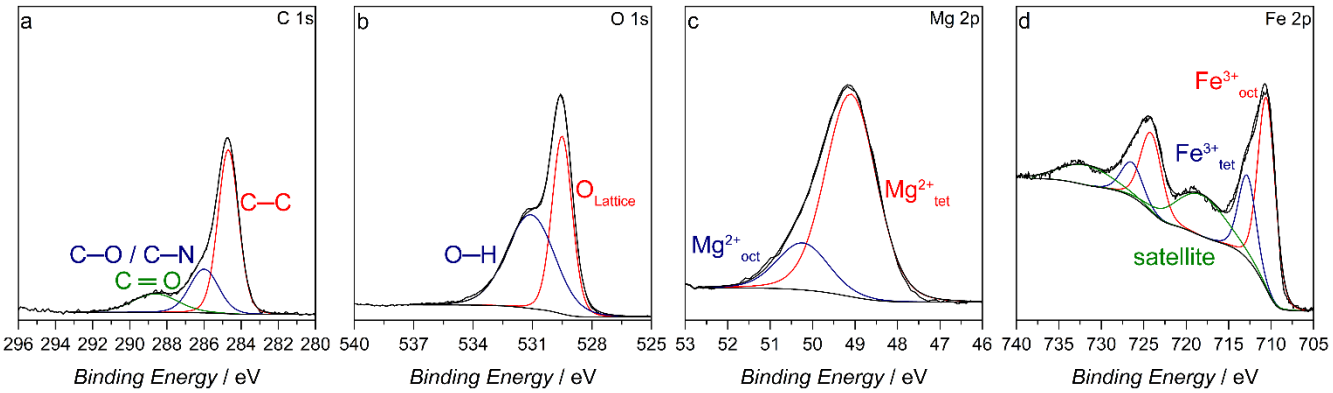

Figure B.5. (a) C 1s, (b) O 1s, (c) Mg 2p, and (d) Fe 2p XPS spectra for $MgFe_2O_4$ nanoparticles annealed at 700 ºC.

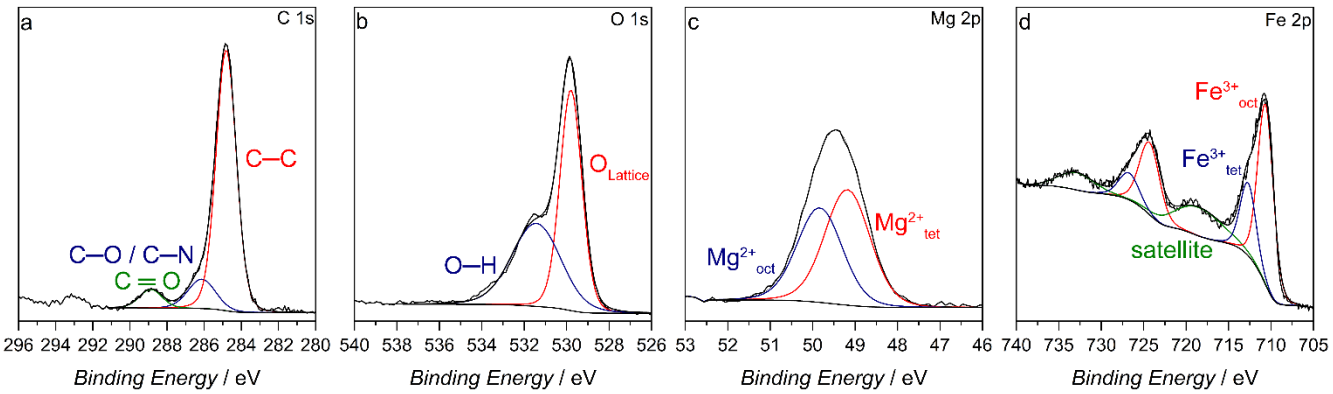

Figure B.6. (a) C 1s, (b) O 1s, (c) Mg 2p, and (d) Fe 2p XPS spectra for $MgFe_2O_4$ nanoparticles annealed at 850 ºC.

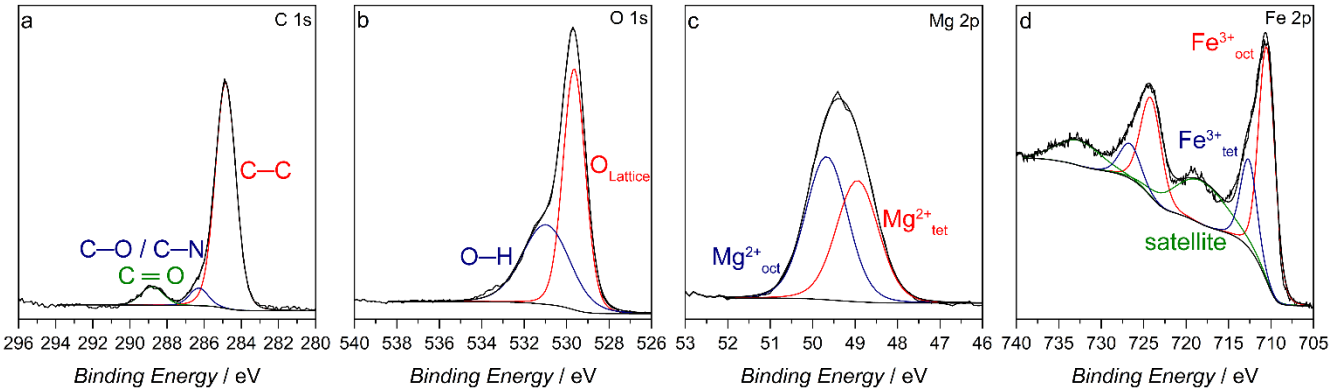

Figure B.7. (a) C 1s, (b) O 1s, (c) Mg 2p, and (d) Fe 2p XPS spectra for $MgFe_2O_4$ nanoparticles annealed at 1000 ºC.

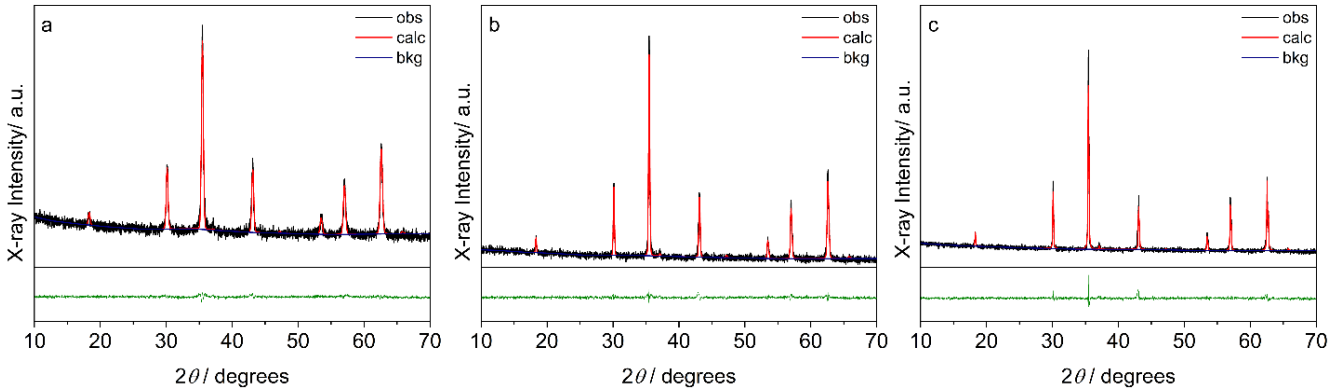

Figure B.8. Rietveld Refinement fittings of XRD patterns of the $MgFe_2O_4$ samples annealed at: (a) 700 °C, χ^2=1.23, R_w=1.68; (b) 850 °C, χ^2=1.17, R_w=1.56; (c) 1000 °C, χ^2=1.46, R_w=1.97. Observed (black), calculated (red), and background (blue) spectra are presented. The difference profile is displayed below in green.

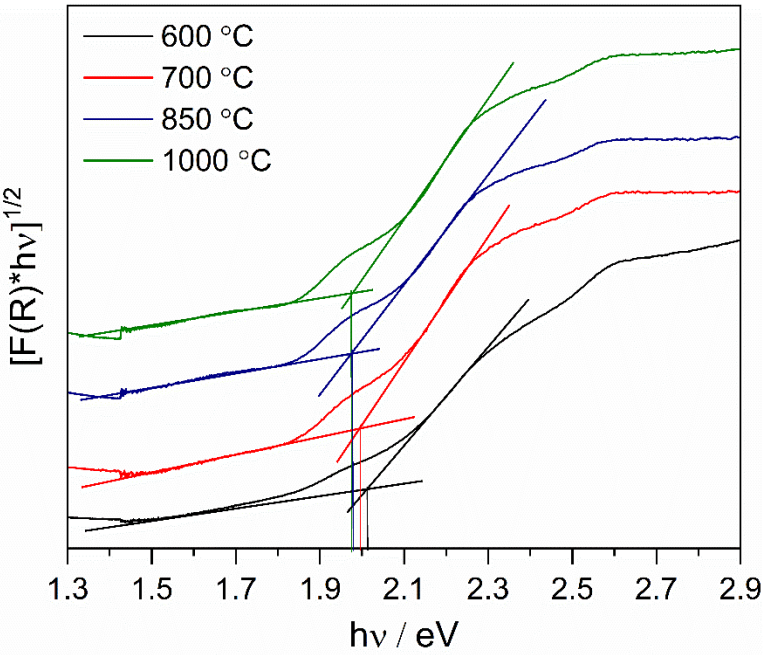

Figure B.9. Tauc Plot for $MgFe_2O_4$ nanoparticles annealed at 600 ºC (black), 700 ºC (red), 850 ºC (blue), and 1000 ºC (green).

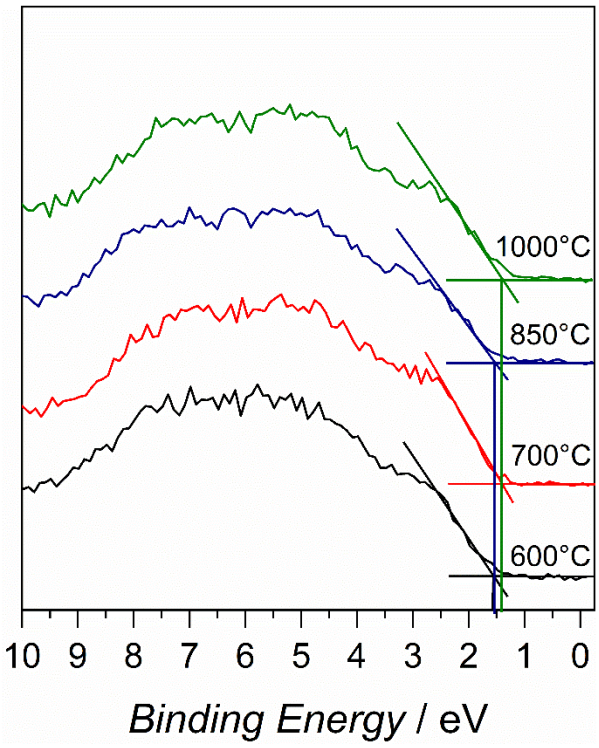

Figure B.10. Valence band XPS spectra $MgFe_2O_4$ nanoparticles annealed at 600 ºC (black), 700 ºC (red), 850 ºC (blue), and 1000 ºC (green).

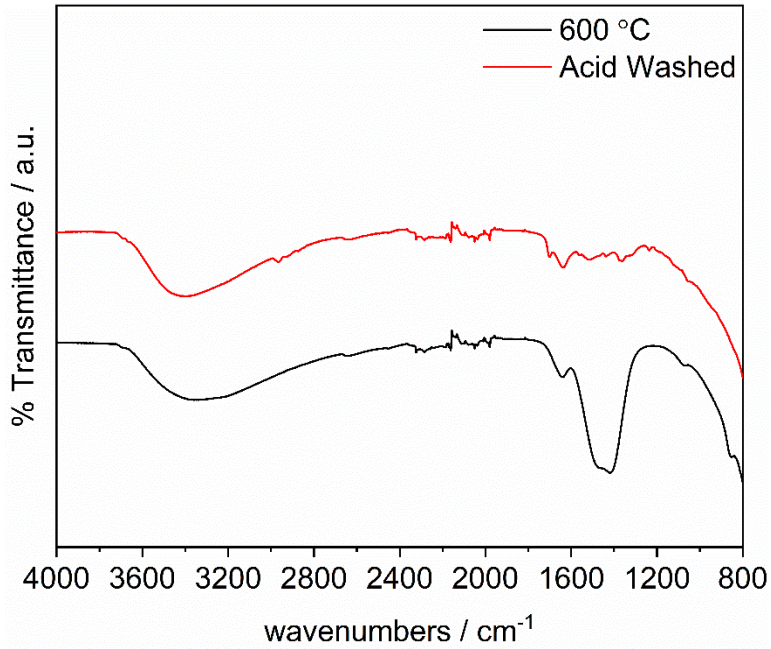

Figure B.11. FTIR-ATR spectra for $MgFe_2O_4$ nanoparticles annealed at 600 ºC as-made (black) and after washing with 1M HCl (red).

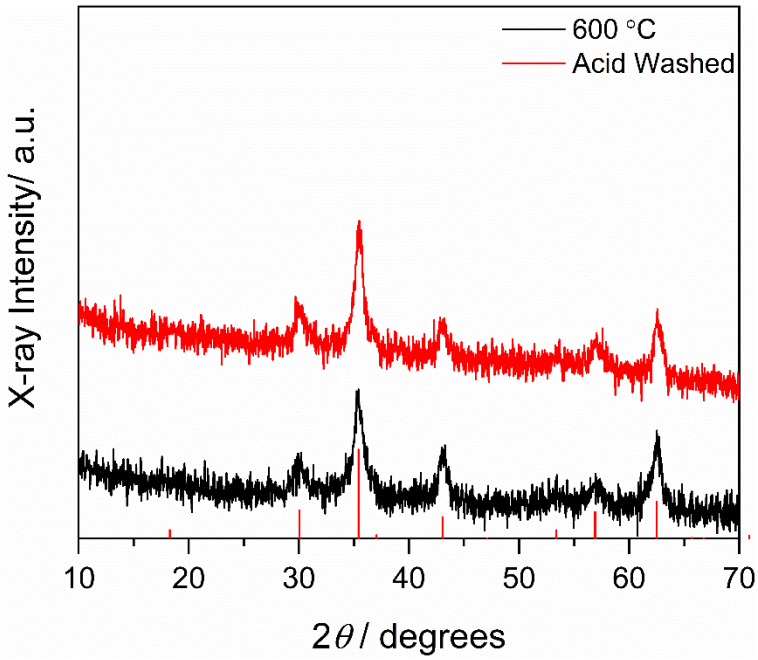

Figure B.12. Powder XRD pattern of $MgFe_2O_4$ nanoparticles annealed at 600 ºC as-made (black) and after washing with 1M HCl (red).

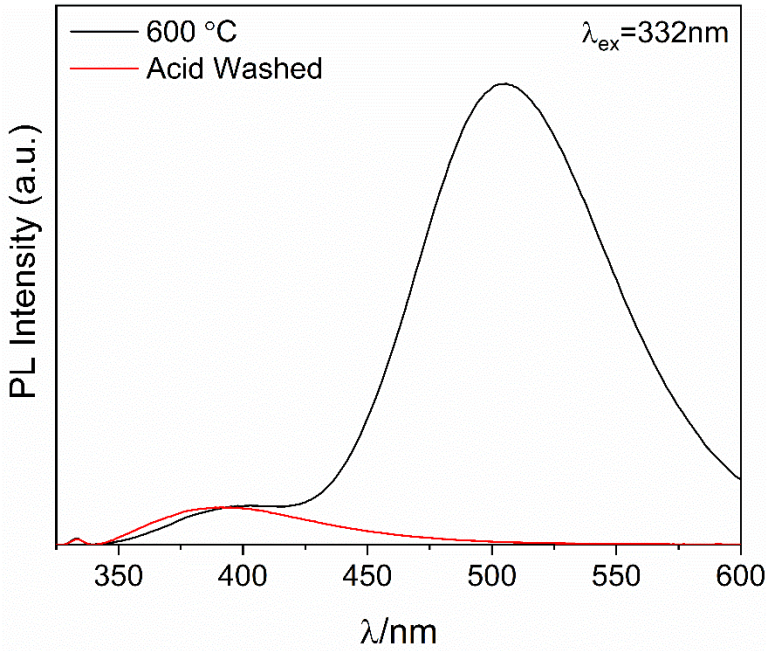

Figure B.13. Emission fluorescence spectra of a solution containing 2 mM coumarin $MgFe_2O_4$ nanoparticles annealed at 600 ºC as-made (black) and after washing with 1M HCl (red).

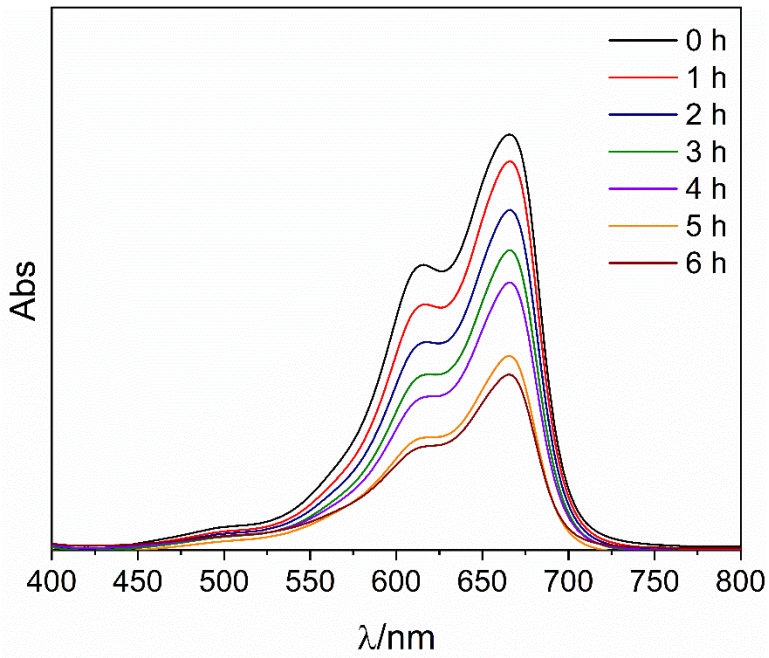

Figure B.14. Sample UV-Vis Absorbance spectra of methylene blue solution degraded under visible light illumination on $MgFe_2O_4$ nanoparticles.

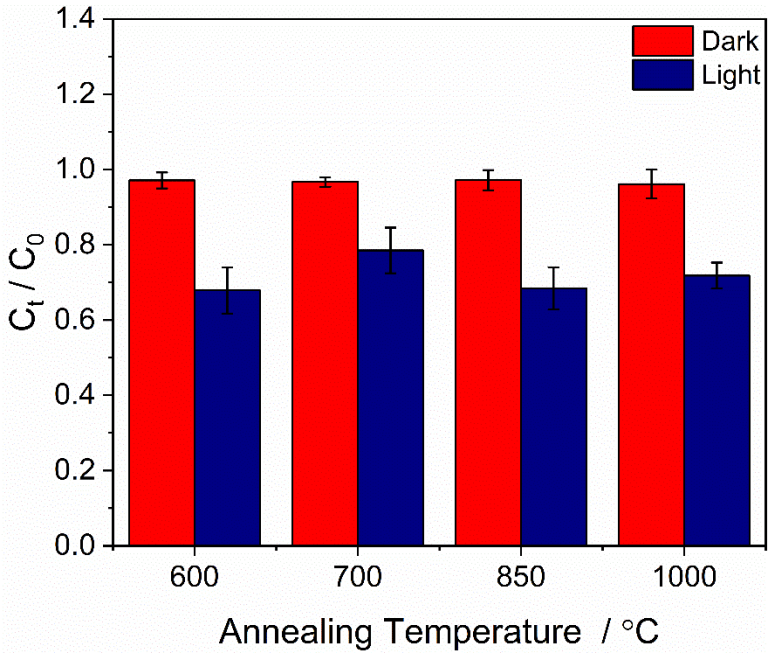

Figure B.15. Bar graph showing the consumption of methylene blue (MB) after a 6-hour period under dark and illuminated conditions on $MgFe_2O_4$ nanoparticles with respect to annealing temperature.

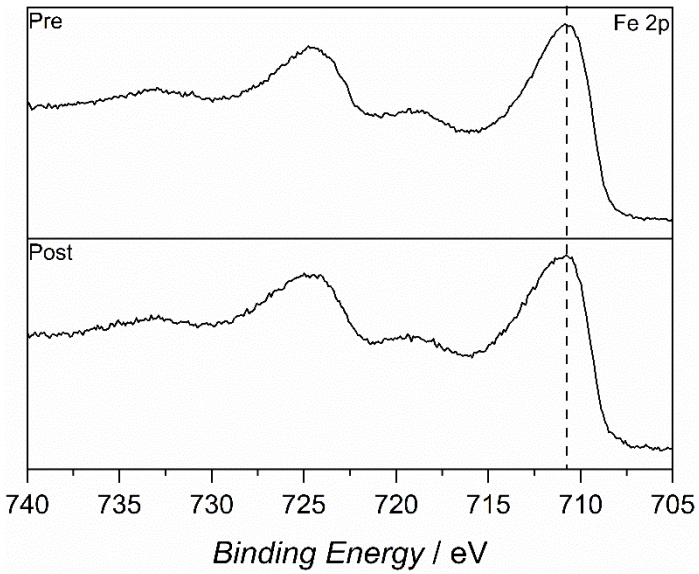

Figure B.16. Fe 2p XPS spectra for $MgFe_2O_4$ nanoparticles annealed at 600 ºC before methylene blue degradation catalysis and after 6 hours of illumination.

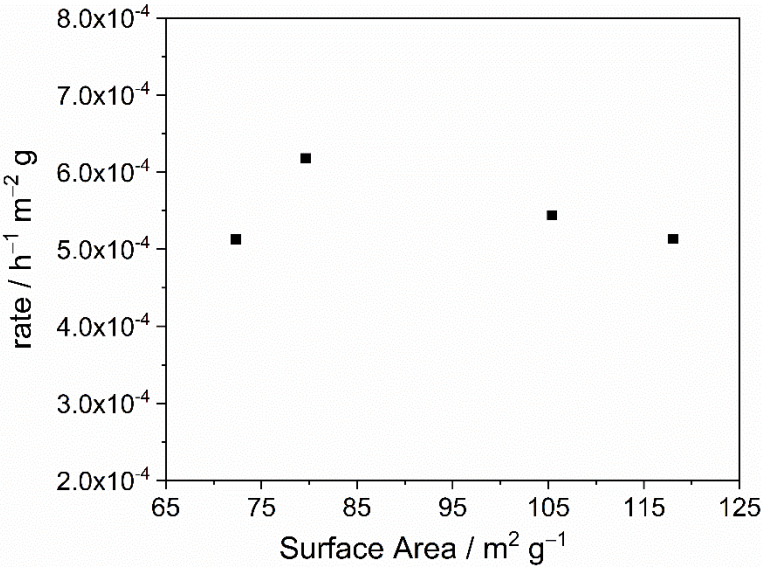

Figure B.17. Reaction rate for the photochemical degradation of methylene blue dye normalized relative to the surface area of the annealed particle samples.

Appendix C

Supporting Information for Chapter 4

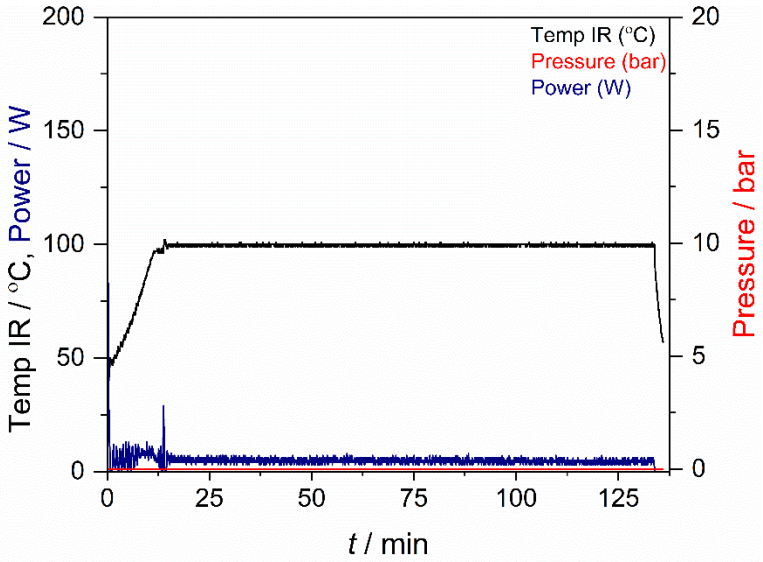

Figure C.1. Temperature, Pressure, and Power readings observed during microwave heating at 100°C for 120 minutes.

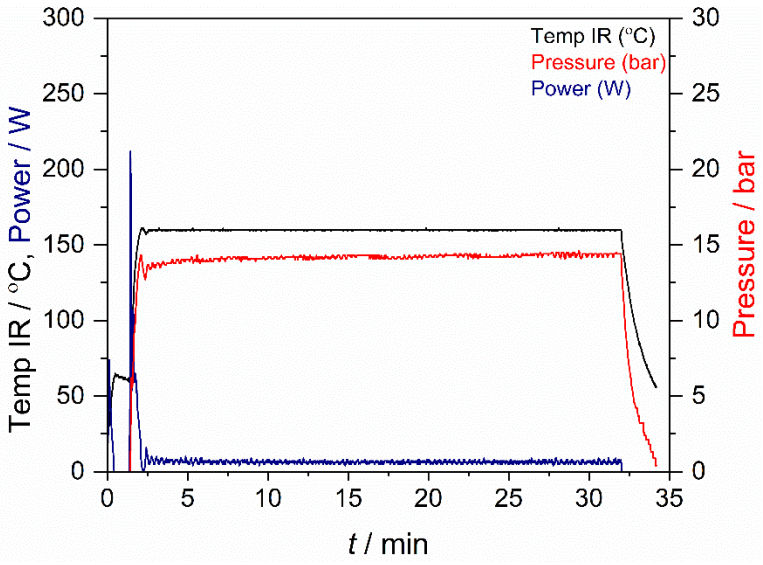

Figure C.2. Temperature, Pressure, and Power readings observed during microwave heating at 160°C for 30 minutes.

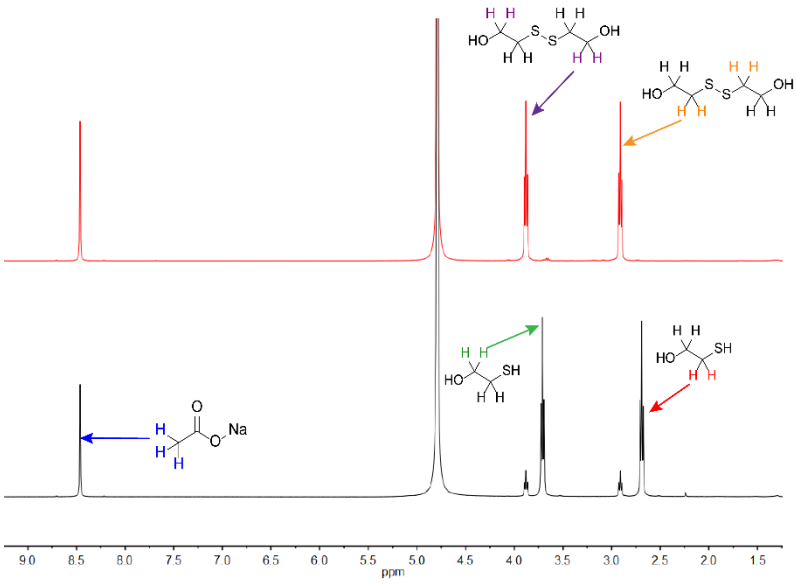

Figure C.3. [1]H-NMR spectra for the pre-photolysis (black) and post-photolysis (red) oxidation of 2-mrcaptoethanol. The post-photolysis measurement was obtained after the 100 mM solution of 2-mercaptoethanol was >99% converted. Sodium formate served as an internal standard for aqueous NMR measurements.

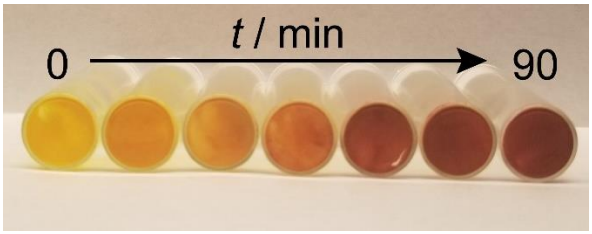

Figure C.4. Picture of the color change experienced during oxidation of 2-mercaptoethanol in acetonitrile solvent. Increasing time from 0 to 90 minutes following the arrow.

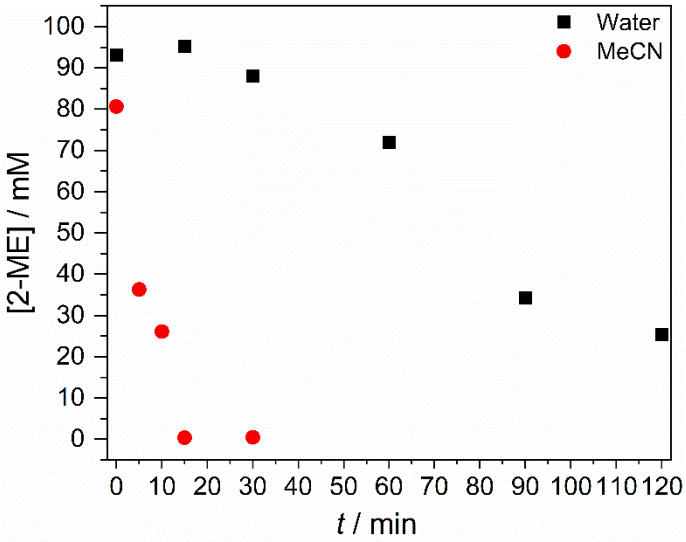

Figure C.5. 2-mercaptoethanol consumption in alkaline water (black squares) and acetonitrile (red circles) on CdSe@TiO_2 nanoparticles using 460 nm blue LEDs.

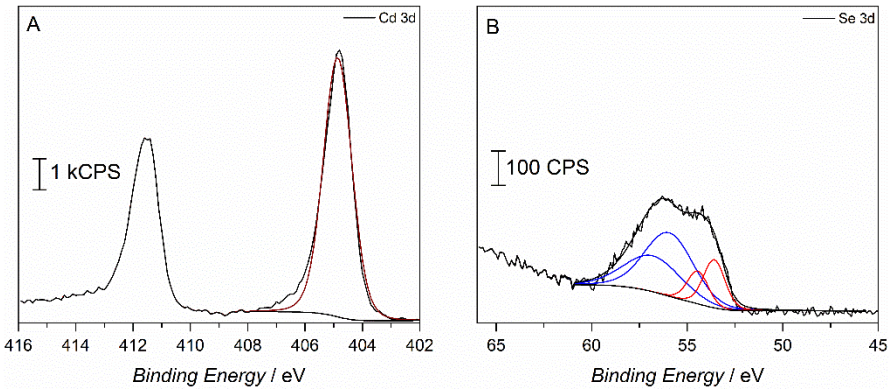

Figure C.6. (a) Cd 3d and (b) Se 3d XPS spectra for CdSe@amine quantum belts.

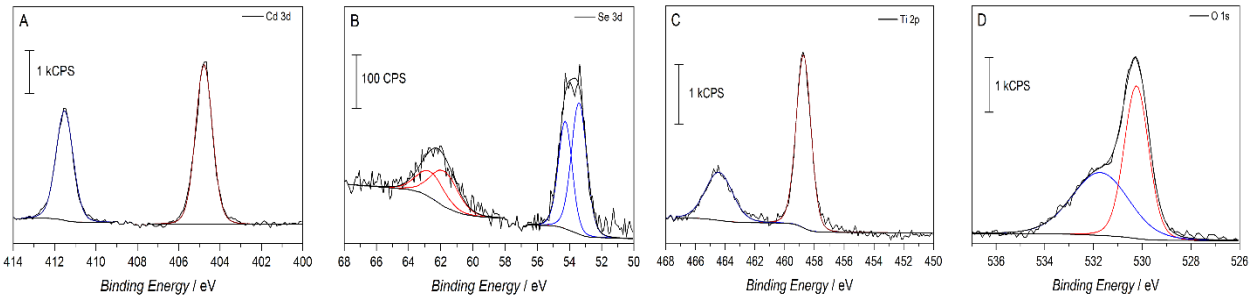

Figure C.7. (a) Cd 3d, (b) Se 3d, (c) Ti 2p, and (d) O 1s XPS spectra for CdSe@TiO_2 quantum belts as synthesized.

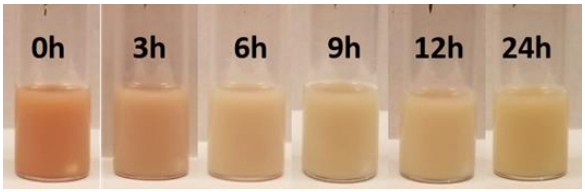

Figure C.8. Picture of the color change experienced during oxidation of benzyl alcohol in acetonitrile solvent. Increasing time from 0 to 24 hours as labeled.